

Ion beam modification of phase-change materials for optical applications

Dissertation

zur Erlangung des akademischen Grades
doctor rerum naturalium (Dr. rer. nat.)

vorgelegt dem Rat der Physikalisch-Astronomischen Fakultät der
Friedrich-Schiller-Universität Jena



**FRIEDRICH-SCHILLER-
UNIVERSITÄT
JENA**

von M.Sc. Martin Hafermann
geboren am 07.12.1990 in Rudolstadt

- 1. Gutachter:** Prof. Dr. Carsten Ronning, Friedrich-Schiller-Universität Jena
- 2. Gutachter:** Prof. Dr. Thomas Taubner, RWTH Aachen University
- 3. Gutachter:** Prof. Dr. Thomas Zentgraf, Universität Paderborn

Tag der Abgabe: 28.10.2020

Tag der Disputation: 18.02.2021

Abstract

Recent progress in the miniaturization of optical components was enabled by the emergence of metasurfaces, which allow to manipulate the amplitude, phase, and polarization of light on length scales smaller than the wavelength. Typically, metasurfaces comprise regularly arranged, subwavelength-sized metallic nanoantennas with varying geometry, size, shape, or orientation. Furthermore, they possess effective optical properties resulting from light interaction with the individual nanoantennas leading to unconventional optical responses. Plasmonic metasurfaces comprise lossy metals that reduce the device efficiency. Although they were recently superseded by low-loss, all-dielectric metasurfaces, individual scatterers lack *in-operando* tunability. Phase-change materials are introduced as active media into metasurfaces to overcome this limitation. The optical and electrical properties of such materials are drastically changed when switching between amorphous and crystalline states. Recently, the combination of phase-change materials and metasurfaces allows to control the optical response on demand, which resulted in dynamically switchable, tunable, and reconfigurable functionalities. Furthermore, active photonic devices relying on artificial phase coexistence of amorphous and crystalline regions were realized using conventional direct laser writing.

Any feature size of direct laser writing is diffraction-limited. Thus, this thesis introduces ion beam irradiation of $\text{Ge}_2\text{Sb}_2\text{Te}_5$, a typical phase-change material, to overcome this limitation, as ion beams can be focused down to a few nanometers. Through gaining a deep understanding of the effects of ion irradiation on the optical properties of $\text{Ge}_2\text{Sb}_2\text{Te}_5$, several approaches are demonstrated to facilitate the successful integration of ion beam modified phase-change materials into optical devices.

Homogeneous noble gas ion irradiation lead to amorphization of initially crystalline $\text{Ge}_2\text{Sb}_2\text{Te}_5$ films caused by induced atomic displacements. Structural and optical investigations during and subsequent to ion bombardment revealed several structural and electronic transitions. Already small amounts of disorder in the hexagonal phase drive a metal-to-insulator transition before a structural conversion into the rock-salt phase occurs. Finally, the accumulation of lattice defects culminates in progressive amorphization of initially crystalline (hexagonal and rock-salt) $\text{Ge}_2\text{Sb}_2\text{Te}_5$ films. The precise control over the amount of lattice disorder grants access to tailorable optical properties of $\text{Ge}_2\text{Sb}_2\text{Te}_5$. Stacking a $\text{Ge}_2\text{Sb}_2\text{Te}_5$ thin film on top of a gold reflector lead to near-zero reflectance in the near infrared spectral region that can be adjusted by appropriately tailoring disorder.

Spatially selective ion irradiation is introduced using a focused ion beam system. By this means, a rock-salt $\text{Ge}_2\text{Sb}_2\text{Te}_5$ film on gold was directly patterned to achieve artificial lateral phase coexistence of regularly arranged amorphous stripes embedded in the crystalline matrix. This resulted in an anisotropic metasurface showing optical dichroism. Furthermore, tailoring disorder in very confined regions allows for grayscale patterning at the nanoscale.

An alternative route to achieve lateral phase coexistence is introduced by ion beam impurity doping. Impurity concentrations of a couple of at.% revealed an increased thermal stability of the amorphous phase compared to non-implanted $\text{Ge}_2\text{Sb}_2\text{Te}_5$. Spatially selective impurity doping combined with appropriate thermal annealing thus allow for active in- and out-tuning of artificial phase coexistence.

Zusammenfassung

Fortschritte in der Miniaturisierung optischer Komponenten wurden in den letzten Jahren durch das Aufkommen von Metaoberflächen ermöglicht, die es erlauben, die Amplitude, Phase und Polarisation von Licht auf Längenskalen kleiner als die Wellenlänge zu manipulieren. Typischerweise bestehen Metaoberflächen aus regelmäßig angeordneten, metallischen Nanoantennen mit unterschiedlicher Geometrie, Größe, Form oder Orientierung. Darüber hinaus besitzen sie effektive optische Eigenschaften, die aus der Lichtwechselwirkung mit den einzelnen Nanoantennen resultieren und zu unkonventionellen optischen Antworten führen. Obwohl plasmonische Metaoberflächen aus verlustbehafteten Metallen, die den Wirkungsgrad des Bauelements limitieren, vor kurzem durch verlustarme, vollständig dielektrische Metaoberflächen ersetzt wurden, sind die optischen Eigenschaften einzelner Streuelemente statisch. Um diese Beschränkung zu überwinden, werden Phasenwechselmaterialien als aktive Medien in die Metaoberflächen eingebaut. Die optischen und elektrischen Eigenschaften solcher Materialien verändern sich beim Wechsel zwischen amorpher und kristalliner Phase drastisch. Die Kombination von Phasenwechselmaterialien mit Metaoberflächen ermöglicht die Steuerung der optischen Antwort nach Bedarf, was zu dynamisch schaltbaren, abstimmbaren und rekonfigurierbaren Funktionalitäten führt. Darüber hinaus wurden zuletzt aktive photonische Bauelemente unter Verwendung von konventionellem, direktem Laserschreiben realisiert, die auf der künstlichen Phasenkoexistenz amorpher und kristalliner Bereiche beruhen.

Jede Strukturgröße des direkten Laserschreibens ist beugungsbegrenzt. Um diese Beschränkung zu überwinden wird in dieser Arbeit die Ionenbestrahlung von dem typischen Phasenwechselmaterial $\text{Ge}_2\text{Sb}_2\text{Te}_5$ eingeführt, da Ionenstrahlen bis auf wenige Nanometer fokussiert werden können. Über das Erlangen eines tiefen Verständnisses von den Auswirkungen der Ionenbestrahlung auf die optischen Eigenschaften von $\text{Ge}_2\text{Sb}_2\text{Te}_5$, werden verschiedene Ansätze zur erfolgreichen Integration von Ionenstrahl-modifizierten Phasenwechselmaterialien in optische Geräte demonstriert.

Homogene Ionenbestrahlung von Edelgasen führt zur Amorphisierung ursprünglich kristalliner $\text{Ge}_2\text{Sb}_2\text{Te}_5$ -Schichten, die durch induzierte atomare Deplatzierungen verursacht wird. Strukturelle und optische Untersuchungen während und nach dem Ionenbeschuss zeigen mehrere strukturelle und elektronische Übergänge. Bereits geringe Mengen an Unordnung in der hexagonalen Phase treiben einen Metall-Isolator-Übergang an, bevor eine strukturelle Umwandlung in die Natriumchlorid-Phase stattfindet. Schließlich gipfelt die Akkumulation von Gitterdefekten in einer fort-

schreitenden Amorphisierung von anfänglich kristallinen (hexagonale Struktur bzw. Natriumchlorid-Struktur) $\text{Ge}_2\text{Sb}_2\text{Te}_5$ -Schichten. Darüber hinaus ermöglicht die präzise Kontrolle der Menge an Unordnung den Zugang zu maßgeschneiderten optischen Eigenschaften von $\text{Ge}_2\text{Sb}_2\text{Te}_5$. Das Stapeln einer dünnen $\text{Ge}_2\text{Sb}_2\text{Te}_5$ -Schicht auf einen Goldreflektor führt zu einem Reflexionsgrad nahe Null im nahen infraroten Spektralbereich, der durch geeignete Anpassung der Unordnung eingestellt werden kann.

Räumlich selektive Ionenbestrahlung wird mit einem fokussierten Ionenstrahlensystem erreicht. Auf diese Weise wird eine $\text{Ge}_2\text{Sb}_2\text{Te}_5$ -Schicht (in der Natriumchlorid-Struktur) auf Gold direkt strukturiert, um eine künstliche, laterale Phasenkoexistenz zu erreichen. Diese besteht aus regelmäßig angeordneten, amorphen Streifen, die in die kristalline Matrix eingebettet sind, was zu einer anisotropen Metaoberfläche mit optischem Dichroismus führt. Darüber hinaus ermöglicht die Kontrolle über die Menge an Unordnung in räumlich sehr definierten Bereichen eine Graustufenstrukturierung auf der Nanoskala.

Ein alternativer Weg, um eine laterale Phasenkoexistenz zu erreichen, ist die Dotierung mittels Ionenimplantation. Dotierkonzentrationen von einigen at.% zeigen eine erhöhte thermische Stabilität der amorphen Phase im Vergleich zu nicht implantiertem $\text{Ge}_2\text{Sb}_2\text{Te}_5$. Die räumlich selektive Dotierung von Verunreinigungen in Kombination mit geeigneter thermischer Wärmebehandlung ermöglicht somit aktives Ein- und Ausschalten der künstlichen Phasenkoexistenz.

Contents

1. Introduction	3
2. Fundamentals	8
2.1. Ion beam modification of solids	8
2.2. Phase-change materials	10
2.2.1. Amorphization and glass formation	11
2.2.2. Crystallization process	12
2.2.3. Typical phase-change materials	13
2.3. GeTe–Sb ₂ Te ₃ pseudo-binary compounds - GST	14
2.3.1. Crystallographic and electronic structures of Ge ₂ Sb ₂ Te ₅	14
2.3.2. Atomistic description of the phase-change in Ge ₂ Sb ₂ Te ₅	18
2.3.3. Metal-insulator transition in Ge ₂ Sb ₂ Te ₅	19
2.3.4. Electrical and optical properties of Ge ₂ Sb ₂ Te ₅	20
2.3.5. Engineering the phase-change	21
3. Experimental methods	23
3.1. Deposition methods	23
3.2. Characterization methods	23
3.2.1. Structural characterization	23
3.2.2. Optical characterization	25
3.3. Imaging methods	26
3.3.1. Electron microscopy	26
3.3.2. Scanning probe microscopy	27
3.4. Modification methods	28
3.4.1. Ion irradiation	28
3.4.2. In-situ optical/electrical measurements during ion irradiation	29
3.5. Simulations and numerical methods	30
4. Intrinsic physical properties of GST thin films	31
4.1. Integral composition of as-deposited GST thin films	31
4.2. Thermal annealing	33
4.3. Structural properties	35
4.4. Optical properties	37
5. Tailoring disorder in GST thin films	41
5.1. Ion beam induced disorder – in-situ measurements	41
5.2. Ion energy dependence of lattice defects	43
5.3. Ex-situ measurements on tailored disorder in GST	45
5.3.1. Disorder-driven metal-insulator transition in hexagonal GST	45

5.3.2.	Disorder-induced structural transitions of hexagonal GST	48
5.3.3.	Disorder-induced progressive amorphization of rock-salt GST	51
5.4.	In-situ annealing of defects during ion irradiation	53
5.5.	Temperature dependence of tailored disorder in GST	55
5.5.1.	Reconfigurability of ion beam amorphized GST films	56
5.5.2.	Thermal stability of intermediate states	57
5.6.	Tailorable near-zero reflection – an application	59
5.6.1.	Intrinsic properties of a GST thin film on Au	61
5.6.2.	Manipulating near-zero reflection via tailoring disorder	62
5.6.3.	Comparison of large-scale and focused ion beam irradiation	65
5.7.	Conclusions	66
6.	Artificial phase coexistence enabled by ion beam patterning	68
6.1.	Dichroism in an anisotropic GST metasurface	68
6.2.	Spatially resolved phase coexistence via optical nanoimaging	72
6.2.1.	Gradually tailorable optical properties at the nanoscale	76
6.2.2.	Exploring the spatial limits of locally tailored disorder	79
6.3.	Grayscale nanopatterning of GST	81
6.4.	Conclusions	83
7.	Ion beam impurity doping of GST for active optical devices	84
7.1.	Polymorphism of amorphous GST	84
7.2.	Impurity doping with group V elements	86
7.2.1.	Manipulating the crystallization process in GST	86
7.2.2.	Reconfigurability of doped GST films	90
7.3.	Spatially selective impurity doping – proof of concept	92
7.4.	Conclusions	95
8.	Conclusion and outlook	97
	Bibliography	101
A.	Appendices	vii
B.	List of publications	x
C.	List of oral and poster presentations	xii
D.	Ehrenwörtliche Erklärung	xiii

1. Introduction

The digital era entails a plethora of digital devices that are designed to support and automate human tasks and activities, enrich human social interaction, and improve interaction with the physical world [1]. The emergence of such devices – referred to as smart devices – lead to the invention of smartphones, tablets, smartwatches, smart speakers, and many others. Their integration into everyday life is already ubiquitous in so-called smart environments such as smart homes, smart cities, and smart manufacturing. Among many applications, where smart devices operate interactively and autonomously, they provide the ability to expand reality towards virtual and augmented reality (AR). The latter is considered as the next generation of display technology that superimposes a computer-generated image on a user’s view of the real world to present a composite view. Among others, see-through near-eye displays, denoted AR glasses, were proposed to grant an immersive experience [2]. Here, the virtual image is created directly in front of the human eye enabled by a transparent eyepiece, while projection typically relies on spherical mirrors, free-form optics [3], and diffractive [4] or holographic optical elements [5]. As the modulation of the wavefront in such conventional optical components is based on light propagation through dispersive media over distances much larger than the wavelength, they lack the ability of miniaturization; thus, truly mobile and highly usable AR glasses remain challenging. Recently, Lee *et al.* introduced metasurfaces into the optical path in AR glasses envisioning miniaturized optical components in such smart devices [6].

The two-dimensional equivalents of metamaterials, called metasurfaces, are subwavelength thin, artificially engineered optical materials that manipulate the amplitude, phase, and polarization of light in a desired manner [7–11]. They typically comprise regularly arranged, subwavelength-sized building blocks with spatially varying geometry, size, shape, or orientation. Commonly, these building blocks consist of noble metal nanoresonators (nanoantennas), which gave rise to plasmonic metasurfaces. The effective optical properties, which typically cannot be deduced from the metasurfaces’ constituents, paved the way for numerous applications such as beam shaping [12–15], optical modulation [16, 17], hologram generation [18, 19], and perfect light absorption [20, 21]. Recently, plasmonic metasurfaces, which suffer from high-losses limiting the device efficiency, were superseded by the emergence of low-loss, all-dielectric metasurfaces [22–25]. However, as such devices are limited by their natural passive response, their performance is restricted to very specific applications [11, 26]. In contrast, the ability to control the optical response *in-operando* readily enables dynamic switchable,

tunable, and reconfigurable optical functionality that facilitates promising applications such as modulation, routing, dynamic beam shaping, and adaptive optics [11, 27–29]. This dynamic control is introduced by the integration of active media into conventional metasurface designs. Liquid crystals [27, 30], graphene [31], phase-transition materials [32], and chalcogenide-based phase-change materials [33, 34] have been demonstrated to serve as active media; particularly the latter emerged as one of the most promising materials for tunable plasmonic [35] and photonic devices [28, 33, 36–42].

Phase-change materials – originally used for rewritable optical data storage [43–45] and recently for non-volatile electronic memories [46, 47] – provide the ability of reversible, repeatable, and rapid switching between amorphous and crystalline states upon external optical, electrical, or thermal stimuli [45, 48–52]. The resulting atomic rearrangement is typically associated with drastic changes in the electrical and optical properties. Hence, introducing phase-change materials for metasurfaces already enabled tunable perfect absorption [31, 38], reconfigurable flat lenses [28], and switchable plasmonic devices [35]. The most extensively studied phase-change materials are pseudo-binary $\text{GeTe-Sb}_2\text{Te}_3$ chalcogenide compounds, particularly $\text{Ge}_2\text{Sb}_2\text{Te}_5$.

Artificial phase coexistence of amorphous and crystalline regions within $\text{GeTe-Sb}_2\text{Te}_3$ thin films was demonstrated as an alternative to “traditional” metasurfaces, i.e., metal-like (crystalline) nanoresonators embedded in a dielectric (amorphous) surrounding. Using direct laser writing, comparable to conventional optical data storage, resulted in active photonic components with randomly accessible control over the optical properties of inherently flat, non-volatile phase-change material-based metasurfaces [28, 36]. Although such devices are promising alternatives to the traditional metasurfaces, the structure size for any element is yet diffraction-limited by the laser light source and the building blocks are restricted to binary states: amorphous and crystalline. The latter was recently overcome by the introduction of appropriate femtosecond laser pulses to achieve intermediate crystallized states [53–55], thus, enabling gradually tailorable optical properties in confined regions. To circumvent the diffraction-limit, this thesis introduces focused ion beam (FIB) irradiation to induce lattice disorder in initially crystalline $\text{Ge}_2\text{Sb}_2\text{Te}_5$ thin films in highly confined regions. While FIB milling was previously used to create reconfigurable metasurfaces [56, 57], it was demonstrated that lattice damage accumulation induced via ion irradiation leads to amorphization of phase-change materials [58–61]. Thus, the scope of this thesis is to gain a deep understanding of the effects of ion irradiation on the optical properties of $\text{Ge}_2\text{Sb}_2\text{Te}_5$. Moreover, three approaches were proposed and addressed to facilitate the integration of ion beam modified $\text{Ge}_2\text{Sb}_2\text{Te}_5$ thin films into active optical devices, such as metasurfaces. To illustrate these approaches, figure 1.1a schematically depicts the abrupt reflectivity increase upon thermal annealing (crystallization) of $\text{Ge}_2\text{Sb}_2\text{Te}_5$.

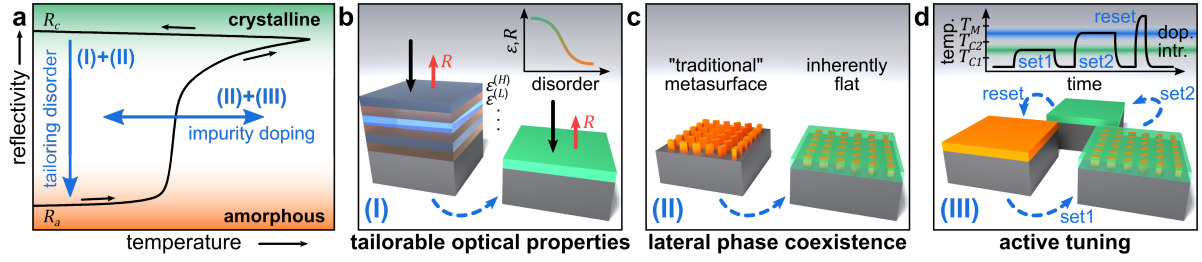


Figure 1.1.: (a) Temperature-dependent reflectivity upon heating and subsequent cooling of an amorphous $\text{Ge}_2\text{Sb}_2\text{Te}_5$ film, which is converted into the crystalline state. (b-d) Schematic drawings that visualize the key approaches proposed within the scope of this thesis: (I) tailorable optical properties, (II) artificial, lateral phase coexistence, and (III) active tuning of an optical functionality.

- (I) To achieve a desired optical response of a given optical element, typically optical coatings comprising multi-layer stacks of low-loss, thin films ($d \sim \lambda$) with alternating permittivity, i.e., high $\epsilon^{(H)}$ and low $\epsilon^{(L)}$ values, are fabricated, as shown in figure 1.1b. In this manner, they serve various applications such as high-reflective or anti-reflective coatings. It was recently demonstrated that ultra-thin lossy films can also efficiently suppress light reflection [62, 63]. The ability to control the amount of lattice disorder within $\text{Ge}_2\text{Sb}_2\text{Te}_5$ thin films leads to gradually **tailorable optical properties**. Thus, elaborate multi-layer coatings can be substituted by single $\text{Ge}_2\text{Sb}_2\text{Te}_5$ layers with tailorable optical responses. To investigate the applicability of this approach, it is therefore crucial to elucidate the effect of ion irradiation on the optical properties of $\text{Ge}_2\text{Sb}_2\text{Te}_5$.
- (II) Metasurfaces based on artificial lateral phase coexistence in $\text{Ge}_2\text{Sb}_2\text{Te}_5$ films are promising to surpass "traditional" metasurfaces comprising metallic/dielectric nanoantennas (compare figure 1.1c). Since this approach yields inherently flat devices, they readily facilitate the ability of multi-layer (stacked) metasurfaces with optical functionalities dedicated to each layer. Within this thesis, focused ion beam irradiation of highly confined regions in $\text{Ge}_2\text{Sb}_2\text{Te}_5$ films is used to achieve artificial, **lateral phase coexistence** with sizes well below the diffraction-limit of direct laser writing. Furthermore, by tailoring the amount of induced lattice damage and controlling the size and shape of the irradiated regions, gradual and local control of the optical properties of $\text{Ge}_2\text{Sb}_2\text{Te}_5$ becomes accessible, which enables grayscale patterning at the nanoscale granting a novel degree of freedom for the design of diverse optical elements and metasurfaces [64].
- (III) Another effective route to achieve artificial phase coexistence is the incorporation of impurity atoms in $\text{Ge}_2\text{Sb}_2\text{Te}_5$. Many studies revealed that impurities effectively

modify the phase-change of $\text{Ge}_2\text{Sb}_2\text{Te}_5$, i.e., they enhance the thermal stability of the amorphous phase. Thus, with the ability to create lateral doping variations, which is readily facilitated by spatially selective ion implantation, different activation energies, i.e., crystallization temperatures, can be obtained for intrinsic and implanted regions, as shown in figure 1.1d. Appropriate switching between the states would enable **active tuning** of lateral phase coexistence that can be accompanied with in- and out-tuning of an optical functionality.

Following the **Introduction** of this thesis, **Chapter 2 - Fundamentals** presents a basic overview of ion-matter interaction with emphasis on ion beam modification of diverse materials. It also introduces the class of phase-change materials and specifically provides fundamental material properties of the ternary chalcogenide $\text{Ge}_2\text{Sb}_2\text{Te}_5$, which is one of the most prominent phase-change materials. Thin film deposition, modification, and characterization techniques as well as simulations used within this thesis are described in **Chapter 3 - Experimental methods**. In **Chapter 4 - Intrinsic physical properties of GST thin films**, the structural and optical properties of as-deposited and annealed $\text{Ge}_2\text{Sb}_2\text{Te}_5$ thin films are investigated. Moreover, extracted optical permittivity values of all $\text{Ge}_2\text{Sb}_2\text{Te}_5$ phases are presented, which are published in reference [65] and in the bachelor thesis of Axel Printschler [66]. In the following three main chapters of this thesis, the previously identified key challenges are targeted.

Within **Chapter 5 - Tailoring disorder in GST thin films**, the effect of ion irradiation on the optical, electrical, and structural properties of initially crystalline $\text{Ge}_2\text{Sb}_2\text{Te}_5$ thin films is examined. It highlights various disorder-driven structural and electronic transitions in $\text{Ge}_2\text{Sb}_2\text{Te}_5$ that are observed via *in-situ* optical, electrical and *ex-situ* optical, structural measurements. The accompanied tailorable optical properties are utilized to achieve tailorable near-zero reflection by stacking $\text{Ge}_2\text{Sb}_2\text{Te}_5$ on a gold reflector. Parts of the results are published in reference [67], in the master thesis of Robin Schock [68], and in the bachelor thesis of Axel Printschler [66].

Chapter 6 - Artificial phase coexistence enabled by ion beam patterning introduces spatially selective ion irradiation of $\text{Ge}_2\text{Sb}_2\text{Te}_5$ thin films via a focused ion beam system in order to tailor disorder in tightly confined regions. The resulting artificial, lateral phase coexistence is used to demonstrate an anisotropic metasurface exhibiting dichroism. Furthermore, this chapter demonstrates, that grayscale patterning at the nanoscale can be achieved based on the limits of ion beam patterning. Parts of this chapter are published in references [65, 67].

The modification of the phase-change of as-deposited $\text{Ge}_2\text{Sb}_2\text{Te}_5$ via ion beam impurity doping is presented in **Chapter 7 - Ion beam impurity doping of GST for active optical devices**. Opposing effects on the thermal stability of doping and changes in

the local order upon ion implantation of most of the group V elements are discussed. The results demonstrate active in- and out-tuning of artificial phase coexistence via spatially selective ion implantation of $\text{Ge}_2\text{Sb}_2\text{Te}_5$. Parts of this chapter are published in the master thesis of Robin Schock [68] and the bachelor thesis of Jacob Grandmontagne [69].

Finally, the main results obtained in this thesis are summarized in **Chapter 8 - Conclusion and outlook** and future work is motivated.

2. Fundamentals

Within this chapter an overview of ion beam modification of materials is provided. Furthermore, the class of phase-change materials is introduced and fundamental material properties of $\text{Ge}_2\text{Sb}_2\text{Te}_5$ are presented.

2.1. Ion beam modification of solids

Ion implantation, i.e., the deliberate incorporation of impurities into solids (doping) via accelerated ion beams, allows to modify the electrical, optical, structural, mechanical or chemical properties of various materials [70]. Thus, ion beam modification serves for a variety of research topics and applications besides standard semiconductor technology, i.e., for nanostructure engineering and advanced electro-optical devices [71–75]. Two mechanisms lead to a deceleration of penetrating ions into the solid depending on the ions' energy; nuclear energy loss arises from elastic collisions between impinging ions and target nuclei, while electronic energy loss is caused by inelastic scattering of the ions with target electrons. Electronic energy loss is dominant in the regime of high ion energies, i.e., above ~ 1 MeV per nucleon, causing the formation of severe irradiation damage or ion tracks through the intense local ionization of target atoms [76]. In the low energy regime however, thus below ~ 500 keV, nuclear collisions dominate the energy transfer from ions to lattice atoms. Displacements of atoms from their lattice sites occur upon elastic collisions with a sufficient energy transfer to overcome the atoms' displacement energy E_d , which is typically some ten eV [77]. As common ion energies for implantation significantly exceed E_d , the residual kinetic energy of a primary knock-on atom (recoil) is sufficient for further displacements (secondary knock-ons, etc.). Such a resulting collision cascade is schematically depicted in figure 2.1a for a representative GeSbTe compound film. Moreover, the displacement of atoms from their lattice sites (vacancy, either $V_{\text{Ge/Sb}}$ or V_{Te} , compare section 2.3.1) and subsequently their occupation of interstitial sites corresponds to the formation of point defects. Such a vacancy-interstitial defect is called Frenkel pair. The formation of extended defects, that are defect clusters, dislocation loops, and stacking faults, or even amorphous regions may be caused by dense or accumulation of multiple collision cascades. Furthermore, nuclear collisions can lead to the ejection of target atoms (sputtering) near the surface considering sufficient energy transfer to overcome their surface binding energy, which can cause a significant erosion for high ion fluences. Additionally, nuclear and electronic energy losses are balanced at intermediate ion

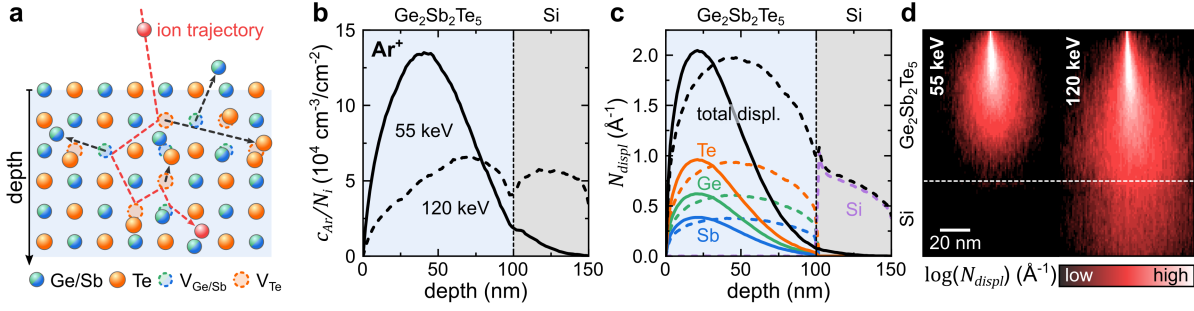


Figure 2.1.: (a) Schematic representation of lattice displacements within a GST compound due to a nuclear collision cascade caused by an impinging energetic ion. (b,c) Ar concentration depth profile c_{Ar} normalized to ion fluence N_i (b) and corresponding number of displaced lattice atoms per incident ion N_{displ} (c) for an Ar^+ -ion irradiated $\text{Ge}_2\text{Sb}_2\text{Te}_5$ film on Si at 7° incidence angle with ion energies of 55 keV (solid line) and 120 keV (dashed line), respectively. (d) Two dimensional distribution of total N_{displ} for the irradiations of (b,c).

energies, which leads either to increased damage production or to competitive recovery processes [76]. However, the atomic mobility at elevated temperatures, i.e., mobile defects, may cause defect migration and recombination reducing the amount of created residual lattice damage. While ion irradiation damage is commonly regarded as detrimental and requires subsequent appropriate annealing processes, it can be also utilized for a desired modification of the structural properties of various materials (defect engineering [78–80]).

Each incident ion will follow an unique ion trajectory and eventually loose all of its kinetic energy due to the successive energy transfer to lattice atoms. It comes to rest after a certain distance denoted penetration depth, which clearly depends on the ion energy, mass and target density. While single ions are impossible to anticipate, the large ensemble of ions typically implanted enables statistical prediction of mean penetration depths. Within this thesis, the common Monte Carlo-based software package collection SRIM (Stopping and Range of Ions in Matter [81]) was used to simulate the spatial distribution of ions and displacements in solids averaged over large numbers of cascades.

Figure 2.1b depicts the Ar concentration (normalized to ion fluence, i.e., number of implanted ions per unit area) as a function of depth for an Ar^+ -ion irradiated $\text{Ge}_2\text{Sb}_2\text{Te}_5$ film on Si simulated via SRIM. Here, two ion energies were used for comparison. Most of the Ar^+ -ions remain in the film with a maximum concentration (denoted as projected ion range R_p) centered in the middle of the film for 55 keV; the width of the distribution is commonly known as projected range straggle. A significant amount of Ar^+ -ions reaches the substrate for increasing the ion energy to 120 keV. This gives rise to the effect of ion beam induced interface mixing at the boundary layer for the irradiation of such thin films [82]. Yet interface alloying can be advantageous in

some cases [83–85].

The defects created within the solid can be also estimated via SRIM simulations and are shown in figure 2.1c. The total number of displaced lattice atoms per incident ion and unit length N_{displ} comprises the contributions of each displaced lattice atom species, i.e., in this case Ge, Sb, and Te. Evidently the maximum in N_{displ} is shifted towards the samples' surface compared to the Ar distribution independent of the ion energy. However, while lattice damage is absent in the Si substrate for the lower ion energy (55 keV), a significant amount of Si displacements occur for the higher ion energy (120 keV). This further corroborates interface mixing.

The lateral distribution of ions and thus lattice displacements is crucial for any ion beam based patterning. Therefore, figure 2.1d depicts the two-dimensional distribution of the total N_{displ} on an logarithmic scale. The width of the lateral Ar distribution (not shown) in the direction perpendicular to the surface normal is referred as lateral straggling (here, ~ 30 nm and ~ 50 nm for 55 keV and 120 keV, respectively), which is accompanied with a broadening of the total N_{displ} (yet smaller than lateral straggling). Both effects, thus, limit any structure size of spatially selective ion irradiation for either impurity doping or defect engineering.

2.2. Phase-change materials

At least theoretically, almost any material can be condensed into two distinct states – amorphous and crystalline. While the latter comprises highly ordered atoms or molecules forming a crystal lattice that fulfills the translational symmetry¹, amorphous solids lack this long-range order but may exhibit a predictable arrangement of the atoms in the short-range. Thus, phase transitions between amorphous and crystalline states may occur for numerous materials. The class of phase-change materials (PCMs), however, is unique in that the phase transition at elevated temperatures can be exceptionally fast in combination with highly stable structural phases at ambient conditions [45]. Furthermore, the structural conversions are accompanied with electronic transitions for most PCMs, which results into distinct differences of the electrical and optical properties of the various phases facilitating their use in non-volatile electronic memory, optical or photonic data storage [42, 45, 46, 87–90].

¹For clarity, with the discovery of quasicrystals, which lack translational symmetry, the definition of crystals was extended to any solid that possesses an essentially discrete diffraction pattern [86].

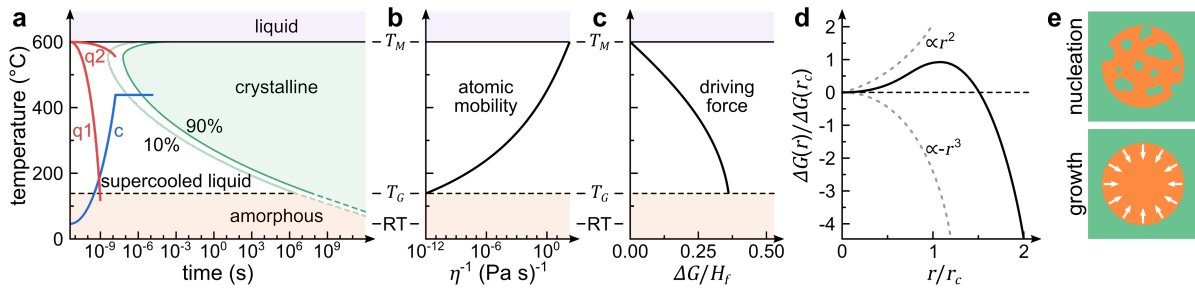


Figure 2.2.: (a) Schematic depiction of a time-temperature-transformation diagram for a representative PCM. (b,c) Temperature-dependent atomic mobility (b) that is related to the reciprocal viscosity η and the difference in Gibbs free energy ΔG (c) between (supercooled) liquid and crystal in units of the heat of fusion H_f . (d) Energy gain for the formation of a crystalline nucleus (spherical shape) within an amorphous matrix as a function of nucleus radius. Panels (a-d) are adapted from reference [91]. (e) Schematic crystallization pattern for nucleation-dominated (top) and growth-dominated recrystallization (adapted from reference [92]).

2.2.1. Amorphization and glass formation

A typical time-temperature-transformation diagram is schematically depicted in figure 2.2a for a representative PCM. The principle of the phase-change in PCMs is a consequence of the peculiar interplay of the temperature-dependent atomic mobility and Gibbs free energy G shown in figure 2.2b and c, respectively [91]. While the microscopic atomic mobility is inversely related to the macroscopic viscosity η of a liquid (Stokes-Einstein relation), the driving force for the phase transition is given by the difference in Gibbs free energy ΔG between the phases. Thus, the phase that minimizes G is present in thermal equilibrium; however, on small timescales equilibrium conditions are inhibited by the finite atomic mobility enabling a glassy state by rapid quenching of a supercooled liquid. Cooling a melt below its melting point (T_M , typically around 600 °C) causes a high atomic mobility; yet crystallization is retarded since its driving force (ΔG) is rather low. Thus, for sufficiently fast quenching of the melt with a constant rate (typically 1×10^{10} K/s; q1 in figure 2.2a) crystallization can be avoided. While for low temperatures the driving force increases, the atomic mobility vanishes, which again inhibits the crystallization process. Further cooling below the glass transition temperature T_G thus leads to a remaining amorphous material (glass). However, for rather slow cooling rates (q2 in figure 2.2a) partial crystallization may occur. Note that the shape of the crystallization regime in figure 2.2a strongly depends on the temperature-dependent viscosity. As glasses formed by melt-quenching are clearly out of thermal equilibrium, relaxation towards equilibrium conditions occur on timescales that depend on the temperature. While long-time stability against crystallization at ambient conditions is required for data retention in storage devices, fast crystallization within a fraction of seconds grants high device speed.

2.2.2. Crystallization process

Crystallization of amorphous materials is based on two mechanisms – nucleation and growth. While nucleation corresponds to the formation of crystalline nuclei within the amorphous matrix, their phase fronts, that separate amorphous and crystalline regions, progress denoted as growth. Again the driving force for crystallization is the minimization of Gibbs free energy. An annealing processes starting at room temperature (RT) is indicated (c, blue line) in figure 2.2a. An interface between the phases has to be established caused by the formation of a crystalline nucleus within an amorphous matrix. As the nucleation process is commonly described in a continuum-approximation, i.e., the discrete atomic structure is neglected, thus, modeling of nucleus formation and growth of a (continuous) interface is enabled [93, 94].

The free energy difference $\Delta G(r)$ for a spherical crystalline nucleus with radius r embedded in an amorphous material can be described using classical nucleation theory [95] as:

$$\Delta G(r) = V(r)\Delta G_V + A(r)\sigma . \quad (2.1)$$

Here, $V(r)$ and $A(r)$ correspond to the volume and surface area of the nucleus, while ΔG_V equals the difference in G between the phases per unit volume and σ resembles the interfacial energy per unit surface area. Thus, the interplay of the energy gain due to the volume ($\propto -r^3$) of the nucleus and the energetic expense of establishing the interface ($\propto r^2$) dominate the formation of nuclei, which is depicted in figure 2.2d. The point of maximal $\Delta G(r)$ is denoted as critical radius r_c :

$$r_c = \frac{2\sigma}{|\Delta G_V|} . \quad (2.2)$$

Therefore, the thermally fluctuating size of the nuclei determines whether they tend to grow ($r > r_c$) or dissolve ($r < r_c$). The latter is caused by the removal of the interface, i.e., a reduction of the free energy. A steady-state nucleation rate I_{SS} and a growth rate $u(T)$ for nuclei with $r \gg r_c$ correspond to [96]

$$I_{SS}(T) \propto \eta(T)^{-1} \exp\left(-\frac{\Delta G(r_c)}{k_B T}\right) \text{ and} \quad (2.3)$$

$$u(T) = \frac{\partial r}{\partial t} \propto \frac{T}{\eta(T)} \left[1 - \exp\left(-\frac{\Delta G(T)}{k_B T}\right)\right] . \quad (2.4)$$

As both rates are indeed temperature dependent, their respective maximal values are reached at different temperatures. Thus, their contribution differs with one process being dominant, which lead to the sub-classification of PCMs into nucleation- or growth-dominated crystallization; schematic crystallization pattern of an amorphous region within a crystalline matrix for both classes are depicted in figure 2.2e. While

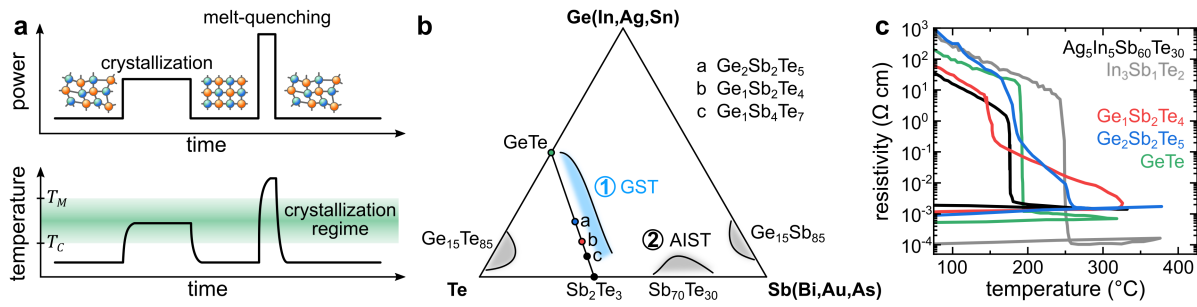


Figure 2.3.: (a) Induced power and corresponding temperature evolution for crystallization and amorphization of PCMs (adapted from reference [94]). (b) Ternary phase diagram illustrating various prominent PCMs (adapted from reference [87]) (c) Temperature dependent resistivity of selected PCM thin films. Values are taken from references [99–101].

the crystallization speed might not depend on the volume of the amorphous region for nucleation-dominated crystallization, such volume dependence can be observed in growth-dominated materials [97]. Here, the time for crystallization drastically decreases with decreasing volume.

Repeatable switching between distinct stable states of a PCM can be achieved by applying external thermal, electrical, or optical stimuli, which is schematically depicted in figure 2.3a. Heating the PCM to a temperature above its crystallization temperature (T_C ; often estimated to be equal to the glass temperature) but well below its melting point (T_M) for a sufficient period of time (moderate power pulse for tens of nanoseconds [51, 98]) leads to crystallization, while amorphization is accomplished through melting (high power pulse below 10 ns [48, 52, 98]), i.e., heating above T_M and subsequently rapid cooling as fast that the time frame within the crystallization regime is sufficiently short. Typically, electrical or optical, low power pulses are further used to read-out the state of the PCM.

2.2.3. Typical phase-change materials

A variety of chalcogenide based PCMs have been discovered over the past decades while some of the most prominent can be classified in a ternary phase diagram shown in figure 2.3b. One of the first candidates that showed an electrical contrast between the amorphous and crystalline state were Te-based eutectic alloys ($Ge_{15}Te_{85}$) [43], yet their transitions were rather slow ($\sim \mu s$). Drastically increasing crystallization speeds accompanied with a distinct optical contrast were found for GeTe [102] with the extension to pseudo-binary GeTe–Sb₂Te₃ alloys [44, 48] (GST; group (1) in figure 2.3b). Another group of PCMs that are frequently used in re-writable optical storage media are Sb–Te binary compounds doped with small amounts of Ag, In and/or Ge [103, 104] – such as Ag₅In₅Sb₆₀Te₃₀ (AIST; group (2) in figure 2.3b). The groups are

classified according to their re-crystallization behavior: while PCMs of group (1) were found to possess a nucleation-dominated crystallization, group (2) materials showed a growth-dominated process [92]. Furthermore, Ge-doped Sb ($\text{Ge}_{15}\text{Sb}_{85}$) were also found to possess decent PCM characteristics [105]. Representative temperature dependent resistivity measurements of some of the aforementioned PCMs are depicted in figure 2.3c demonstrating their high electrical contrast (several orders of magnitude) between insulating, amorphous and metal-like, crystalline phases.

2.3. $\text{GeTe-Sb}_2\text{Te}_3$ pseudo-binary compounds - GST

Stoichiometric GST compounds comprising a pseudo-binary mixture of $(\text{GeTe})_m(\text{Sb}_2\text{Te}_3)_n$ (m, n being integer values) are one of the most extensively studied and widely used PCM. Besides the prominent ternary compounds $\text{Ge}_1\text{Sb}_2\text{Te}_4$ ($m=1, n=1$) and $\text{Ge}_1\text{Sb}_4\text{Te}_7$ ($m=1, n=2$), $\text{Ge}_2\text{Sb}_2\text{Te}_5$ ($m=2, n=1$) is the matter of choice within the scope of this thesis. However, the exceptional properties of these materials are quite similar [106, 107].

2.3.1. Crystallographic and electronic structures of $\text{Ge}_2\text{Sb}_2\text{Te}_5$

Local order of the amorphous phase Zallen proposed that the atomic arrangement within common amorphous solids closely resembles the corresponding crystalline structure [108]. While the amorphous state lacks long-range order, still there may be strict rules for the arrangement on short-range [45]. However, the local atomic arrangement of PCMs is still a matter of debate. Kolobov *et al.* concluded from EXAFS and XANES² spectroscopy at $\text{Ge}_2\text{Sb}_2\text{Te}_5$ that Ge atoms are either tetrahedrally or octahedrally coordinated in the amorphous or crystalline phases, respectively, which indeed corresponds to considerably different local atomic arrangements [109]. While subsequent reports on Raman spectroscopy [110, 111], X-ray fluorescence holography [112], and density-functional theory simulations [113] even corroborated this model, it was controversially discussed in literature [45, 114–116]. Jovari *et al.* proposed that the local arrangement of amorphous $\text{Ge}_2\text{Sb}_2\text{Te}_5$ is determined by two opposing effects, which are, first, that the 8– N rule (N is the number of valence electrons) should be satisfied by most atoms and, second, bonds that are prohibited in the crystalline phases should be avoided [116, 117]. However, they observed the formation of Ge-Ge and Ge-Sb bonds (indeed not present in crystalline GST; see next paragraph) that is sufficient to satisfy the 8– N rule, while no Sb-Sb or Te-Te bonds were found. In another study on reverse Monte Carlo simulations from Kohara *et al.* with synchrotron-radiation X-ray diffraction data, bond angles of $\sim 90^\circ$ and no evidence for homopolar bonds

²Extended X-ray absorption fine structure and X-ray absorption near-edge spectroscopy

were observed [118]. Further, they proposed even-folded ring structures to be the characteristic building blocks of amorphous Ge₂Sb₂Te₅ corroborating the preference of heteropolar bonds. Each ring consists of an alternation of A (Ge/Sb) and B (Te) atoms indicating chemical ordering.

The very distinct findings from experimental perspectives lead to numerous molecular-dynamics simulations, which were performed to enable further insights into the local atomic arrangement of amorphous Ge₂Sb₂Te₅ [114, 119–124]. In conclusion of these works, chemical ordering (occurrence of ABAB rings) is confirmed, but is associated with a significant amount of homopolar (Ge-Ge) and Ge-Sb bonds. Bond-angles of –Ge(Sb)–Te–Ge(Sb)– are also found to distribute around $\sim 90^\circ$. The 8–N rule, however, tends to be unsatisfied with considerable larger coordination numbers (yet below 6); thus, most of Ge and Sb (four-fold coordinated) and the three-fold coordinated Te are mainly located at defective octahedral sites [114]. Moreover, about one third of Ge locates within tetrahedral environments, which is favored by the presence of homopolar bonds. Note that so far a unique amorphous phase was considered, yet polymorphism of amorphous Ge₂Sb₂Te₅ was reported [115, 125]. In particular, as-deposited samples show predominantly tetrahedrally coordinated Ge with an increased amount of homopolar and Ge-Sb bonds compared to melt-quenched samples, which is accompanied with a reduction of ABAB rings.

Crystallographic structures Ge₂Sb₂Te₅, like most of the GeTe–Sb₂Te₃ pseudo-binary compounds, crystallizes into a metastable cubic and a stable trigonal crystal system, respectively. The metastable phase comprises face-centered cubic (fcc) unit cells with space group $Fm\bar{3}m$ and cubic lattice constant of $a_{cub} = 6.0177(5) \text{ \AA}$ ($\alpha = 90^\circ$) [126], which is schematically depicted in figure 2.4a. While octahedrally coordinated Te atoms form a fcc sublattice itself occupying one (anion-like) lattice site at $a_{cub}(1/2, 1/2, 1/2)$ of a rock-salt-like structure, Ge and Sb randomly occupy the second (cation-like) lattice site at $(0, 0, 0)$ [87, 126–128]. Due to uneven numbers of Ge and Sb compared to Te, the residual lattice sites are thus (randomly) unoccupied leading to a considerable large amount of inherent vacancies ($\sim 20\%$ on the Ge/Sb sublattice) within Ge₂Sb₂Te₅. Wuttig *et al.* demonstrated via *ab initio* density-functional theory (DFT) simulations that the removal of Ge and/or Sb atoms from an ideal Ge₂Sb₂Te₄, i.e., vacancy free, system leads to a decrease in formation energy caused by a reduced occupation of anti-bonding states (present in Ge₂Sb₂Te₄) [87, 128]. Thus, the formation of inherent vacancies within Ge₂Sb₂Te₅ is indeed energetically favorable unlike typical positive vacancy formation energies of common semiconductors [129]. Furthermore, the formation of *p*-bonds in GST compounds causes their octahedral atomic arrangement; thus, a pronounced Peierls distortion of the rock-salt phase is evoked by considerable displacements of Ge

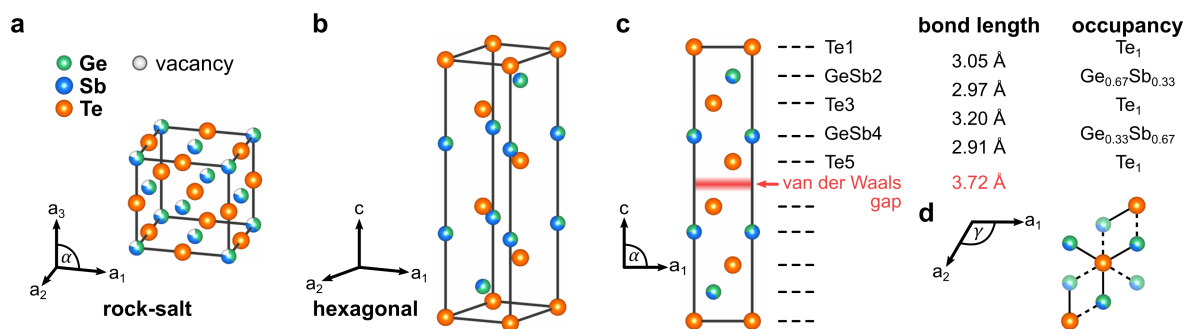


Figure 2.4.: (a,b) Crystal structures of crystalline $\text{Ge}_2\text{Sb}_2\text{Te}_5$ phases: (a) rock-salt [126] and (b) hexagonal structure. (c) Side view of the hexagonal unit cell depicting the stacking sequence to illustrate the van der Waals gap. Bond lengths and occupancies for each layer are taken from Urban *et al.* [131]. (d) Schematic to display 3 + 3 coordination of Te3 ((c),(d) adapted from reference [131]).

and Sb from their ideal lattice sites leading to a further significant energy gain [109, 130].

In the stable crystalline phase, $\text{Ge}_2\text{Sb}_2\text{Te}_5$ has a hexagonal unit cell (space group $P\bar{3}m1$) with lattice parameters $a_{1,2} = 4.2257(2) \text{ \AA}$, $c = 17.2809(18) \text{ \AA}$, $\alpha = 90^\circ$, and $\gamma = 120^\circ$ [131] as shown in figure 2.4b. The atomic arrangement is not trivial. Petrov *et al.* [132] proposed cubic close packed stacking (*abcabc*) in a 9-layered sequence comprising pure Te-Sb(Ge)-Te-Ge(Sb)-Te-Te-Ge(Sb)-Te-Sb(Ge)- basal planes along the *c*-axis (stacking with atoms in parenthesis was reported by Kooi & De Hoosen [133]). However, more recent studies from Matsunaga *et al.* [134] and Urban *et al.* [131] suggested randomly occupied Ge and Sb layers; both studies revealed that Ge atoms favor the GeSb2 site while Sb prefers the GeSb4 site as marked in figure 2.4c. Furthermore, there is a large separation between the two adjacent Te layers (Te5) corroborated by the significantly larger bond length ($\sim 3.7 \text{ \AA}$) compared to the Ge/Sb-Te bond lengths ($\sim 3 \text{ \AA}$) [131]. This ordered vacancy layer [135, 136] is accompanied with weak van der Waals forces between low (3) coordinated Te atoms (van der Waals gap) [137]. The low coordination of Te5 is corroborated by the shortened GeSb4-Te5 bond length next to the gap and gives rise to the higher occupancy of Sb ($\sim 67\%$) on the GeSb4 site; Sb has three *p*-electrons (compared to two of Ge) favoring the charge balancing with Te5. Moreover, while Te1 (like all Ge and Sb atoms) is octahedrally coordinated, Te3 exhibits a 3 + 3 coordination [131], which is depicted in figure 2.4d.

Electronic structures Figure 2.5a schematically depicts the density of states for the amorphous, rock-salt, and hexagonal phase of $\text{Ge}_2\text{Sb}_2\text{Te}_5$. Generally, the electronic density of states is quite similar for all phases, which is a consequence of an overall structural similarity between crystalline and amorphous phases. It was reported that the valence band (bonding states) comprises mainly Te lone-pair electrons, while the

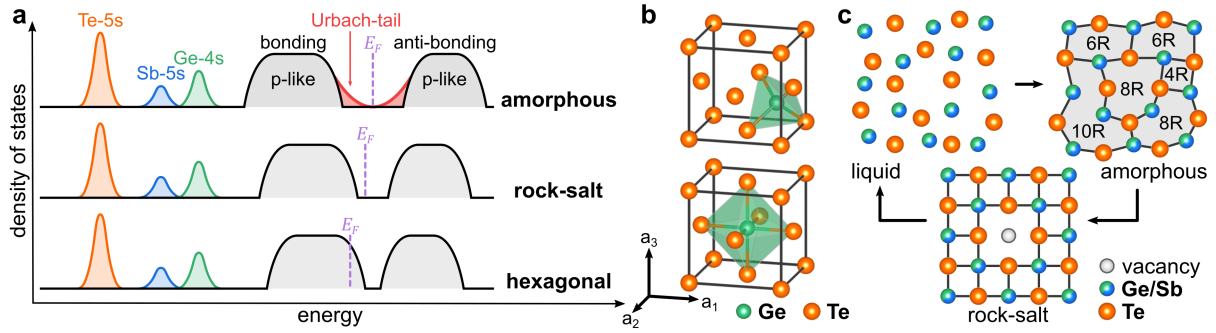


Figure 2.5.: (a) Schematic electronic density of states depicted for the amorphous, rock-salt, and hexagonal phase of Ge₂Sb₂Te₅, respectively (adapted from reference [91]). (b) Simplified unit cells depicting the Te fcc sublattice with one single Ge atom that is either tetrahedrally (top) or octahedrally (bottom) coordinated to illustrate the umbrella-flip model between amorphous and crystalline phases (adapted from reference [109]). (c) Schematic depiction of the possible ring size transformation upon phase-changes from crystalline to liquid to amorphous to crystalline (rock-salt) (adapted from reference [118]).

conduction band consists of anti-bonding states of Ge-Te and Sb-Te for all phases, respectively [138]. Ge (4s), Sb (5s), and Te (5s) each contribute two s-electrons leading to s-like states that are well separated from the p-like states. The p-like bonding and anti-bonding states are separated by an energy gap; the size and nature of the gap varies for the different phases. However, slight interaction of s-states [139] accompanied with broad superimposed p-states hint in principle p-bonding in these materials.

While the largest energy gap is observed for the amorphous phase ($E_g \approx 0.7$ eV) [140–143], here the Fermi-level is located midgap revealing semiconducting behavior. However, additional states are located within the band gap that are a result of localized states (Te lone-pairs) in highly disordered media, which is denoted as Urbach tail [106, 144, 145]. P-type semiconducting properties were found for the rock-salt like phase accompanied with a decrease of the gap to about 0.5 eV [140, 143, 146]. Here, acceptor-like trap states evoked by the presence of non-stoichiometric excess vacancies – separate from the inherent vacancies of Ge₂Sb₂Te₅ – on the cation-like sublattice lead to a shifted Fermi-level towards the valence band [122, 142, 147–149]. A further shift of the Fermi-level deep inside the valence band is observed for the hexagonal phase indicating a degenerate p-type semiconductor [140]. This behavior is caused by the formation of a defect band due to the ordered vacancy layers (van der Waals gaps) within the hexagonal structure. Despite some calculations yielded semi-metal conduction [138], there is still a narrow electronic gap accompanied with an even larger optical gap due to the Burstein-Moss-effect [150, 151].

2.3.2. Atomistic description of the phase-change in $\text{Ge}_2\text{Sb}_2\text{Te}_5$

The umbrella-flip model As discussed in the previous section, Kolobov *et al.* proposed that Ge is either present in a tetrahedral or octahedral lattice site for the amorphous or crystalline phase, respectively. This further lead to an appealing atomistic model – the umbrella-flip model [109] – that describes the phase-change of GST compounds, i.a. $\text{Ge}_2\text{Sb}_2\text{Te}_5$. Here, the main structural rearrangement upon crystallization is thus a flip of Ge from tetrahedral to octahedral lattice sites, which is schematically depicted in figure 2.5b in a simplified unit-cell comprising the Te fcc sublattice and one single Ge atom. While the change in bonding accounted for the property contrast accompanying the phase-change, the little atomic rearrangement intuitively explained the rapid crystallization kinetics of such PCMs. However, typically the amount of tetrahedrally coordinated Ge is small at about one third in the amorphous phase as already discussed before. Moreover, Ge is also associated with homopolar Ge-Ge or Ge-Sb bonds instead of only in Ge-Te bonds as it is proposed in the umbrella-flip model. Thus, this model is likely unrealistic to describe the phase-change in GST compounds despite gaining substantially attention [45, 110–116] as it is also not applicable to PCMs without Ge.

Evolution of ring-statistics A more universal model is conceived by another qualitative rather statistical evaluation of the structural differences/similarities of amorphous and rock-salt $\text{Ge}_2\text{Sb}_2\text{Te}_5$. As was already discussed, both the amorphous and rock-salt phase comprise AB-alternating even-folded rings, which is schematically depicted in figure 2.5c (top right). Moreover, preferential octahedral coordination and the average bond-angle of $-\text{Ge}(\text{Sb})-\text{Te}-\text{Ge}(\text{Sb})-$ ($\sim 90^\circ$) found in the amorphous state resemble that in the cubic crystalline state [118]. Thus, the amorphous phase can be regarded as a strongly distorted version of the rock-salt phase to a first approximation. While little distortions can be present in the crystalline state, such strong distortions clearly exceed these and lack any long-range order. Within this model, again (like in the umbrella-flip model) only small structural rearrangements are necessary giving rise to the fast crystallization. Furthermore, decreasing the amount of homopolar bonds and the amount of tetrahedrally coordinated Ge-atoms that impede the crystallization process is likely the most significant occurring rearrangement. The evolution of ring-statistics may thus allow for a atomistic description of the crystallization of the amorphous phase [49, 118, 152, 153]. Molecular dynamics simulation of an entire phase-change cycle, i.e., melt-quenching and recrystallization of $\text{Ge}_2\text{Sb}_2\text{Te}_5$ shown in figure 2.5c, revealed indeed a decrease in the amount of homopolar bonds and an increase of the near-regular four-fold ABAB-rings [121]. These findings did corroborate that the ring-statistics model provides a concise description of the phase-change in $\text{Ge}_2\text{Sb}_2\text{Te}_5$.

2.3.3. Metal-insulator transition in Ge₂Sb₂Te₅

Up to here, only the transition from amorphous to rock-salt phase via crystallization was discussed. However, since the rock-salt phase of Ge₂Sb₂Te₅ is metastable, i.e., not the most energy favorable configuration, but can be stable over a long period of time at ambient conditions, a further transition towards the stable hexagonal phase is expected. This conversion from rock-salt to hexagonal phase was found to be accompanied with a pronounced change in the electrical transport properties [100], i.e., a transition from insulating to metallic behavior (discussed in detail in the next section). Although, such a metal-insulator-transition (MIT) can be typically deduced to a structural rearrangement, it may occur independent on a change in crystal structure and for that two distinct mechanisms were proposed. Mott suggested that strong electron correlations lead to charge carrier localization; thus, an electronically driven MIT occurs if the electron interaction energy exceeds the Fermi energy [154]. Contrary, localized electronic states at the Fermi energy caused by strong disorder were proposed by Anderson (Anderson-localization) [155]; thus, reducing disorder in the system drives the MIT due to delocalization. Although, both concepts can explain insulating behavior in many systems, the effects on electron correlation and disorder are difficult to disentangle experimentally.

The rock-salt phase possesses a significant amount of atomic disorder, which are a high concentration of inherent vacancies, randomly distributed Ge, Sb and inherent vacancies on the cation-like sublattice, and considerable displacements of Ge and Sb from their ideal lattice sites [48, 156]. Thus, the electronic properties clearly correlate with this atomic disorder with the addition of small amounts of other defects, i.e., excess vacancies or anti-site defects [42, 136]. Moreover, the insulating behavior of the disordered rock-salt phase can be explained by Anderson-localization, because electron–electron correlation effects are shown to be weak in PCMs [143, 157]. Indeed, electron localization was observed in low-temperature transport experiments [100, 158, 159], while DFT simulations revealed that the localization of electrons near the Fermi level is caused by random distribution of inherent vacancies accompanied with the formation of vacancy clusters [160].

As the stable hexagonal structure comprises vacancy layers resembling the van der Waals gaps, vacancy clusters of the disordered rock-salt phase dissolve and vacancies diffuse into the cation-like layers upon thermal annealing. DFT simulations from Zhang *et al.* further revealed that vacancy ordering triggers several transitions in crystalline Ge₁Sb₂Te₄ [160] (comparable to Ge₂Sb₂Te₅ [161]). First, a structural conversion from the metastable rock-salt phase to the stable hexagonal phase is observed for decreasing disorder; second, further vacancy ordering then drives the MIT (here a transition from

insulating to metallic behavior; to avoid confusion) before complete vacancy layers are formed. The disorder-driven MIT, which was evidenced by both experiments [100, 158, 159] and simulations [160, 161] of crystalline PCMs, between disordered and ordered GST indicates a purely electronically-driven transition that is disentangled from any crystallographic transition. These findings are further corroborated experimentally by the fabrication of cubic GST samples with ordered vacancy layers also showing metallic behavior [162–165].

2.3.4. Electrical and optical properties of $\text{Ge}_2\text{Sb}_2\text{Te}_5$

Electrical properties Figure 2.6a depicts the resistivity change of a representative $\text{Ge}_2\text{Sb}_2\text{Te}_5$ thin film upon heating and subsequently cooling [101]. The as-deposited, amorphous film shows a high resistivity that decreases upon thermal annealing. The negative slope ($d\rho/dT < 0$) is characteristic for insulating behavior. A drastic drop occurs at $\sim 180^\circ\text{C}$ that is related to the crystallization into the rock-salt phase. Further heating of the film reveals a second decrease in resistivity resembling the MIT [100]. Subsequently, the sample was cooled towards room temperature; here, a positive slope ($d\rho/dT > 0$) was observed, which indeed corroborates the transition into a metal-like state. The insulating behavior of the rock-salt phase is indicated by the dashed line in figure 2.6a (also with $d\rho/dT < 0$). The concentration of non-stoichiometric excess vacancies that lead to the p-type semiconducting rock-salt and hexagonal phase was found to be ~ 0.1 at.% [122, 148, 149]. Note that the excess vacancies are different from the inherent vacancies discussed in section 2.3.1. Although, the presence of such excess vacancies corroborates the high hole carrier concentration of $\sim 1 \times 10^{20} \text{ cm}^{-3}$ similar in both crystalline phases, they could not explain the observed distinct different transport properties. Hall and van der Pauw measurements by Siegrist *et al.* revealed an increase in carrier mobility of two orders of magnitude between rock-salt and hexagonal $\text{Ge}_1\text{Sb}_2\text{Te}_4$ [100] (also applicable to $\text{Ge}_2\text{Sb}_2\text{Te}_5$). As discussed before, the reduction of disorder in the rock-salt phase upon thermal annealing triggers the Anderson-like MIT, which is accompanied with delocalization of holes. This delocalization that occurs upon the disorder-driven MIT leads eventually to the enhanced carrier mobility in the hexagonal phase, which is responsible for the electrical resistance change.

Optical properties One of the key features of PCMs is their exceptional optical contrast between amorphous and crystalline phases. Such a pronounced optical contrast is also observed for $\text{Ge}_2\text{Sb}_2\text{Te}_5$. Figure 2.6b and c show the real and imaginary part of the permittivity for amorphous, rock-salt and hexagonal $\text{Ge}_2\text{Sb}_2\text{Te}_5$, respectively. The spectra of all phases are dominated in the visible to NIR spectral region by their

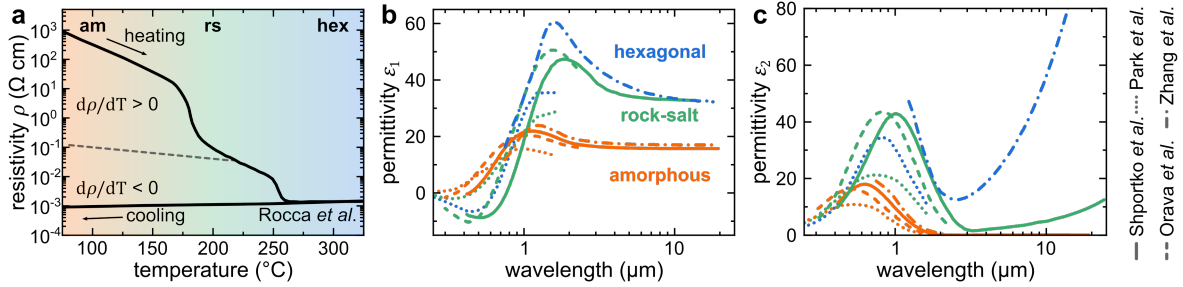


Figure 2.6.: (a) Temperature dependent resistivity of a Ge₂Sb₂Te₅ thin film. Values are taken from reference [101]. (b,c) Real ϵ_1 (b) and imaginary part ϵ_2 (c) of the complex permittivity of Ge₂Sb₂Te₅ for the amorphous (orange), rock-salt (green), and hexagonal phase (blue), respectively. Different values taken from references [107, 143, 167, 168] are given for comparison.

interband transitions, which were discussed before; however, especially the metal-like hexagonal phase shows a strong Drude-contribution in the IR that is a result of the high hole concentration accompanied with the high carrier mobility (low scattering time). A minor Drude-contribution was also observed for the rock-salt phase. The origin of the contrast is still under debate. However, recent studies proposed that the different optical properties arise from the distinct atomic arrangements between the structural phases [109, 113, 166].

Form the comparison of some literature data of the Ge₂Sb₂Te₅ permittivity [107, 143, 167, 168], it becomes evident that, while the overall shape is similar, the actual values vary significantly especially for the crystalline phases. The latter is likely caused by different fabrication processes of the Ge₂Sb₂Te₅ films and their respective conversion into the crystalline phases. Thus, a more detailed investigation of the intrinsic optical properties of the Ge₂Sb₂Te₅ films prepared within this thesis is necessary and will be presented in section 4.4.

2.3.5. Engineering the phase-change

Doping during deposition While GST compounds among other PCMs are already commercially used in non-volatile electrical storage devices, yet they are limited by their high programming currents, relatively slow operating speeds, and restricted thermal stability to satisfy the demand for next-generation high-density data storage [169]. Thus, impurity doping of diverse elements is extensively investigated while mainly achieved by incorporation during growth. In particular, N- and C-doped Ge₂Sb₂Te₅ are already integrated in PCM-based devices [170–176] as they were found to decrease the resistivity and enhance the stability of the amorphous state, i.e., increasing data retention while decreasing power consumption. Furthermore, an increase in crystallization temperature was observed for a variety of doping elements, such as

Cu [177], Er [178], Si [179–181], O [182], As [183], and Zn [184]. Further elements are discussed to either decrease the amorphous phase' resistivity or enhance the operation speed [169, 185–189].

Tuning disorder As disorder in crystalline $\text{Ge}_2\text{Sb}_2\text{Te}_5$ is the driving force of the MIT, controlling its degree may facilitate multilevel resistance or reflectance states based on disorder-induced localization. Thus, apart from thermal annealing [100] a variety of approaches emerged in literature in which tuning disorder in GST compounds, among others, was achieved via laser and photonic excitation [190, 191], focused electron beam irradiation [192], chemical composition [159, 161], pressure [193–198], strain [199, 200], interface templates [162, 201, 202], electric field [203, 204], and voltage pulses [205–207].

Ion irradiation of GST compounds Ion irradiation readily facilitates precisely tailoring disorder in solids; thus, multiple studies investigated the effect of defect engineering of GST compounds [58–61]. For instance, Privitera *et al.* demonstrated that increasing disorder induced by Ar^+ -ion irradiation leads to progressive amorphization of rock-salt $\text{Ge}_2\text{Sb}_2\text{Te}_5$, while several structural and electronic transitions occur in the hexagonal phase [59]. For the latter, they proposed that vacancy disordering first drives the MIT – inverse to vacancy ordering upon thermal annealing – for low ion fluences and second a conversion from the hexagonal to rock-salt phase, which was corroborated with DFT simulations.

Furthermore, the effect of ion irradiation on the thermal stability of the amorphous phase of some GST compounds, i.e., the induced changes in local arrangement, was examined [125, 208–211]. Consistently, it was observed that ion irradiation of amorphous GST leads to enhanced crystallization kinetics, i.e., a reduced thermal stability, which is primarily caused by a reduction of homopolar bonds as was also discussed before for melt-quenched amorphous GST.

The incorporation of impurity atoms in GST compounds, i.e., impurity doping, by means of ion implantation was also addressed in literature [212–217]. However, ion implantation is far less considered for impurity doping compared to the wide range of doping during deposition of GST films. The incorporation of N, O, F via ion implantation was discussed by Privitera *et al.* revealing enhanced thermal stability of the amorphous phase of GST for N and O, while an increase in crystallization kinetics was observed for F [212, 216]. Furthermore, ion beam induced Si and O recoil implantation was performed by Carria *et al.* via Ge^+ -ion irradiation through a SiO_2 capping layer [217]. By this means, they observed even more pronounced doping effects compared to traditional ion implantation caused by circumventing the ion beam induced defect formation.

3. Experimental methods

This chapter gives an overview on the experimental methods used within this thesis. Further, important experimental details are specified. If not stated in particular, the measurements were performed at the *Institute of Solid State Physics* of the *Friedrich Schiller University Jena*.

3.1. Deposition methods

Magnetron sputtering All $\text{Ge}_2\text{Sb}_2\text{Te}_5$ (from this point on denoted as GST for simplicity) thin films were deposited on various substrates within this thesis using direct current (DC) magnetron sputtering at room temperature. By applying a distinct voltage $V_{DC} = (300 \pm 10)$ V between a stoichiometric $\text{Ge}_2\text{Sb}_2\text{Te}_5$ target and the grounded sample holder in an argon atmosphere with partial pressure $p_{Ar} = (5 \pm 2) \times 10^{-3}$ mbar, Ar particles become ionized and are accelerated towards the cathode knocking out (sputtering) target elements, which are deposited onto the substrate. The Ar pressure was set below 1×10^{-2} mbar to ensure high GST film quality [218]. A relatively low GST deposition rate of approximately 25 nm/min was obtained by setting the ion current to $I_{DC} = (40 \pm 5)$ mA. Typically, capping layers are deposited on top of GST for GST based device fabrication to prevent the films from oxidization and thus degradation. No capping layers were used in this thesis; thus, all experiments had to be carried out carefully to minimize degradation. Furthermore, gold coated Si substrates were also fabricated by DC magnetron sputtering with an additional titanium adhesion layer between Au and Si prior to the GST deposition. These substrates were fabricated by Dr. Frank Schmidl at the *Friedrich Schiller University Jena*. The thickness of the Au layer ($d_{Au} \approx 100$ nm) was designed in order to achieve bulk-like optical properties of the stack (see appendix A.1).

3.2. Characterization methods

3.2.1. Structural characterization

Energy dispersive X-ray spectroscopy (EDX) was used for qualitative and quantitative elemental analysis by detecting fluorescent X-rays that are created by impinging energetic electrons of an SEM. EDX measurements were carried out at the *FEI Helios*

NanoLab 600i using a *Oxford Instruments X-Max^N* silicon drift detector with a typical detection limit and elemental uncertainty of approximately 1 at.%. Quantitative analysis can be obtained by fitting the characteristic X-rays and the bremsstrahlung background with an additional XPP (extended Pouchou/Pichoir [219]) correction, which was accomplished by using the software package *AZtec* from *Oxford Instruments*. More details about EDX can be found in reference [220].

X-ray diffraction (XRD) is a non-destructive method to examine the structural properties of materials on the atomic/molecular scale. All XRD measurements presented in this work were carried out at a *Bruker D8 Discovery X-ray diffractometer* at the *University of Wisconsin-Madison*. Here, an X-ray beam that is created by a *Cu-K α micro X-ray source* is guided towards a sample while the scattered intensity is collected via a *Vantec 500 area detector* in $\theta - 2\theta$ mode (2θ corresponds to the angle between incoming and outgoing beam). Structural information of the sample arise from constructive interference of X-rays scattered at crystal planes due to the satisfaction of Bragg's law. The 2D area detector was positioned at three different outgoing angles, which limits the events that satisfy Bragg's law. In this common setup for powder analysis, the intensity along 2θ is integrated over a circular sector. By fitting all reflections, its position can be precisely determined. The scattering angle 2θ correlates to an adjacent plane distance d by Bragg's equation:

$$n\lambda = 2d \sin(\theta) , \quad (3.1)$$

with the X-ray wavelength λ (for Cu K α : $\lambda = 1.54059 \text{ \AA}$) and n being an integer value. The resulting plane distances can be used to calculate the lattice constants for a cubic cell via the miller indices (h , k , and l):

$$\frac{1}{d_{hkl}^2} = \frac{h^2 + k^2 + l^2}{a_{cub}^2} . \quad (3.2)$$

Similarly, the lattice constants for a hexagonal structure follow:

$$\frac{1}{d_{hkl}^2} = \frac{4h^2 + hk + k^2}{3a^2} + \frac{l^2}{c^2} . \quad (3.3)$$

Further, polycrystalline materials with small grain sizes are comparable to the powder counterpart and can thus be sufficiently examined with this experimental setup. However, it is not suitable for single crystalline materials as some crystal planes might not be detected. More details about XRD techniques can be found in references [221, 222].

3.2.2. Optical characterization

The reflectance of a sample can be measured in a wide spectral range with various optical spectroscopy techniques. However, they mostly require careful reference measurements to achieve reasonable quantitative results. This was accomplished by measuring bare silicon wafers and calculating its reflectance via Fresnel coefficients (compare section 3.5) using literature data of the refractive index from references [223, 224]. Corrected reflectance spectra are thus calculated via:

$$R_{\text{sample}}^{\text{corrected}} = R_{\text{sample}}^{\text{measurement}} \times \frac{R_{\text{silicon}}^{\text{calculation}}}{R_{\text{silicon}}^{\text{measurement}}}, \quad (3.4)$$

which cancels out all systematic errors occurring in the measurement. Silicon is chosen due to its well-known optical properties and low sample-to-sample variations.

UV-VIS-NIR spectroscopy was carried out with a *Varian Cary 5000 UV-Vis-NIR spectrometer* that is capable of measuring from the ultra-violet (UV) to near infrared (NIR) spectral range ("Vis" corresponds to visible). The spectrometer has the ability to measure between 250 nm and 2500 nm and can be either used in transmission or reflection mode. Here, light from a broad band source is monochromatically filtered and guided to the sample surface at near-normal incidence while the intensity of reflected light is measured via a photodetector. Reference [225] contains more details about the UV-VIS-NIR spectroscopy technique.

Fourier transform infrared spectroscopy (FTIR) measurements were performed on two different setups depending on the samples' footprint. While measurements on large-area samples were carried out via a *Varian 640-IR spectrometer* in the mid infrared (between 2 μm and 25 μm), small-area measurements require a small aperture to detect the reflectivity in micron sized areas. This was achieved by using a *Hyperion 2000 microscope* attached to a *Bruker Vertex 80V FTIR spectrometer* located at the *Institute of Applied Physics of the Friedrich Schiller University Jena*. Here, the measurements were carried out primarily in the near infrared spectral range using an InGaAs detector (between 850 nm and 1850 nm). Both systems rely on detecting light that is guided through a Michelson interferometer and spectral information arise from a Fourier transform of the FTIR interferogram. For more information on the various FTIR setups see reference [226].

Temperature-resolved reflectance (TRR) measurements were carried out by monitoring any changes to the reflectance of a sample during heating or cooling using a

3. Experimental methods

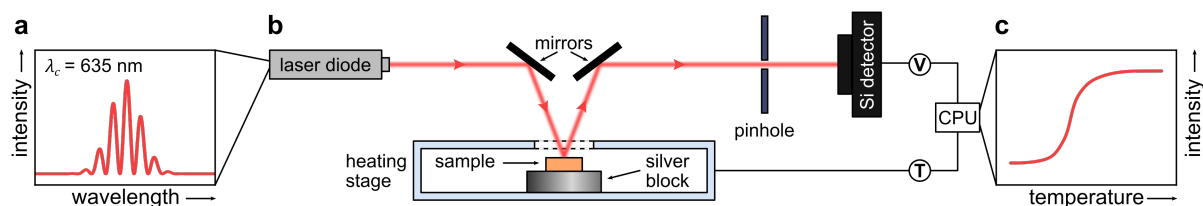


Figure 3.1.: (a) Illustrative multi-mode laser diode emission spectrum with a center wavelength $\lambda_c = 635$ nm. (b) Schematic of the experimental setup used for temperature resolved reflectivity measurements. (c) Symbolic TRR curve.

Linkam THMS 600 high temperature stage. This was enabled by a custom-built experimental setup, which was realized within this thesis and is depicted in figure 3.1. The heating stage allows to precisely (uncertainty ~ 0.01 °C) set a temperature in the range of -196 °C to 600 °C with a maximum heating rate of 150 °C. A mirror directs the laser beam of a collimated red laser diode with a multi-mode emission spectrum (center wavelength $\lambda_c = 635$ nm, spectral width $\Delta\lambda \approx 2$ nm, compare figure 3.1a) towards the sample, which is placed on the heating element (silver block) inside the chamber of the heating stage (see figure 3.1b). The laser beam is reflected from the sample and then guided through a pin hole towards a biased silicon detector. The pin hole is used to block any scattered or multiple reflected light of the stage window. Note that the laser power is only 1.2 mW and the spot size is 2.9 mm leading to an excitation power density of 0.18 mW/mm², which is sufficient to detect small intensity variations without significant thermal heating of the sample. Direct measurements of the surface temperature via a *PT1000* thermocouple revealed a discrepancy between surface temperature and the temperature of the heating element of only ± 1 K even for the maximal heating rate. Thus, reading out the value of the heating stage is sufficient to correlate reflectance changes to the sample temperature. The simultaneous measurement of the light intensity by the detector and the sample temperature thus allows monitoring reflectance changes upon heating or cooling of reflective samples (see figure 3.1c), which is especially beneficial for investigating the transition kinetics of either phase-change or phase-transition materials.

3.3. Imaging methods

3.3.1. Electron microscopy

Scanning electron microscopy (SEM) utilizes a focused electron beam to scan across a sample surface. Imaging with nanometer-resolution is achieved by spatially detecting primary or secondary electrons that are emitted through electron scattering. The tightly

focused electron beam provides lateral resolutions of about 2 nm. SEM measurements were carried out using the electron beam of the dual beam system *FEI Helios NanoLab 600i*. More information are provided by reference [227].

Transmission electron microscopy (TEM) uses a stationary parallel electron beam of several hundred keV while detecting the transmitted electrons directly through a ~ 100 nm thin specimen. A cross-sectional lamella was prepared using the focused ion beam system (*FEI Helios NanoLab 600i*) and subsequently investigated via a *JEOL Jem-3010* system at the *Otto Schott Institute of Materials Research (Friedrich Schiller University Jena)*. For more details about TEM see references [227, 228].

3.3.2. Scanning probe microscopy

Atomic force microscopy (AFM) allows for investigating the topography of a sample surface by approaching and scanning a sharp tip of a cantilever. A laser beam detects any cantilever deflections that occur due to close-range attractive forces between the sample and the tip. Topography maps were measured in two separate setups: a *neaSNOM* from *Neaspec GmbH* and a *VistaScope* from *Molecular Vista* both located at *Harvard University*. More details about AFM are presented in reference [229].

Scattering-type scanning near-field optical microscopy (s-SNOM) is an optical nano-imaging technique that provides information of the local optical polarizability of a probed sample surface with spatial resolution below 20 nm. A far-field photodetector detects laser light that is scattered at the tip-sample region according to the local electric field. Thus, scanning the tip over the sample allows for detecting differences in the local dielectric function of the sample surface. A tunable mid-infrared laser (quantum cascade laser) was used at a wavelength of 6.993 μm in combination with the *neaSNOM* for s-SNOM investigations, which also allows for AFM topography measurements. Only the nonlinear contributions to the scattered field were accounted in order to decouple the near- and far-field response [230]. This phase-sensitive detection is crucial for the suppression of the far-field background, while the signal mainly contains the near-field contribution. A detailed review of the s-SNOM method can be found in references [229, 231].

Photo-induced force microscopy (PiFM) was performed using a *VistaScope* System. Here, a green laser (532 nm) was focused at the AFM tip-sample region inducing a dipole-dipole image force generated by the field-sample interaction. As this light-induced force is measured completely mechanically, no far-field detection/suppression

is needed. Modulating the illuminating laser at the sum frequency of the first and second eigenmode of the cantilever allows for demodulating the electric signal of a quadrant photodiode. While demodulation at the second eigenmode yields AFM topography information, the PiFM signal is extracted by demodulating at the first eigenmode. More information about PiFM and some experimental results can be found in references [232–234].

3.4. Modification methods

3.4.1. Ion irradiation

Ion irradiation techniques allow for a variety of experiments by accelerating energetic ions towards a sample in order to examine or modify its physical properties. In this work ion beams were used, first, to intentionally create lattice defects inside crystalline GST films and, second, to implant various doping elements into amorphous GST films.

Large-area homogeneous ion irradiation was performed at the single-ended ion accelerator *ROMEO* with various ion energies and beam fluxes ranging from 30 to 200 keV and 10^{10} to 10^{13} $\text{cm}^{-2}\text{s}^{-1}$, respectively, depending on the specific experiment. More information about ion beam techniques can be found in references [70, 235].

Spatially selective ion irradiation of GST in confined regions was conducted via a focused ion beam (FIB). The dual beam system *FEI Helios NanoLab 600i* that was also used for SEM and EDX measurements provides a tightly focused (~ 5 nm) ion beam that was used to irradiate nanometer scaled regions inside GST thin films with various ion fluences while the flux was kept as low as possible ($\lesssim 1 \times 10^{14}$ $\text{cm}^{-2}\text{s}^{-1}$). Additionally, micrometer sized areas ($200 \mu\text{m} \times 200 \mu\text{m}$) were homogeneously irradiated to compare the FIB irradiation to experiments performed using the implanter *ROMEO* where large areas were irradiated. However, the FIB is restricted to gallium ions and a maximum energy of 30 keV. More information of FIB systems are provided by reference [237].

Spatially selective impurity doping of various elements inside GST films was achieved, in contrast to direct patterning using a FIB, by covering with suitable masking together with large-area homogeneous ion implantation. Common photolithography was conducted using a *AZ 5214 E* photoresist that was deposited much thicker than the penetration depth of the ions protecting the sample beneath. A simple mask was fabricated comprising squares with sizes ranging from $500 \mu\text{m}$ to $800 \mu\text{m}$ within a cell with a period of $1000 \mu\text{m}$ (for mask design see appendix A.1). The mask was removed

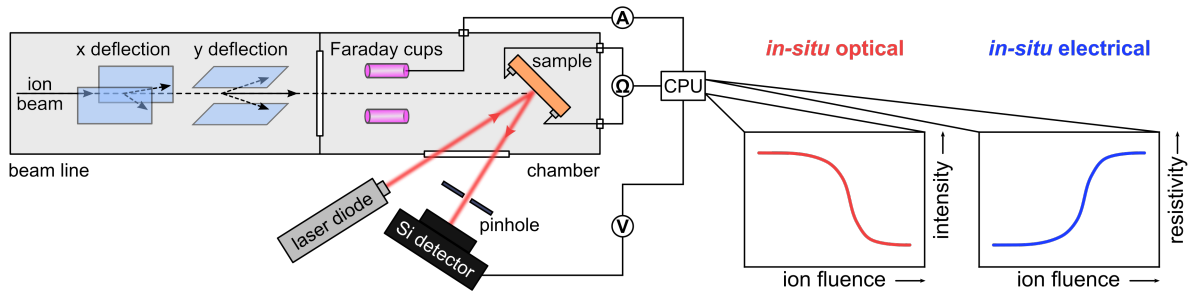


Figure 3.2.: Schematic of the experimental setup used for *in-situ* optical/electrical measurements during ion irradiation with respective symbolic curves.

subsequent to ion implantation using acetone in an ultrasonic bath for several minutes with additional rinsing with isopropanol and distilled water.

3.4.2. In-situ optical/electrical measurements during ion irradiation

For the purpose of instantly investigating changes to the physical properties of ion beam induced disorder in GST films, an experimental setup was realized within this thesis that allows to simultaneously monitor changes in the reflectivity and/or resistivity of the sample during ion bombardment. This setup is schematically depicted in figure 3.2. Optical measurements were conducted similar to the TRR measurements (compare section 3.2.2) with the same red laser diode ($\lambda_c = 635 \text{ nm}$). The incoming and outgoing laser beams are guided through a window (near-normal incidence) while the sample is tilted to 45° with respect to the ion beam inside the irradiation vacuum chamber. In this way, changes to the reflectivity of the sample upon ion irradiation can be directly observed by detecting the light intensity reflected by the sample via a Si detector. Simultaneously, it is also possible to monitor changes to the resistivity by contacting the sample via conductive lacquer to a *Keithley 2000 multimeter*. Note that no predefined contacts were used; thus, absolute resistance values cannot be compared due to different contact geometries between several samples. For *in-situ* experiments, the beam current was measured via Faraday cups with a defined area in order to calculate the ion fluence. A more detailed description of *in-situ* electrical measurements can be found in reference [236].

3.5. Simulations and numerical methods

Finite-difference time-domain (FDTD) simulations rely on the numerical solving of Maxwell's equations of the electromagnetic field distribution of light propagation through media in discrete spatial and temporal steps. The advantage of time-domain simulations is that a broad frequency band can be solved within a single simulation. The calculation of the reflectance of diverse optical devices was performed by using the *Lumerical FDTD* software package. More details on FDTD simulations can be found in reference [238].

Fresnel equations and transfer matrix method Light propagation through single and multilayer thin films can be described by using the Fresnel equations. Calculating these equations for a single interface between two distinct media results into the intensity of light that is reflected or transmitted. Thus, the reflection coefficient r and the transmission coefficient t can be written for s-polarization (of the electric field) as:

$$r_s = \frac{\tilde{n}_1 \cos(\theta_1) - \tilde{n}_2 \cos(\theta_2)}{\tilde{n}_1 \cos(\theta_1) + \tilde{n}_2 \cos(\theta_2)} , \quad (3.5)$$

$$t_s = \frac{2\tilde{n}_1 \cos(\theta_1)}{\tilde{n}_1 \cos(\theta_1) + \tilde{n}_2 \cos(\theta_2)} , \quad (3.6)$$

and for p-polarization as:

$$r_p = \frac{\tilde{n}_2 \cos(\theta_1) - \tilde{n}_1 \cos(\theta_2)}{\tilde{n}_2 \cos(\theta_1) + \tilde{n}_1 \cos(\theta_2)} , \quad (3.7)$$

$$t_p = \frac{2\tilde{n}_1 \cos(\theta_1)}{\tilde{n}_2 \cos(\theta_1) + \tilde{n}_1 \cos(\theta_2)} . \quad (3.8)$$

Here, θ_1 and θ_2 correspond to the angle of incidence and the angle of the transmitted wave, respectively. For a single interface, the reflectance R and transmittance T can be simply calculated via

$$R = |r|^2 \text{ and } T = \frac{\tilde{n}_2 \cos(\theta_2)}{\tilde{n}_1 \cos(\theta_1)} |t|^2 , \quad (3.9)$$

while extending the model to multiple interfaces in an optical multi-layer stack requires a more complex method to solve the various occurring reflection and transmission coefficients. Within this thesis a *MATLAB* based code (adapted from reference [236]) that relies on the transfer matrix method was used. This method is widely used in optics to model the propagation of electromagnetic light waves through a stratified medium. Taking into account Fresnel and Maxwell's equations, a simple 2x2 matrix can be used to describe the electric field within a single layer. The description of multi-layers is then the product of each layer's matrix and can be solved while also considering internal reflections and interference of coherent light waves.

4. Intrinsic physical properties of GST thin films

This chapter presents the intrinsic physical properties of as-deposited and thermal annealed GST thin films, which were deposited on various substrates via magnetron sputtering within this thesis. X-ray diffraction measurements were carried out by Chenghao Wan at the University of Wisconsin-Madison. Annealing experiments were conducted together with Konstantin Ruffert (see his bachelor thesis [239]). Optical measurements of GST thin films were performed in collaboration with Axel Printschler (see his bachelor thesis [66]). Optical constants presented in this chapter are published in reference [65].

4.1. Integral composition of as-deposited GST thin films

Thin GST films were deposited on various substrates, such as bare, thermally oxidized (with approximately 300 nm SiO₂), and gold coated single crystalline (100) silicon wafers, using magnetron sputtering at room temperature. Sputtering conditions of the GST deposition (compare section 3.1) were chosen with regard to achieve a relatively smooth layer with the desired material properties. Because of the strong dependence of the overall phase-change behavior, optical and electrical properties, and the crystalline structures on the stoichiometry of GST [218, 240], it is crucial to investigate the integral composition of the GST thin films. Thus, EDX was measured at several deposited GST films on Si and for comparison at the sputtering target, respectively (see figure 4.1a). In all spectra various characteristic X-ray peaks can be identified. The energy of the electrons in the primary beam should be at least a factor of two higher than the ionization energy of inner shell electrons (called overvoltage ratio [220]) to efficiently generate characteristic X-rays. Thus, only the L-lines of Sb and Te could be excited as the respective K-lines binding energies are in the range of roughly 30 keV, which is not possible to excite with the restricted 30 kV electron beam acceleration voltage of the SEM. However, the K-lines of Ge at around 10 keV are detected for a beam energy E_0 of 20 keV.

It is also important to account the excitation volume of the primary electrons for a quantitative analyses of thin films, which is strongly correlated to the acceleration energy (compare figure 4.1b). For a 10 keV beam energy the penetration depth x_e is roughly 1.3 μm , which was estimated by using the empirical formula: $x_e(\mu\text{m}) = 0.1E_0^{1.5}\rho^{-1}$

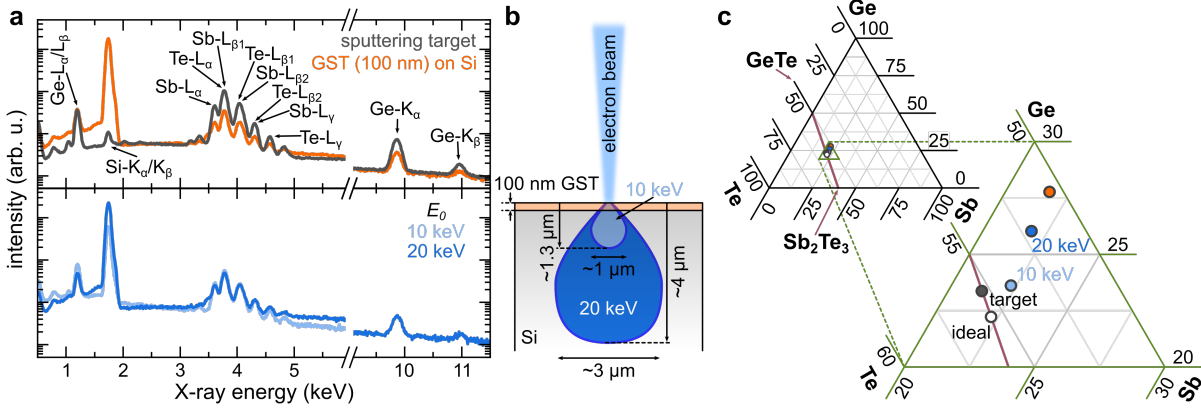


Figure 4.1.: (a) EDX spectra of a 100 nm GST thin film deposited on a silicon substrate (orange) compared to the GST sputtering target (gray) and a similar 100 nm GST film from a different batch, while the latter was excited with different beam energies E_0 (light and dark blue). (b) Schematic of the penetration depth of impinging electrons for the beam energies of (a), respectively, illustrates the strong contribution of the Si substrate peak to the spectra of the GST thin films. (c) Ternary phase diagram of a Ge, Sb, and Te mixture together with an enlargement on the area of interest depicts the extracted stoichiometries of the samples from (a). The white dot marks the ideal stoichiometry of $\text{Ge}_2\text{Sb}_2\text{Te}_5$, which is located on the pseudo-binary $\text{GeTe-Sb}_2\text{Te}_3$ line (red).

(and further the width $y_e(\mu\text{m}) = 0.077E_0^{1.5}\rho^{-1}$). As a result doubling the beam energy to 20 keV leads to three times higher penetration depth ($\sim 4 \mu\text{m}$) and thus the probed volume increases drastically. For an only $\sim 100 \text{ nm}$ film the respective volume ratio of specimen to substrate is small and should be considered when evaluating the EDX measurement.

By fitting the EDX spectra depicted in figure 4.1a, the compositions of these samples were extracted and are plotted in a ternary phase diagram (figure 4.1c). The composition of the stoichiometric target (gray) is close to the ideal composition of $\text{Ge}_2\text{Sb}_2\text{Te}_5$ (white) while the discrepancy is in the range of EDX uncertainty. The compositions of the $\sim 100 \text{ nm}$ GST films that were deposited in different batches show for 20 keV excitation energy (orange and dark blue) an increased Ge and decreased Te contribution while Sb is similar to the ideal or target stoichiometry. Small deviations can be attributed to sample-to-sample variations and the EDX uncertainty. Contrary, for the $E_0 = 10 \text{ keV}$ measurement (light blue) the extracted composition is in the uncertainty range of the ideal/target stoichiometry with only a slightly increased Ge concentration. This can be attributed to the higher specimen/substrate ratio for the smaller electron energy. As the XPP correction (compare section 3.2.1) is performed for bulk material, attenuation of X-rays is assumed leading to higher anticipated Ge, Sb, and Te intensities. If only the L-Lines were considered, this effect mainly cancels out by only using the ratios of these elemental contributions. However, for the 20 keV excitation, the Ge K-lines are additionally considered, and thus a higher Ge concentration is assumed

by the fit. This effect makes the lower excitation energy (10 keV) more reliable and it can be concluded that the GST thin film stoichiometry is similar to the intended $\text{Ge}_2\text{Sb}_2\text{Te}_5$ composition with probably a slightly increased Ge content. However, exact values cannot be concluded with this method.

4.2. Thermal annealing

As the GST deposition was performed at room temperature, presumably, the as-deposited GST thin films are in an amorphous state. Multiple possibilities to crystallize GST are available, which were discussed in section 2.2.2. However, the more classical approach is using thermal annealing of GST films by inducing heat to the system, which can be conducted with the temperature-resolved reflectance (TRR) setup (compare section 3.2.2). This allows additionally to monitor the change in reflectance of the GST thin films upon heating. The reflectance change of an approximately 100 nm GST film deposited on Si that was heated with a constant heating rate of 10 K/min in air is depicted in figure 4.2a. Two drastic increases can be observed at around 165 °C and 270 °C indicating two phase transitions from amorphous to rock-salt and from rock-salt to hexagonal, respectively. The first transition is linked to crystallization into the rock-salt phase (compare section 2.3). Repeated measurements at the same conditions with similar samples show the same critical temperature T_C for the first phase-change, which is defined by the maximal change rate indicated by a peak in the derivative of the reflectance change (see inset of figure 4.2a). However, the second transition arises from ordering the randomly distributed vacancies inside the rock-salt lattice that drives the insulator-to-metal transition and leads to highly ordered vacancy layers (van der Waals gaps [241], compare also section 2.3) in the hexagonal phase. More insights in the phase-change kinetics can be obtained by varying the heating rate of the TRR measurements, which is depicted in figure 4.2b. With increasing heating rate v the onset of crystallization shifts to higher temperatures. Differentiating the reflectance change in the transition regions can be used to identify critical temperatures T_C for each heating rate and phase-change, respectively, which is indicated by the peaks in figure 4.2e. Plotting of $\ln(v/T_C^2)$ as a function of inverse T_C , which was proposed by Kissinger (Kissinger plot in figure 4.2f [242, 243]), can be used to extract an activation energy E_A for crystallization by fitting a linear dependency. For the phase-change from amorphous to rock-salt E_A is roughly (2.7 ± 0.1) eV while $E_A \approx (1.9 \pm 0.2)$ eV for the rock-salt to hexagonal phase transition.

A similar examination can be accomplished by measuring the reflectance change at a constant elevated temperature that is in the vicinity of the phase-change as a function of time. Figure 4.2c shows such an experiment for temperatures ranging from $T_0 = 150$ °C

4. Intrinsic physical properties of GST thin films

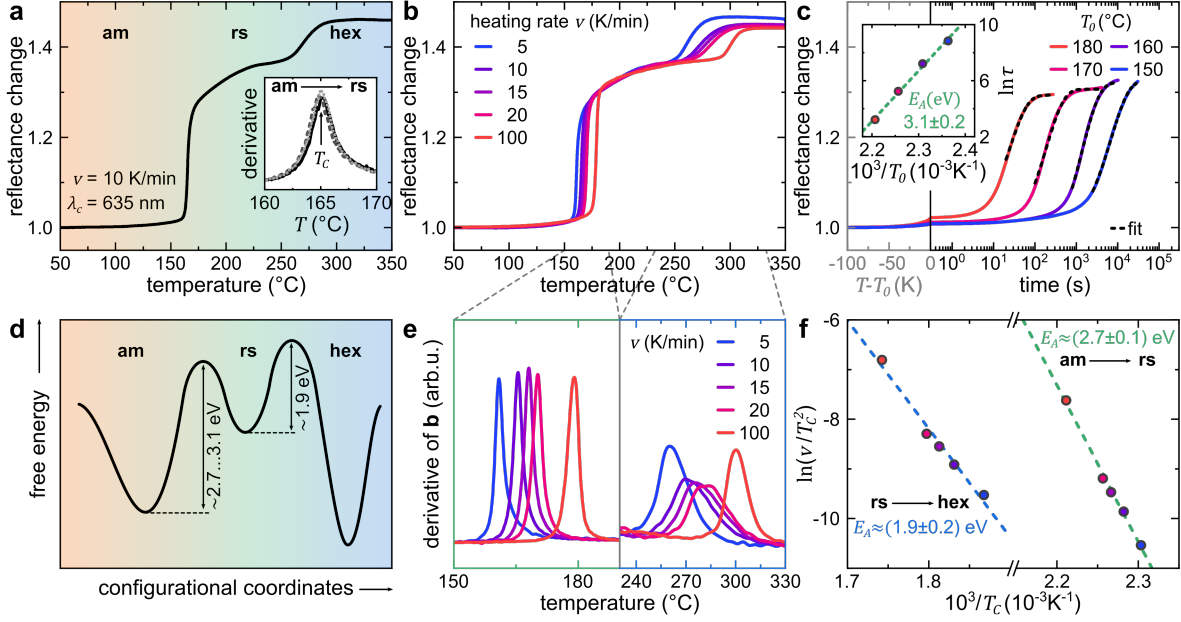


Figure 4.2.: (a) Reflectance change $R(T, t)/R_0$ of an approximately 100 nm GST thin film during heating (heating rate $v = 10$ K/min) at a wavelength of $\lambda_c = 635$ nm. The inset shows the derivative of $R(T)/R_0$ around the first phase-change from amorphous (am) to rock-salt structure (rs) for 3 samples to confirm reproducibility. (b,c) Reflectance change of GST thin films (~ 100 nm) as a function of (b) temperature with various heating rates and (c) annealing time at different constant temperatures (T_0). For the latter elevated temperatures T_0 were reached using a 100 K/min heating rate depicted in the gray left scale ($T - T_0$). Characteristic decay times $\tau(T)$ are extracted of exponential fits (black dashed lines) and depicted as an Arrhenius plot in the inset of (c). (d) Schematic free energy diagram as a function of representative configurational coordinates for GST thin films with phase-change barriers between amorphous to rock-salt and rock-salt to hexagonal (hex) structure. (e) Derivative of the reflectance change of b enlarged in the regions of phase changes, respectively. (f) Kissinger plot of the critical temperatures (T_c) obtained from (e).

to 180 °C and times up to 10^4 s. Note that prior to reaching $T_0 = 180$ °C there is already a significant increase of the reflectivity (compare figure 4.2c, gray left scale) due to incipient crystallization. The shape of the ongoing reflectance change due to the phase-change (amorphous to rock-salt) can be described with the JMAK¹ equation [244]. This is not trivial, but arises from a linear correlation between the reflectance of a GST thin film and its crystalline fraction (see appendix A.1). However, characteristic decay times $\tau(T)$ can be extracted by fitting an exponential decay to the tail of the reflectance change and, furthermore, an Arrhenius plot of $\ln(\tau)$ versus inverse temperature again allows for predicting activation energies E_A (see inset of figure 4.2c). With this method an E_A of (3.1 ± 0.2) eV was estimated for the amorphous to rock-salt transition, which is similar but slightly different to the previous described results. This might be caused by the different approximations in both models, respectively. Presumably, the activation

¹Johnson-Mehl-Avrami-Kolmogorov

energy for the phase-change from amorphous to rock-salt may be approximately in the range of 2.7 eV to 3.1 eV. These values are in good agreement with previous calorimetry experiments predicting E_A [242, 245].

This examination give hints to crystallization or phase-change barriers of GST, which are schematically depicted in figure 4.2d in a free energy diagram. The lower activation energy for the rock-salt to hexagonal ($E_A \approx 1.9$ eV) transition compared to the crystallization barrier from amorphous to rock-salt is in accordance with a meta-stable rock-salt phase [246].

4.3. Structural properties

In the previous section it was demonstrated that heating as-deposited amorphous GST thin films above ~ 200 °C or ~ 300 °C resulted in phase transformations presumably into the rock-salt or hexagonal phase, respectively. Furthermore, a structural characterization of these phases is mandatory to confirm their crystal structures and thus XRD measurements were carried out at differently annealed GST thin films on Si (GST thicknesses about 100 nm) as shown in figure 4.3a.

Several peaks appear in the XRD pattern (green curve in figure 4.3a) for a GST film that was heated to ~ 250 °C (with a constant heating rate of 20 K/min) and immediately cooled down to room temperature. By comparing the peak positions with literature [126], it is obvious that the amorphous thin film was crystallized to a polycrystalline film with the rock-salt structure. Note that due to the experimental setup (compare section 3.2.1) no peaks of the single crystalline (100) Si substrate were detected. Further heating of the GST film up to ~ 350 °C (same heating rate as before) leads to the occurrence of new peaks indicating the hexagonal crystal structure (blue curve in figure 4.3a). A strong indication for the hexagonal phase is the h(106) reflection at about 40° (see inset in figure 4.3a) where no overlaying rock-salt peaks should be present. Indexing of all reflections according to reference [131] reveals that additional peaks are still present, which cannot be explained with hexagonal GST.

A closer look at the region around 29° in figure 4.3b shows that in the measurement of the hexagonal sample the r(200) reflection ($2\theta \approx 29.6^\circ$) is still visible while the h(013) peak ($2\theta \approx 29.0^\circ$) is shifted by $\sim 0.6^\circ$ with respect to the r(200) reflection. These values were extracted out of multiple Gaussian peak fits to the diffraction data. Thus, a minor portion of rock-salt phase remains in the GST film for the sample that was heated to ~ 350 °C. Possibly higher temperatures or holding the sample temperature at ~ 350 °C for a significant period of time might reduce or even vanish the rock-salt portion in the film. However, to avoid oxidation/overall degradation of the GST film due to the missing capping layer higher temperatures or longer annealing times were

4. Intrinsic physical properties of GST thin films

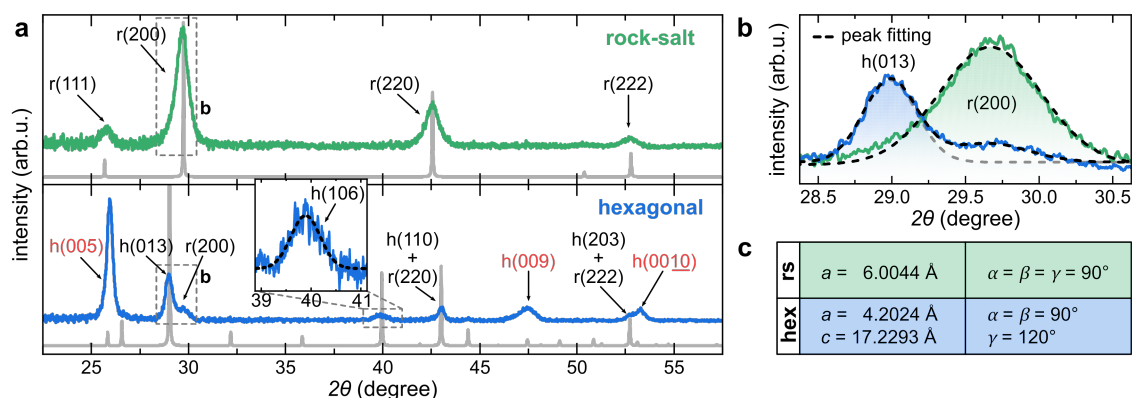


Figure 4.3.: (a) XRD patterns obtained in $\theta - 2\theta$ mode of approximately 100 nm GST thin films in the rock-salt and hexagonal phase, respectively. Reflection peaks of the crystalline phases are identified using references [126, 131]. Gray lines display the calculated powder diffraction patterns of the rock-salt and hexagonal structure, respectively, using fitted lattice constants. (b) Magnification of characteristic h(013)/r(200) reflections, that can be used to differentiate between rock-salt and hexagonal structure. Dashed lines represent multiple Gaussian fits to the data. (c) Respective lattice constants that are calculated via the fitted peak positions for both phases.

avoided. Furthermore, the detailed scan also shows broader peaks for the rock-salt phase revealing smaller grain sizes in rock-salt compared to hexagonal GST thin films. Moreover, this is further corroborated by estimating the average grain size using the Scherrer equation [247], which results in about 18 nm and 14 nm for the hexagonal and rock-salt phase, respectively (with errors of ~ 4 nm for both phases).

Furthermore, the lattice constants were calculated for both phases by cross-fitting the peak positions (compare section 3.2.1) and are given in the table in figure 4.3c, while the error is on the order of 0.01 \AA . They are in good agreement with previous works [126, 131] (compare also section 2.3.1). The lattice constants were additionally used to calculate powder diffraction patterns for both phases, respectively (gray lines in figure 4.3a).

Comparing the intensity of the calculated powder patterns with the experimentally obtained thin film patterns reveals preferential orientation of a large portion of grains in hexagonal GST films. The h(005), h(009), and h(0010) reflections (marked red in figure 4.3a) of the hexagonal thin film have a higher contribution than expected from the calculated powder counterpart, where the h(013) should have the highest intensity. Thus, here, most grains likely are preferentially orientated along the c-axis of the hexagonal structure. Preferential orientation was not observed for the rock-salt phase.

4.4. Optical properties

A combination of UV-VIS-NIR and FTIR spectroscopy in reflection mode was performed that allows for optical measurements ranging from UV to mid infrared. GST thin films with three different thicknesses, that were approximately $d = 25$ nm, 50 nm, and 100 nm thick, were deposited and annealed on thermally oxidized silicon. Annealing conditions were the same as for the samples used in the previous section. The obtained reflectance spectra of amorphous, rock-salt, and hexagonal GST films on SiO₂/Si are given in figure 4.4a-c. Stacking of thin GST films on top of SiO₂/Si results in a strong reflectance modulation caused by thin film interference. As an approximately 300 nm SiO₂ layer on top of Si already shows a strong modulation due to transparent silica (see Appendix A.1), an additional thin GST layer leads to even more interfaces that result in strong multilayer interference. These distinct interference fringes occur for all phases, respectively, mainly in the infrared region while only the thinnest films (d_1) show further modulations in the visible due to the small film thickness compared to the penetration depth of light in this spectral range. Features at roughly 9 μ m and 22 μ m cannot be assigned to thin film interference, but arise from phonon resonances of SiO₂ [248] and are detectable in all spectra. However, in the measurements of hexagonal GST (see figure 4.4c) this feature is less pronounced indicating higher losses of hexagonal GST in the infrared compared to the other phases, respectively. The general reflectance especially in the visible range, where nearly no modulation occurs, increases after the phase transformations to the rock-salt and hexagonal phases, respectively, hinting an overall higher refractive index of crystalline compared to amorphous GST.

In order to extract the intrinsic optical constants, the reflectance spectra were numerically fitted using a Tauc-Lorentz (TL) dispersion model for the complex permittivity $\tilde{\epsilon}(\omega)$ of GST with an additional Drude term, which is necessary to account for free carrier absorption in the crystalline phases:

$$\tilde{\epsilon}(\omega) = \epsilon_{\infty} + \tilde{\epsilon}_{\text{TL}}(\omega) + \tilde{\epsilon}_{\text{Drude}}(\omega), \quad (4.1)$$

where ϵ_{∞} is the high frequency permittivity (for details see Appendix A.3). The Drude term $\tilde{\epsilon}_{\text{Drude}}(\omega)$ can be neglected for amorphous GST in the considered wavelength range.

The reflectance was calculated out of given optical constants of Si [223, 224] and SiO₂ [248, 249] and using the Tauc-Lorentz (and Drude) model for GST by applying the transfer matrix method, which is based on the Fresnel equations and already considers interference effects of single and multilayer thin films (compare 3.5). The SiO₂/Si substrate was chosen due to the fact that the observed strong modulations of the reflectance restrict some degrees of freedom benefiting the fitting routine. Further, to get

4. Intrinsic physical properties of GST thin films

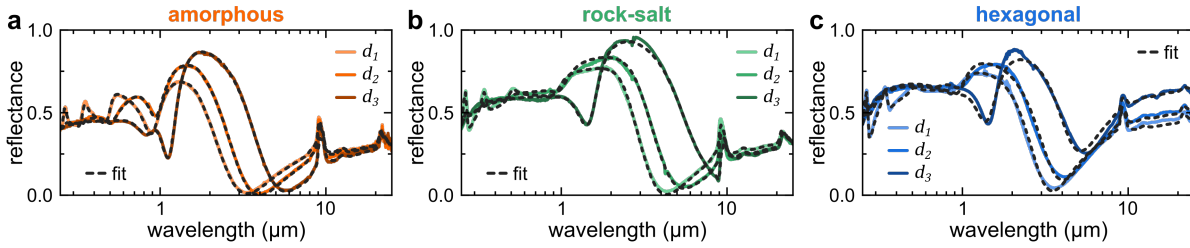


Figure 4.4: (a-c) Measured reflectance spectra of GST thin films with various thicknesses of roughly 25 nm, 50 nm, and 100 nm (d_1 , d_2 , and d_3 , respectively) on SiO₂/Si with GST in the (a) amorphous, (b) rock-salt, and (c) hexagonal phase, respectively. All measurements were fitted (dashed lines) using a Tauc-Lorentz dispersion model with an additional Drude model contribution to the permittivity for the crystalline phases.

quantitatively reasonable results, the SiO₂ thickness (333 nm) was determined by fitting measured reflectance spectra of the SiO₂/Si substrate also using Fresnel-equations (see appendix A.1). To gain statistical certainty and to account for sample-to-sample variations, three samples for each GST film thickness and phase, were fitted simultaneously (only one representative measured and fitted spectrum are given in figure 4.4a-c, respectively). Additionally, the film thickness was not assumed to be constant but was also fitted within the routine. Thus, the given values d_1 , d_2 , and d_3 are only the predicted film thicknesses of each batch. Note that an eventual surface roughness layer was neglected in the fit.

The extracted real ϵ_1 and imaginary part ϵ_2 of the permittivity of all GST phases are given in figure 4.5a. Solid lines represent mean values that correspond to the average of the fits to all film thicknesses (in total 9 spectra) for each GST phase individually, while shaded areas depict the standard deviations. It is evident that there is a distinct difference of the optical constants between all GST phases over the whole given spectral range. Both crystalline phases exhibit a Drude contribution in the infrared arising from free charge carriers. Thus, hexagonal GST has losses ($\epsilon_2 > 0$) all over the presented wavelength range. However, there is only a weak Drude contribution for rock-salt GST in the mid infrared. Note that the standard deviations of the permittivity of hexagonal GST are relatively high in the infrared due to a sensitive Drude part, which strongly depends on the preparation conditions [240]. Thus, for further experiments the samples were prepared carefully under similar conditions to ensure comparability.

Amorphous GST has a ϵ_2 that reaches zero for wavelengths larger than approximately 2 μm , which is also depicted in figure 4.5b as a function of photon energy that is used to illustrate the Tauc-Lorentz model parameters. Further, the optical energy gap E_g of amorphous GST can be identified in this plot which is 0.69 eV. The average of the fitted parameters of the Tauc-Lorentz and Drude model are given in the table in figure 4.5c for all phases together with standard deviations given in brackets. These values

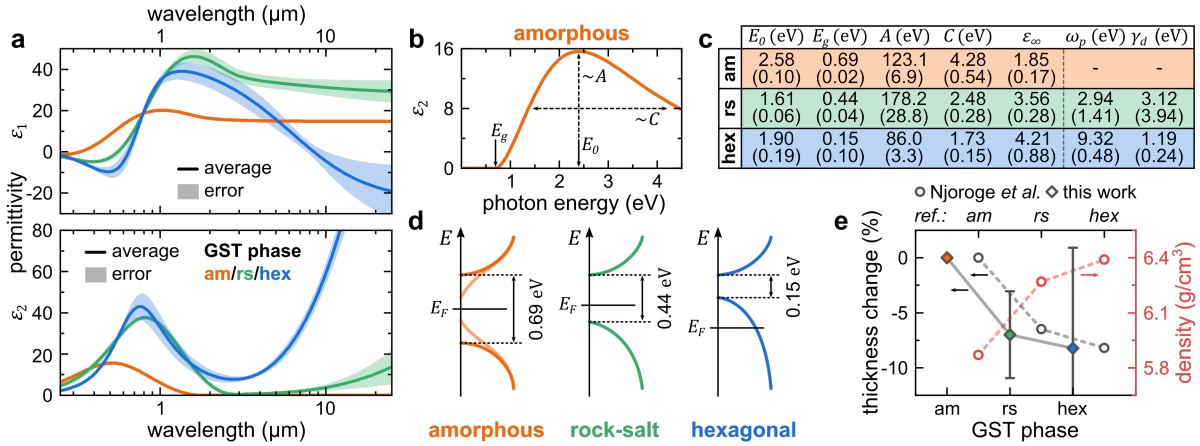


Figure 4.5.: (a) Real ε_1 and imaginary part ε_2 of the permittivity extracted out of the fits to the reflectance spectra for all phases, respectively. Solid lines correspond to average values of amorphous (orange), rock-salt (green) and hexagonal (blue) phases while shaded areas display the respective standard deviations. (b) Imaginary part of the permittivity ε_2 of amorphous GST to illustrate Tauc-Lorentz parameters. (c) Mean Tauc-Lorentz and Drude model parameters for all phases (standard deviations given in brackets), respectively. (d) Schematic representation of the density of states depicting the optical Tauc gaps for all phases, respectively (adapted from Kato *et al.* [140]). (e) Relative thickness change of GST films upon crystallization (additionally extracted from the fits) compares well to values given by reference [250] (reference values shifted for better visibility) and to the change in density (red axis).

are used for further optical simulations in this thesis and are in good agreement with literature data [107, 143, 167, 168].

Figure 4.5d schematically illustrates the density of states (DOS) of all GST phases with the obtained optical band gaps. Extended electronic states can be approximated with parabolic bands for all phases, which is accounted by the Tauc-Lorentz dispersion model. The optical Tauc gap of amorphous GST is 0.69 eV indicating semiconducting properties. However, electronic structures of amorphous semiconductors are not trivial compared to the crystalline counterpart [140]. Thus, the DOS of amorphous GST in figure 4.5d should be interpreted carefully. Between the parabolic valence and conduction bands there is an additional Urbach tail due to localized states in the band gap of disordered media [144, 145] (symbolized by light orange line in figure 4.5d). However, the Urbach tail is not accounted in the Tauc-Lorentz fit. Thus, the Tauc gap may refer to the energy difference between extended electronic states [140]. Using a Cody-Lorentz dispersion model would be more sufficient for more precise optical constants around the valence band edge. However, it results only in minor differences in ε_2 [167]. Further, the energy gap decreases upon crystallization to the rock-salt phase ($E_g = 0.44$ eV). It was reported that rock-salt GST is a p-type semiconductor with a Fermi level (E_F) close to the valence band that is a result of a high intrinsic vacancy concentration [140] (compare section 2.3). Vacancy ordering in the hexagonal phase

results in the formation of a defect band, which leads to a further decrease of the optical band gap and a Fermi level deep inside the valence band so that hexagonal GST can be regarded as a degenerate p-type semiconductor [140]. This is in good agreement with the obtained narrow band gap of $E_g = 0.15$ eV for hexagonal GST and explains its metal-like physical properties.

Furthermore, the density of GST changes upon crystallization, which was also observed in the extracted GST film thicknesses. In figure 4.5e the mean thickness change (normalized to the amorphous phase) upon crystallization is depicted. The film thickness decreases by roughly 6 % and 9 % for the rock-salt and hexagonal phase, respectively, which matches previous results from Njoroge *et al.* [250] (white dots in figure 4.5e) and is also in good agreement with the density differences of the GST phases (see figure 4.5e, red axis).

5. Tailoring disorder in GST thin films

Irradiations with energetic ions are commonly used for impurity doping of diverse materials to modify the structural and electronic properties. As ion irradiation causes displacements of lattice atoms via nuclear collisions, an inevitable amount of structural defects such as interstitials, vacancies, or complex defect clusters are formed during ion bombardment. Usually, these lattice defects have to be recovered by an appropriate thermal treatment that facilitates defect migration and recombination. Recently, it was demonstrated that the intentional creation of structural defects and lattice damage can be also utilized to modify and engineer the electronic structure of strongly correlated materials such as vanadium dioxide (defect engineering, [78]). Furthermore, various structural and electronic transitions can be triggered in GST by inducing disorder [59, 61, 251]. Moreover, using ion irradiation readily enables the ability to tailor the amount of lattice damage. Thus, this chapter investigates the effect of the intentional creation of lattice defects by means of homogeneous ion irradiation on the optical, electrical, and structural properties of GST thin films on various substrates. First, a combinatorial approach of optical and electrical measurements was performed (*in-situ*) during ion bombardment of initially crystalline GST thin films. Second, multiple GST films were irradiated with various ion fluences and subsequently (*ex-situ*) optically and structurally examined. Further, the results of both approaches – *in-situ* and *ex-situ* – are compared. Optical measurements of *ex-situ* irradiated GST films and thermal annealing of ion beam amorphized GST films were performed in collaboration with Robin Schock (see his master thesis [68]). Measurements on the thermal stability of intermediate GST states were carried out together with Axel Printschler (see his bachelor thesis [66]). X-ray diffraction measurements were performed by Chenghao Wan at the University of Wisconsin-Madison. The results on tailorable near-zero reflection presented in this chapter are published in reference [67].

5.1. Ion beam induced disorder – *in-situ* measurements

A combination of *in-situ* optical and electrical measurements were performed in order to investigate the effect of ion irradiation on the physical properties of initially crystalline (rock-salt and hexagonal) GST films. For this purpose, GST thin films with a thickness of approximately 100 nm on SiO₂/Si were irradiated with 180 keV Ar⁺-ions at room temperature while the samples' reflectivity and resistance were continuously monitored. The insulating SiO₂ barrier of the substrate is mandatory for electrical

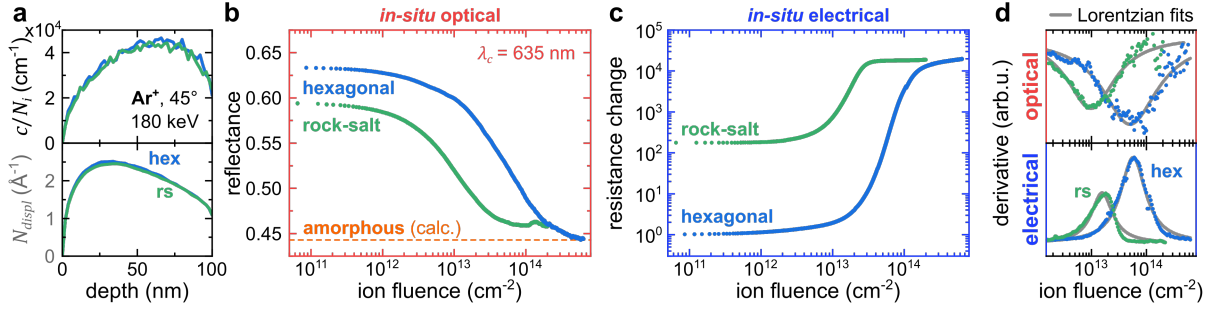


Figure 5.1.: Simultaneous *in-situ* optical/electrical measurements of approximately 100 nm GST films on SiO₂/Si initially in the hexagonal and rock-salt phase, respectively. **(a)** Ar concentration normalized to ion fluence c/N_i (top) and total displacements per incident ion N_{displ} (bottom) as a function of depth at 45° incidence angle as simulated with SRIM. **(b)** Reflectance at 635 nm of initially hexagonal and rock-salt GST films upon Ar⁺ irradiation at a constant flux of $2 \times 10^{11} \text{ cm}^{-2}\text{s}^{-1}$. Additionally, the dashed orange line corresponds to the calculated reflectance value of a comparable amorphous GST film. **(c)** Simultaneously obtained resistance change for both phases, respectively. **(d)** First derivatives of *in-situ* optical and electrical measurements for hexagonal and rock-salt GST films are fitted (on a logarithmic scale) using Lorentzian distribution functions, respectively.

measurements to avoid current flow through the substrate and beneath the contacts, where the GST film is not irradiated. Further, the usage of the noble gas Ar as ion species is advantageous, because Ar is not chemically incorporated into the GST matrix. This allows for mainly investigating the effect of induced lattice damage without any unintended impurity doping. The ion flux was set constant and sufficiently low at $2 \times 10^{11} \text{ cm}^{-2}\text{s}^{-1}$ to minimize thermal heating by the ion beam [252]. Further, the energy of the impinging ions was chosen in order to create a damage profile that is almost uniform across the film thickness by calculating the depth distribution of total displacements and penetration depth per incident ion using SRIM simulations [81], as shown in Figure 5.1a. This estimation was performed for both crystalline GST phases and shows only negligible differences.

The change in reflectance at $\lambda_c = 635$ nm of initially rock-salt and hexagonal GST films upon ion irradiation as a function of ion fluence is plotted in figure 5.1b. As the experimental setup detects only changes of the sample's reflectivity, absolute reflectance values were calculated for the intrinsic films using the optical constants that were determined in section 4.4. Furthermore, thin film interference should not affect the signal as the penetration depth of the used light is small compared to the GST film thickness. The reflectance of both, rock-salt and hexagonal, GST films decreases upon ion bombardment and saturates for ion fluences higher than $1 \times 10^{14} \text{ cm}^{-2}$ (rock-salt) or $5 \times 10^{14} \text{ cm}^{-2}$ (hexagonal). In saturation, the reflectance of both films is close to the expected value of amorphous (as-deposited) GST.

Simultaneous to the obtained reflectance change the resistance of the samples was monitored, which is displayed in figure 5.1c. Here, relative changes were compared instead of absolute values due to different contact geometries of each sample despite measuring absolute resistance values (see section 3.4.2). To account for the different intrinsic resistances of rock-salt and hexagonal GST films, the resistance change of the rock-salt sample was normalized to the high ion fluence side of the hexagonal sample as the resistance in the amorphous phase should be similar for both samples. Thus, the resulting resistance difference of intrinsic hexagonal and rock-salt GST is ~ 200 and in good agreement with reported values [100, 101]. Moreover, the resistance increases upon ion irradiation by 4 or 2 orders of magnitude and saturates for high ion fluences above $2 \times 10^{14} \text{ cm}^{-2}$ or $4 \times 10^{13} \text{ cm}^{-2}$ for the intrinsic hexagonal or rock-salt phase, respectively. These values are slightly lower than for the optical data, which indicates different relations between the optical and electrical properties and the amorphous fraction, thus the amount of induced disorder in the film. However, the phenomenological observation of the optical and electrical properties already hints that initially crystalline GST films can be amorphized by inducing lattice damage by means of ion irradiation as already reported by others [58–61, 251].

Further, the first derivative of *in-situ* optical and electrical data reveals a point of maximal change in both cases. Here, this point is assigned to a critical amount of induced lattice damage that ultimately leads to amorphization of the GST film (see figure 5.1d). It is evident that this critical ion fluence is significantly smaller for rock-salt ($\sim 1 \times 10^{13} \text{ cm}^{-2}$) than hexagonal ($\sim 5 \times 10^{13} \text{ cm}^{-2}$) GST, which can be seen in both optical and electrical measurements. This different behavior of the crystalline GST phases upon ion irradiation at room temperature, despite identical chemical composition, was recently demonstrated by Privitera *et al.* [59]. Directional effects like axial or planar channeling are negligible for polycrystalline films; therefore, the irradiation damage should be independent on the crystal structure of the irradiated media. Hence, discrepancies in the amorphization thresholds are likely linked to different thermal mobilities of ion beam induced defects in both phases.

5.2. Ion energy dependence of lattice defects

So far, only single energy irradiation were performed; however, in the next sections the ion energy is adjusted depending on the respective experiment requirements. Within this section, the influence of ion energy on the observations of the *in-situ* experiments is discussed. Thus, multiple GST films ($d \approx 100 \text{ nm}$) on SiO_2/Si and Si were irradiated with Ar^+ -ions at various energies. While *in-situ* optical measurements were performed during ion bombardment of GST films on Si, the electrical measurements required the

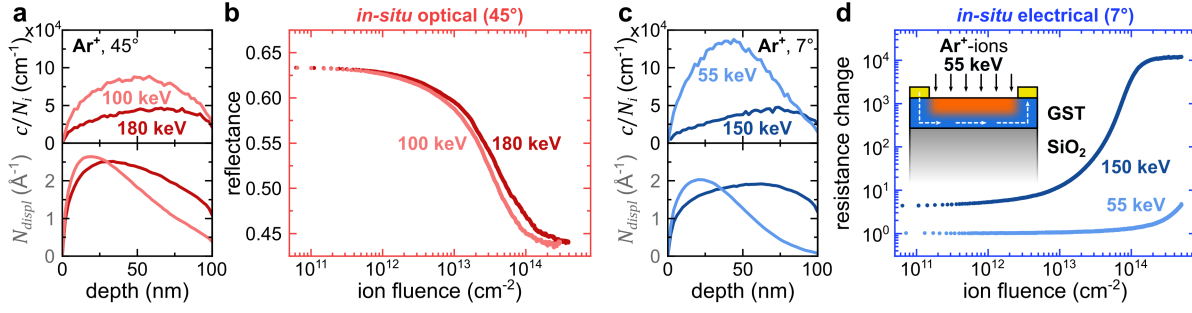


Figure 5.2.: (a) Ar concentration per ion fluence c/N_i (top) and total displacements per incident ion N_{displ} (bottom) for Ar⁺-ions into hexagonal GST with ion energies 100 keV and 180 keV and 45° incidence angle. (b) Reflectance at 635 nm of initially hexagonal GST films on Si upon Ar irradiation at a constant flux of $2 \times 10^{11} \text{ cm}^{-2} \text{ s}^{-1}$ for the ion energies and incidence angle of (a). (c) Ar concentration per ion fluence c/N_i (top) and total displacements per incident ion N_{displ} (bottom) as a function of depth for Ar⁺-ions into hexagonal GST with ion energies 55 keV and 150 keV and 7° incidence angle. (d) Resistance change of a GST film on SiO₂/Si at a constant flux of $2 \times 10^{11} \text{ cm}^{-2} \text{ s}^{-1}$, which was first irradiated with an Ar ion energy of 55 keV and further irradiated with 150 keV at an incidence angle of 7°.

SiO₂/Si substrate. The results from both measurement setups are depicted in figure 5.2. First, *in-situ* optical measurements were performed at 45° incidence angle for beam energies of 100 keV and 180 keV at GST thin films on Si. The latter energy was used before (compare figure 5.1) to ensure nearly uniform damage distribution across the entire film. Consequently, an inevitable amount of Ar⁺-ions reaches the substrate and possible interface mixing might influence the GST layer (see figure 5.2a). Reducing the beam energy to 100 keV and keeping the angle at 45° leads to a non-uniform damage profile while most Ar⁺-ions remain in the film and interface mixing can be neglected. The reflectance change upon ion irradiation for these energies is given in figure 5.2b. The reflectance decreases down to the expected amorphous value in both cases with only minor differences in the critical amount of induced lattice defects. This can be attributed to the different number of total displacements per ion for both energies (compare figure 5.2a). As the red laser light ($\lambda_c = 635 \text{ nm}$) only probes roughly the first 50 nm of the GST film (with the extinction coefficient being ~ 4 for both crystalline phases), the reflectance signal contains mainly information about the first half of the film. Thus, the slightly higher amount of displacements near the surface for the 100 keV irradiation compared to the higher beam energy of 180 keV explains the slightly smaller critical ion fluence for amorphization.

A similar examination was performed for *in-situ* electrical measurements on approximately 100 nm thick GST films on SiO₂/Si. As these measurements were not performed simultaneously to the *in-situ* optical examination, here, an incidence angle of 7° was chosen. As the depth distribution of damage caused by impinging ions is also determined by their angle of incidence, the beam energies were adjusted properly. Similar

damage profiles can be achieved by using 55 keV and 150 keV ions (see figure 5.2c). The resistance change of a GST film upon 55 keV ion irradiation is depicted in figure 5.2d. Even for comparable high ion fluences well above previously obtained amorphization thresholds the resistance only slightly increases. On the other hand, subsequent irradiation with 150 keV ions of the same sample leads to a drastic increase in resistance to the expected change caused by amorphization. As the induced lattice damage at the interface of the GST and SiO₂ films is negligible for a beam energy of 55 keV, a non-damaged path with low resistance remains that mainly affects the total sheet resistance (see inset of figure 5.2d). Therefore, the beam energy and thus the penetration depth plays an important role for investigating disorder in GST films via electrical methods but has no significant impact on the *in-situ* optical measurements at 635 nm for rather thick films ($\gtrsim 100$ nm). However, below the optical gap of GST, i.e., its absorption-free thus transmissive spectral region (mainly in the IR), inadvertent interface mixing for higher ion energies may reduce thin-film interference effects that are then independent of changes in the refractive indices. Therefore, 55 keV Ar⁺-ions were used for the following *ex-situ* measurements to avoid interface mixing.

5.3. Ex-situ measurements on tailored disorder in GST

Section 5.1 revealed that inducing disorder in initially crystalline GST films leads to a gradual change of their electrical and optical properties. However, as the *in-situ* measurements are restricted to a purely phenomenological perspective, other methods need to be exploited in order to gain insights into the various structural and electronic transitions in GST that occur upon ion bombardment. To circumvent these restrictions, the induced disorder in GST films is tailored via ion irradiation with appropriate ion fluences. Thus, multiple, initially rock-salt and hexagonal GST thin films (~ 100 nm) on Si were irradiated at room temperature with 55 keV Ar⁺-ions at 7° angle of incidence with various ion fluences. Optical and structural measurements were performed *ex-situ* on both GST phases subsequent to ion irradiation, respectively. Note that each ion fluence corresponds to a single sample; thus, sample-to-sample variations should be considered.

5.3.1. Disorder-driven metal-insulator transition in hexagonal GST

The influence of ion irradiation on the optical properties of intrinsic hexagonal GST thin films was investigated by a combination of UV-VIS-NIR and FTIR spectroscopy in reflection mode over a broad spectral range. Figure 5.3a shows the reflectance spectra of various, initially hexagonal GST thin films on Si that were irradiated with

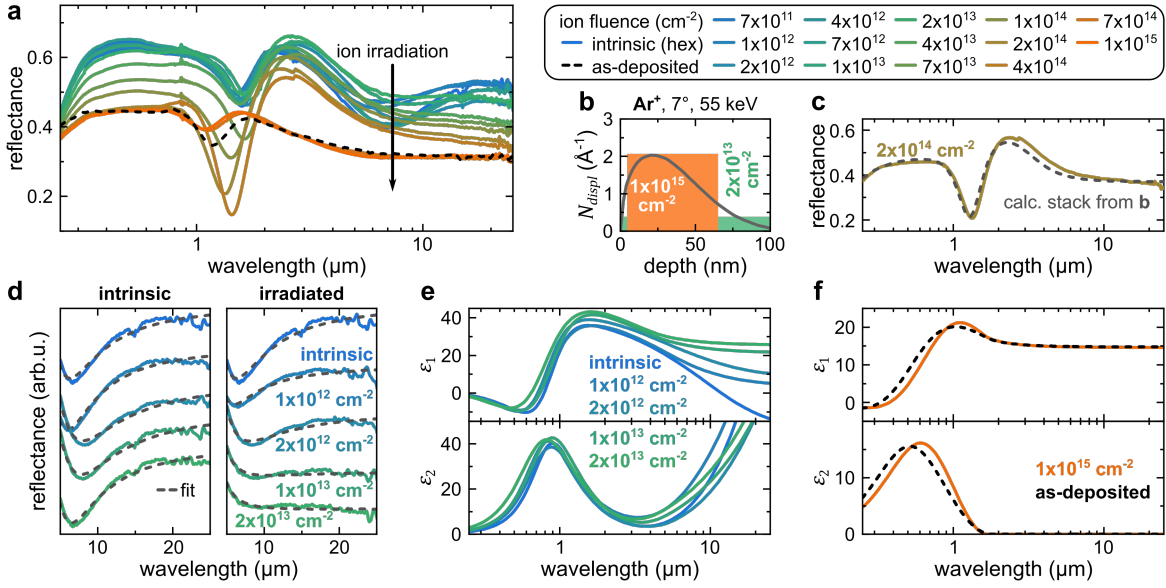


Figure 5.3.: (a) Reflectance spectra of as-deposited (amorphous; black dashed line), intrinsic hexagonal and Ar⁺ irradiated GST thin films ($d \approx 100$ nm) on Si with increasing ion fluences. (b) Total displacements per incident ion N_{displ} for 55 keV Ar⁺-ions into hexagonal GST as a function of depth. Shaded areas demonstrate the simplified layer model used to calculate the reflectance in (c). (c) Experimental reflectance of the sample irradiated with 2×10^{14} cm⁻² compared to the calculated reflectance spectrum of the stack. (d) Selected reflectance spectra in the infrared before (left) and after irradiation with low ion fluences (right) while each color represents one respective sample. All spectra were fitted with the combined Tauc-Lorentz and Drude model in order to extract optical properties of the irradiated GST films. (e) Resulting real ϵ_1 and imaginary part ϵ_2 of the permittivity for the irradiated samples from (d). (f) Comparison of the permittivity of highly irradiated (orange) and as-deposited (black dashed line) GST films.

55 keV Ar⁺-ions with different fluences. Additionally, the spectrum of an as-deposited amorphous film is given as a reference. The reflectance of intrinsic hexagonal GST (blue) has a pronounced Drude contribution that leads to an increased reflectance in the infrared compared to rock-salt GST (compare section 4.4). Small modulations in the near-IR can be attributed to thin film interference (also compare section 4.4). The reflectance decreases mainly in the infrared while remaining roughly constant in the visible to near-IR spectral range upon ion bombardment with low ion fluences up to $\sim 2 \times 10^{13}$ cm⁻². Further irradiation leads also to a decrease of the reflectance in the visible towards complete amorphization at $N_I \approx 7 \times 10^{14}$ cm⁻². The spectra of ion beam amorphized and as-deposited amorphous GST match well.

Furthermore, strong modulations of the reflectance are present in the near-IR spectral range for intermediate stages. The amplitude of these modulations is stronger compared to intrinsic hexagonal or as-deposited amorphous GST thin films. The reflectance in the visible already reaches the value of the amorphous phase for an ion fluence of 2×10^{14} cm⁻², while strong modulations in the near-IR remain and values well below

the reflectance of the Si substrate are detected. This reveals a gradient in the refractive index within the GST film that arises from the non-uniform damage profile of the 55 keV Ar^+ -ions shown in figure 5.3b.

To extract the optical constants of disorder-induced intermediate GST phases, the reflectance spectra of all samples were fitted by a combination of Tauc-Lorentz and Drude dispersion models as introduced in section 4.4. However, the fit fails for films irradiated with fluences between $2 \times 10^{13} \text{ cm}^{-2}$ and $7 \times 10^{14} \text{ cm}^{-2}$ as a single layer model cannot account for a refractive index gradient within the film. Figure 5.3c shows the reflectance of the GST film irradiated with $2 \times 10^{14} \text{ cm}^{-2}$. The reflectance can be described by approximating the damage profile (see figure 5.3b) with a simple three layer model comprising of 60 nm amorphized GST sandwiched by 1 nm (surface side) and 40 nm (interface side) defective but crystalline GST. The fitted optical constants of samples irradiated with ion fluences of $1 \times 10^{15} \text{ cm}^{-2}$ and $2 \times 10^{13} \text{ cm}^{-2}$ were used for amorphized and defective, crystalline GST, respectively. Certainly, this approximation does not resemble the real permittivity gradient inside the GST film, but allows insights into the occurring effects. Around the peak of the damage profile amorphous regions are produced while especially at the interface – but also at the surface – partially crystalline or defective regions are still present due to a lower defect concentration. Increasing the ion fluence above $7 \times 10^{14} \text{ cm}^{-2}$ also leads to amorphization of these defective regions and the gradient index vanishes within the GST film, which leads to complete amorphization of the film. However, as the optical properties of intermediate states cannot be described by a single layer model, effective optical properties for intermediate GST states cannot be extracted for an Ar^+ -ion energy of 55 keV. Increasing the ion energy to create a more uniform damage profile might enable single layer fitting and the extraction of optical constants that well describe intermediate GST states.

Figure 5.3d shows the IR reflectance spectra of hexagonal GST films prior and after irradiation with low ion fluences up to $2 \times 10^{13} \text{ cm}^{-2}$. Spectra of intrinsic films are given to account for the effect of sample-to-sample variations. It is evident that the Drude contribution in the IR drastically changes already for low ion fluences where mainly point defects, such as vacancies, interstitials, or replacements, and small defect clusters are produced. Furthermore, these spectra were also fitted using the combined Tauc-Lorentz-Drude model (gray dashed lines). The extracted complex permittivity is given in figure 5.3e. Indeed, the real part of the permittivity increases mainly in the IR spectral range with increasing ion fluence while the imaginary part remains roughly unchanged. The latter is most likely a result of the aforementioned non-uniform damage profile leading to remaining absorbing regions near the interface. Note that the fitted effective permittivity is quantitatively vague and here only used for qualitative consideration. However, the change in ϵ_1 indicates a decrease of the Drude

contribution that is accompanied with a decrease in free carrier concentration and/or mobility. The vacancy layers resembling the van der Waals gaps in pristine hexagonal GST are responsible for the high mobility due to delocalized states (compare section 2.3.1). Privitera *et al.* [59] suggested that ion irradiation induces a disordering of these vacancies. This vacancy disordering process is accompanied with the formation of localized states and thus vanishing of delocalized states, which leads to a reduction of carrier mobility and indeed is observed in the infrared spectra for low ion fluences. This disorder-driven metal-insulator transition can be regarded as the inverse process of the vacancy ordering induced insulator-metal transition upon thermal annealing (compare section 4.2).

Furthermore, increasing the ion fluence leads to a gradual decrease of the reflectance until saturation above $7 \times 10^{14} \text{ cm}^{-2}$. As the refractive index gradient inside the GST film vanishes at this point, valid optical constants can be extracted out of Tauc-Lorentz fits. The Drude term can be neglected for amorphous GST. The extracted permittivity of highly irradiated and as-deposited amorphous GST given in figure 5.3f is quite similar with only a minor shift of E_0 (compare section 4.4). This deviation can be explained by the existence of diverse amorphous phases [125, 208, 209]. Further analysis of the polymorphism of amorphous GST will be addressed in section 7.1.

In conclusion, already the creation of point defects and small defect clusters in the low fluence regime leads to vacancy disordering in hexagonal GST films inducing a metal-insulator transition. At higher ion fluences accumulation of disorder leads to complete amorphization of the film. To further corroborate these observations from optical measurements, a detailed structural characterization of ion irradiated hexagonal GST films is mandatory.

5.3.2. Disorder-induced structural transitions of hexagonal GST

In order to investigate the effect of ion irradiation on the structural properties of hexagonal GST films XRD measurements were performed on the exact same set of samples from the previous section after the optical measurements. Figure 5.4a shows the obtained XRD pattern of the approximately 100 nm GST films on Si that were irradiated with 55 keV Ar^+ -ions and various ion fluences. The integration time and area was kept constant for all measurements to allow for comparability between all samples. Numerous reflection peaks occur in the pattern of pristine hexagonal GST; however, there is an additional significant contribution from the rock-salt phase, which was discussed in detail in section 4.3. The peak intensities generally decrease upon ion irradiation of the GST films. No reflections are present for ion fluences of $7 \times 10^{14} \text{ cm}^{-2}$ and $1 \times 10^{15} \text{ cm}^{-2}$; thus, these GST films were amorphized confirming the assumption

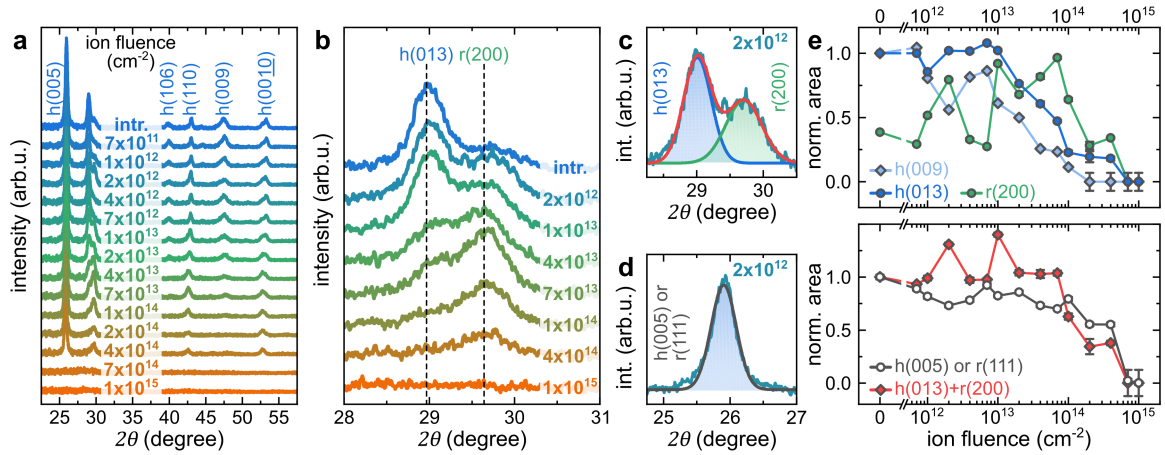


Figure 5.4.: (a) XRD patterns of intrinsic (hexagonal) and Ar^+ irradiated GST thin films ($d \approx 100$ nm) on Si with increasing ion fluences. (b) Zoom at the region around the h(013) and r(200) reflections of some representative samples from (a). (c,d) Exemplary multiple Gaussian peak fits of (c) the h(013) (blue) and r(200) (green) reflections and (d) the superposition of the h(005) and r(111) reflection of the GST film irradiated with $2 \times 10^{12} \text{ cm}^{-2}$, respectively. (e) Extracted Gaussian peak areas of some characteristic reflections normalized to their value of the intrinsic hexagonal GST film. However, the r(200) values are normalized to the value of the intrinsic h(013) reflection to account for different contributions of rock-salt and hexagonal phases.

from optical measurements. Note that XRD only allows for information about the long range order. Other methods, such as Raman or X-ray absorption spectroscopy techniques [109, 253], would have to be exploited in order to investigate the short range order of diverse amorphous phases.

Further insights can be gained by a more detailed inspection at the region around $2\theta \approx 29^\circ$, which is displayed in figure 5.4b. In this range the contribution of the h(013) ($\sim 29.0^\circ$) and the clearly shifted r(200) ($\sim 29.6^\circ$) reflections are located. The intensity change upon ion bombardment already reveals that the ratio of the respective contribution (of hexagonal and rock-salt phase) changes. By fitting these reflections with multiple Gaussian functions (see figure 5.4c) their peak area can be extracted. This examination was also performed for the h(005) (see figure 5.4d) and h(009) reflections with single Gaussian peak fits, respectively. Note that the h(005) reflection is superimposed with the r(111) peak; thus, this reflection mainly represents the overall crystallinity of the films. The fitted peak areas of irradiated GST films were normalized to the respective associated peak area of the intrinsic hexagonal GST sample with the exception of the r(200) peak that was normalized to the area of the intrinsic h(013) reflection to account for different contributions of the respective phases. The normalized areas are displayed as a function of ion fluence in figure 5.4e. Note that the given error bars only correspond to the fit errors and do not account for the error due to sample-to-sample variations.

The normalized area of the h(013) reflection remains roughly constant upon ion bombardment for fluences up to $1 \times 10^{13} \text{ cm}^{-2}$ and then gradually decreases until vanishing at $\sim 7 \times 10^{14} \text{ cm}^{-2}$ due to complete amorphization. In contrast, the trend of the r(200) reflection area first increases up to fluences of $\sim 7 \times 10^{13} \text{ cm}^{-2}$ before it also decreases due to amorphization. Note that the fluctuation of the r(200) peak area is relatively high, which is a result of the aforementioned sample-to-sample variations. Furthermore, there is an inverse correlation between the values of r(200) and h(009) reflections up to fluences of $\sim 1 \times 10^{13} \text{ cm}^{-2}$. While the contribution of the r(200) peak increases the h(009) peak decreases and vice versa. This further indicates deviations between single samples. However, the overall trend clearly reveals an increase of the portion of rock-salt phase inside the film for low ion fluences accompanied with a reduction of the hexagonal phase.

Density functional theory simulations on vacancy layer formation in disordered crystalline GST [59, 160] have shown that the rock-salt structure has a lower formation energy compared to the hexagonal structure when both contain depleted layers with 50% vacancy concentrations. Thus, as the vacancy occupancy of the van der Waals gaps decreases upon ion irradiation to about 50%, the rock-salt structure becomes energetically more favorable. Hence, the energy penalty that occurs upon vacancy disordering in the hexagonal phase is causing the structural transition from hexagonal to rock-salt.

The decrease of the h(009) reflection is shifted to lower fluences compared to the h(013) peak, which indicates a loss of the nine-plane periodicity in hexagonal GST (compare section 2.3.1). Moreover, this reveals that the periodicity that is linked to the van der Waals gaps is lost prior to the phase transformation of the hexagonal structure. In the previous section, IR spectroscopy indicated that the metal-insulator transition caused by vacancy disordering occurs in an ion fluence range of $\sim 1 \times 10^{13} \text{ cm}^{-2}$, which is in good agreement with the decrease of the h(009) reflection. Furthermore, the h(013) peak tends to decrease at higher fluences than $\sim 1 \times 10^{13} \text{ cm}^{-2}$ suggesting that there is no direct correlation between the metal-insulator transition and the structural hexagonal to rock-salt transition, which is in good agreement with previous studies [59, 100].

Furthermore, the overall crystallinity of the initially hexagonal GST thin films is roughly constant up to an ion fluence of $\sim 1 \times 10^{14} \text{ cm}^{-2}$, which is indicated by the normalized area of the superposition of h(005) and r(111) reflections shown in figure 5.4e. Additionally, the sum of the peak areas of h(013) and r(200) is given. It also follows the same trend while small deviations can be explained by sample-to-sample variations. For higher ion fluences the overall crystallinity decreases due to amorphization.

In conclusion, ion irradiation induced disorder causes multiple transitions in hexagonal GST thin films. First, for low ion fluences vacancy disordering leads to an electronic

metal-insulator transition. Increasing disorder further leads to a conversion from the hexagonal to rock-salt structure before a progressive amorphization occurs at high ion fluences. These processes indicate that the van der Waals gaps not only determine the electronic structure but also the stability of the hexagonal GST phase.

5.3.3. Disorder-induced progressive amorphization of rock-salt GST

Similar to the *ex-situ* experiment of hexagonal GST, the effect of ion-beam induced tailored disorder on the optical and structural properties of initially rock-salt GST is examined. The reflectance spectra of intrinsic rock-salt, 55 keV Ar⁺ irradiated and as-deposited amorphous GST thin films ($d \approx 100$ nm) on Si are depicted in figure 5.5a. The reflection spectra remain almost unaffected by ion irradiation up to an ion fluence of $\sim 7 \times 10^{12}$ cm⁻² (green curves). Small deviations can be attributed to sample-to-sample variations, especially in the intended film thickness, leading to shifted thin film interference fringes. In this low ion fluence regime mainly point defects, such as vacancies and interstitials, are formed, which do not seem to alter the optical properties of rock-salt GST. This might be caused by the initially present amount of disorder caused by randomly distributed vacancies in the Ge-sublattice of the rock-salt phase (see section 2.3.1). As the ion fluence increases, the reflectance decreases drastically in the visible and reaches saturation at about 7×10^{13} cm⁻² that corresponds to complete amorphization of GST. This progressive amorphization likely proceeds by accumulation of point defects and small defect clusters or by direct amorphization of small regions within the GST film. Furthermore, the reflectance of highly irradiated GST is similar with that from an as-deposited amorphous GST thin film, which further corroborates ion beam induced amorphization.

Additional to complete amorphization intermediate states are observed. These states correspond to extended defect formation and/or local amorphization inside the rock-salt GST film. Intermediate stages with fluences ranging between 1×10^{13} cm⁻² and 4×10^{14} cm⁻² show distinct modulations in the near-IR, as it was already discussed for intermediate stages of hexagonal GST films (compare section 5.3.1). This effect becomes more evident when comparing the reflectance change as a function of ion fluence at visible (635 nm) and near-IR (3 μ m) wavelengths, which is given in figure 5.5c. As discussed in section 5.2 at 635 nm the light probes mainly the first 50 nm of the film. However, at 3 μ m the extinction of GST is significantly smaller than in the visible; thus, the reflected light contains information from the entire film. Further, due to the non-uniform damage profile of 55 keV Ar⁺-ions, here, a refractive index gradient is present within the GST film. Thus, the effective amorphization threshold shifts to higher ion fluences due to the smaller amount of defects induced near the

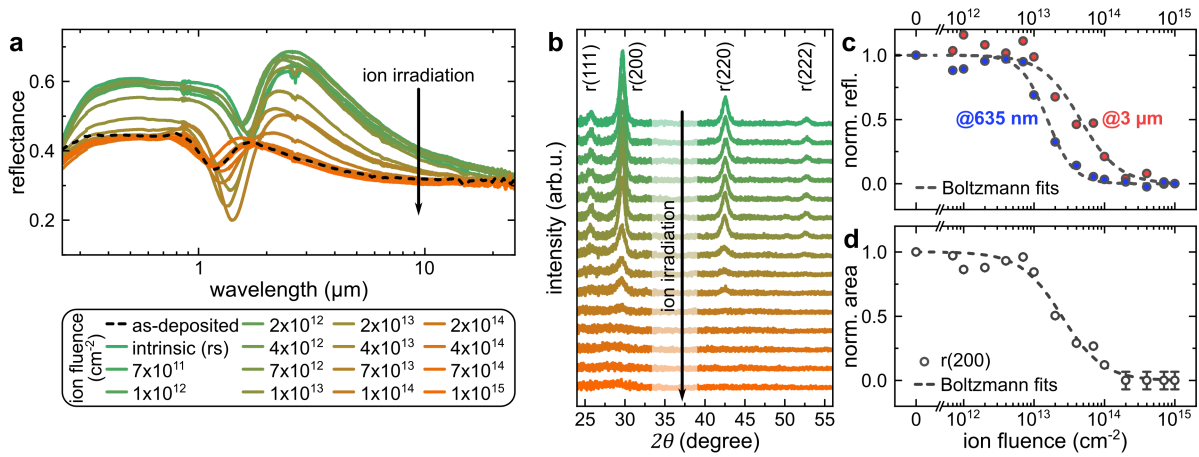


Figure 5.5.: (a) Reflectance spectra and (b) XRD patterns of intrinsic (rock-salt) and 55 keV Ar^+ irradiated GST thin films ($d \approx 100$ nm) on Si with increasing ion fluences. Additionally, a representative reflectance spectrum of a comparable as-deposited (amorphous) GST film on Si is displayed (black dashed line in (a)). (c) Normalized reflectivity in the visible (635 nm, green) and IR (3 μm , red) as a function of ion fluence that were fitted using Boltzmann's sigmoidal equation (gray dashed lines). (d) Extracted Gaussian peak area of the r(200) reflection normalized to the value of the intrinsic rock-salt GST film.

film/substrate interface, which indeed is observed in figure 5.5c.

Furthermore, XRD measurements were performed on the same set of samples. The obtained XRD pattern are given in figure 5.5b. Upon ion irradiation there is a reduction in peak intensity of all reflections of the rock-salt structure. Progressive amorphization of the GST film is observed as no further peaks appear in the XRD pattern. The most intense peak, the r(200) reflection, is used to estimate the crystallinity of the film. Thus, figure 5.5d shows the peak area of r(200) that is extracted using Gaussian function fitting as a function of ion fluence. Furthermore, the r(200) peak intensity and the normalized reflectance at $\lambda = 3 \mu\text{m}$ (see figure 5.5c) follow the same trend. This further corroborates the lower defect concentration near the GST/Si interface due to the non-uniform damage profile, as the XRD pattern also contains information of the entire film.

In conclusion, increasing disorder induced by ion irradiation causes progressive amorphization in initially rock-salt GST films. Bastiani *et al.* suggested that the amorphization process is a purely elastic collision-driven process (nuclear energy loss) while the inelastic contribution (electronic energy loss) can be neglected [58]. Furthermore, intermediate GST states can be achieved by carefully tailor the induced amount of disorder.

5.4. In-situ annealing of defects during ion irradiation

Inducing disorder via ion irradiation causes several structural and electronic transitions in crystalline GST thin films, as discussed in detail in the previous sections. As all measurements were carried out at room temperature, induced lattice damage might be able to partially recover due to the recombination of mobile defects by thermal energy. Thus, the amount of created residual disorder is clearly a consequence of opposing effects: the rate of atomic displacements versus the rate of defect migration and recombination. In order to investigate the effect of defect annealing of both crystalline GST phases, first, the reflectance changes of *in-situ* and *ex-situ* measurements will be compared and, second, the influence of the ion flux on *in-situ* measurements will be discussed.

While *ex-situ* irradiation was performed using 55 keV Ar⁺-ions at 7° angle of incidence, this angle had to be adjusted to approximately 45° for the *in-situ* measurement due to the vacuum chamber's geometry (see section 3.4.2). Figure 5.6a shows the total displacements per incident ion N_{displ} calculated via SRIM for Ar⁺-ion energies and angles of incidence that were used for the *ex-situ* (purple) and *in-situ* (red) measurements, respectively. The energy for the 45° irradiation was chosen to 100 keV so that the depth profile of N_{displ} is similar to the 55 keV, 7° irradiation. However, the overall N_{displ} is slightly higher for 100 keV. Consequently, to account for different N_{displ} of the respective measurements, the number of displacements per lattice atom was calculated with:

$$n_{dpa} = \frac{N_{displ}^{max} \times N_I}{n_{at}}, \quad (5.1)$$

using the maximum of the number of displacements per incident ion N_{displ}^{max} (with ion fluence N_I). Note that the atomic density n_{at} slightly changes upon irradiation. As an approximation, for the calculation of n_{dpa} only the initial values of the respective GST phases were assumed.

The reflectance at $\lambda_c = 635$ nm of approximately 100 nm crystalline GST films on Si upon ion irradiation is given in figure 5.6 for *in-situ* and *ex-situ* measurements, respectively. *Ex-situ* reflectance values are directly measured via UV-VIS spectroscopy after irradiation. However, absolute values of the reflectance change obtained from *in-situ* optical measurements were referenced to the calculated reflectance values of intrinsic hexagonal and rock-salt GST thin films, respectively (compare section 4.4). As previously discussed the reflectance decreases upon ion bombardment due to amorphization in both experiments. However, it is evident that this decrease is shifted to higher n_{dpa} in the *ex-situ* measurements for both crystalline GST phases (compare figure 5.6b). This can be clearly attributed to annealing of lattice defects through migration and recombination. For *ex-situ* measurements the reflectance is roughly constant (conside-

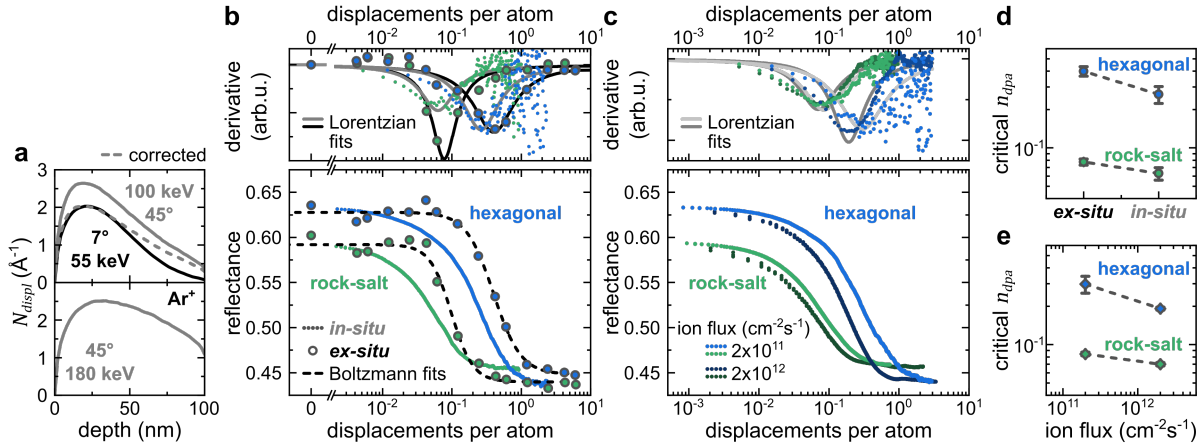


Figure 5.6.: (a) Total displacements per incident ion N_{displ} for Ar^+ -ions into crystalline GST with ion energies 55 keV for 7° incidence angle (black), 100 keV and 180 keV for 45° incidence angle (gray). The gray dashed line represents the 100 keV irradiation that is corrected to the peak displacements of the 55 keV irradiation to account for different irradiation conditions of *in-situ* and *ex-situ* experiments. (b) Comparison of the reflectance at 635 nm of initially rock-salt (green) and hexagonal (blue) GST films on Si upon Ar irradiation for *in-situ* (constant flux of $2 \times 10^{11} \text{ cm}^{-2}\text{s}^{-1}$) and *ex-situ* experiments as a function of displacements per lattice atom with respective ion energies and incidence angle of (a). *Ex-situ* measurements were fitted using Boltzmann's sigmoidal equation (black dashed lines). Additionally, respective derivatives of all curves are fitted (on a logarithmic scale) with Lorentzian distribution functions (solid lines). (c) *In-situ* optical measurements of initially rock-salt (green) and hexagonal (blue) GST films on Si upon Ar irradiation for different ion fluxes together with respective derivatives and Lorentzian fits. (d,e) Extracted critical number of displacements per atom n_{dpa} corresponding to the peak position of the fitted Lorentzian functions to compare (d) *in-situ* and *ex-situ* experiments and (e) different ion fluxes.

ring the UV-VIS uncertainty) up to about $n_{dpa} \approx 0.05$ and ≈ 0.1 for the rock-salt and hexagonal phase, respectively. Thus, point defects and small defect clusters might be able to recover almost completely within the time at RT (\sim hours) between irradiation and optical measurement. On the contrary there is a gradual decrease of the *in-situ* reflectance change for both phases. Here, the time is not sufficient to recover even for small amounts of point defects before the ongoing ion bombardment leads to the formation of larger, more stable defects.

To gain further insights in the annealing process during ion irradiation of GST thin films, *in-situ* optical measurements were performed with different ion fluxes, which corresponds to an altered rate of atomic displacements. However, the rate of defect migration and recombination should be independent on the ion flux and only depend on the sample's temperature. Note that for the used ion fluxes significant heating of the sample caused by the ion beam is unlikely and thus neglected. For these measurements an ion energy of 180 keV was used to obtain a near uniform damage profile, which is shown in figure 5.6a (black curve). The impact of the non-uniform damage profile on

optical measurements in the visible is negligible, which was demonstrated in section 5.2. Figure 5.6c shows the *in-situ* reflectance change of initially rock-salt and hexagonal GST films ($d \approx 100$ nm) on Si. Apparently, increasing the ion flux by an order of magnitude leads to a shift of the amorphization threshold to smaller n_{dpa} values for both phases resulting from an increased rate of atomic displacements. Moreover, this shift is smaller for the rock-salt than for the hexagonal phase indicating a lower annealing rate. This is further corroborated by an overall lower amorphization threshold of rock-salt GST.

By neglecting directional effects of ion irradiated polycrystalline films, as discussed in section 5.1, the rate of atomic displacements should be independent of the crystal structure of chemically identical media. However, the mobility and recombination process of defects strongly depends on the crystal structure of GST. This is a consequence of different diffusion paths of defects and dislocated lattice atoms that clearly depend on the local atomic arrangement. It was reported that the van der Waals gaps in hexagonal GST serve as preferential sinks where displaced atoms are able to recombine [61]. Due to unfavorable Te-Te antibonds and low mobility of Te atoms primarily Ge and Sb tend to migrate and recombine in the gaps. As these gaps are not found in rock-salt GST, the resulting annealing rate is higher in the hexagonal phase, which leads to an increased critical n_{dpa} for amorphization.

Furthermore, critical values of n_{dpa} were extracted from Lorentzian fits to the derivatives of both *ex-situ* and *in-situ* measurements (see figure 5.6b) and the different ion fluxes (see figure 5.6c), which are depicted in figure 5.6d and e, respectively. While *ex-situ* measurements result in a ~ 1.5 times higher critical n_{dpa} for hexagonal GST compared to *in-situ*, this ratio is reduced to ~ 1.2 for the rock-salt phase. Coincidentally, very similar values were achieved by comparing the different ion fluxes in *in-situ* measurements. However, these observations further corroborate a higher defect mobility and recombination rate of hexagonal than rock-salt GST. Furthermore, the comparison of *ex-situ* and *in-situ* measurements suggests that the annealing of defects is on the time scale of seconds (or even less) rather than hours.

5.5. Temperature dependence of tailored disorder in GST

One of the key features of phase-change materials, in particular GST, is the repeatable switching between crystalline and amorphous phases. Thus, it is crucial for any GST-based applications to investigate whether ion beam induced disorder can be totally reversed upon thermal annealing. First, reconfigurability of amorphized GST films is demonstrated by means of UV-VIS spectroscopy and TRR measurements. Second, the thermal stability of tailored disorder in GST films is addressed.

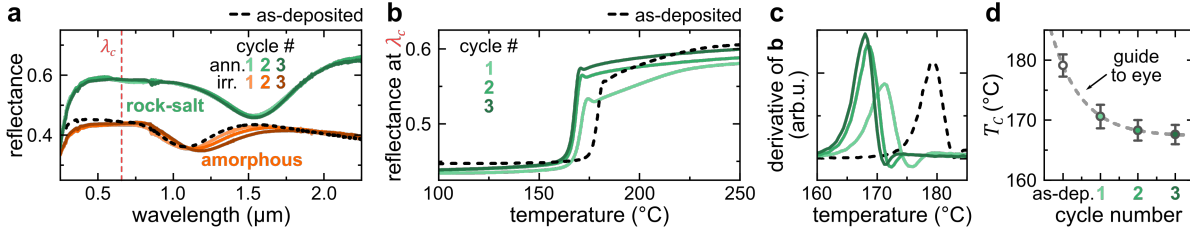


Figure 5.7.: (a) Reflectance spectra of a GST film ($d \approx 100$ nm) on Si, which was repeatably Ar^+ irradiated with $4 \times 10^{14} \text{ cm}^{-2}$ (amorphized with $E_{\text{Ar}^+} = 55$ keV, orange) and annealed to 250°C (rock-salt; green). Additionally, the spectra of the sample in the as-deposited state (amorphous; black dashed line) is given for comparison. (b) Reflectance at a wavelength of $\lambda_c = 635$ nm of the as-deposited and irradiated films from (a) during heating (heating rate 25 K/min). (c) Derivative of the reflectance change as a function of temperature. (d) Critical temperatures for crystallization as a function of cycle number. Error bars correspond to the full-width at half maximum of the first derivatives from (c).

5.5.1. Reconfigurability of ion beam amorphized GST films

One single GST film ($d \approx 100$ nm) on Si was repeatedly irradiated with $N_I = 4 \times 10^{14} \text{ cm}^{-2}$ ($E_{\text{Ar}^+} = 55$ keV) and subsequently annealed up to 250°C . The latter leads to a conversion into the rock-salt phase (compare section 4.2), while ion irradiation with this fluence leads to amorphization of the GST film. Note that prior to the first irradiation the sample was in the as-deposited state, thus, not crystallized. Figure 5.7a shows the reflectance spectra of the GST film in the crystalline (rock-salt, green), ion beam amorphized (orange), and as-deposited amorphous (black dashed line) state. The reflectance of the rock-salt phase is clearly unchanged after three cycles. As previously observed the optical properties of as-deposited and ion irradiated amorphous GST are slightly different; still, they are approximately unchanged after multiple irradiation-annealing-cycles. Thus, reconfigurability for at least a few switching cycles is confirmed. It is worth noting that ion irradiation also leads to sputtering of target atoms corresponding to a reduction of the film thickness for very high ion fluences. The sputtering yield can be calculated via SRIM and is ~ 5.4 atoms/ion for the used 55 keV Ar^+ -ions and near normal incidence. Thus, there is a reduction of the average film thickness of only ~ 0.6 nm for $N_I = 4 \times 10^{14} \text{ cm}^{-2}$. Multiple cycles lead to an accumulation of this value limiting the total number of cycles.

Moreover, temperature-resolved reflectance (TRR) measurements were performed to investigate the effect on the crystallization upon repeatable ion irradiation as depicted in figure 5.7b. Here, absolute reflectance values were calculated using UV-VIS spectroscopy reflectance values of the sample before annealing. There is a significant difference in the crystallization kinetics of as-deposited and ion irradiated GST. For the latter the onset of crystallization is shifted to lower temperatures. By differentiating the TRR curves (see figure 5.7c), critical temperatures for crystallization T_C can be

extracted and are depicted in figure 5.7d as a function of cycle number. Apparently, T_C decreases after ion irradiation of as-deposited GST and further decreases after an annealing-irradiation step. However, this shift saturates after a few cycles and is a result of different amorphous phases. The effect of ion irradiation on the crystallization kinetics will be discussed in more detail in chapter 7.

5.5.2. Thermal stability of intermediate states

Another key challenge for GST-based devices that rely on tailored disorder is the thermal stability of ion beam induced intermediate states. In order to investigate the stability upon thermal annealing one initially rock-salt and one hexagonal GST film (both $d \approx 100$ nm) were successively irradiated with various ion fluences below and in the vicinity of the amorphization threshold. Note that the Ar^+ -ion energy was slightly increased to 75 keV compared to prior experiments leading to a slightly more uniform damage profile. Between each irradiation step the samples were annealed up to 225 °C and 350 °C for the initially rock-salt and hexagonal sample, respectively. Reflectance spectra were measured using a combination of UV-VIS and FTIR spectroscopy before and after each irradiation/annealing step.

Figure 5.8a displays the reflectance spectra of the rock-salt and hexagonal GST film in the intrinsic and various irradiated states, respectively. The gradual change of optical properties is in good agreement with the observations from sections 5.3.3 and 5.3.1. Furthermore, intermediate states were annealed after irradiation using the TRR setup allowing to examine their stability upon thermal heating, which is shown in figure 5.8b for both samples, separately. Ion irradiation of an initially rock-salt GST film on Si with a low ion fluence of $N_I = 5 \times 10^{12} \text{ cm}^{-2}$ leads to a slight decrease of the reflectance at 635 nm; subsequent thermal annealing (up to 225 °C) then results in an increase of the reflectance back to the initial value. This increase occurs at temperatures well below the amorphous to rock-salt phase-transition; however, the reflectance is constant up to about 50 °C. The phase-transition is very broad for low ion fluences and becomes sharper with increasing ion fluences. Furthermore, the phase-transition temperature is shifted to higher temperatures with increasing ion fluence, i.e., with a larger amount of induced lattice disorder. At the highest used ion fluence well above the amorphization threshold, there is still a discrepancy between the phase-transition temperatures of ion beam amorphized and as-deposited amorphous GST films of ~ 10 °C. This was already observed in the previous section and will be discussed in section 7.1.

Moreover, an initially hexagonal GST film was examined in a comparable manner. Low ion fluences do not change the reflectance in the visible but mainly in the infrared due to an electronic metal-insulator transition in an unaltered structure, which was

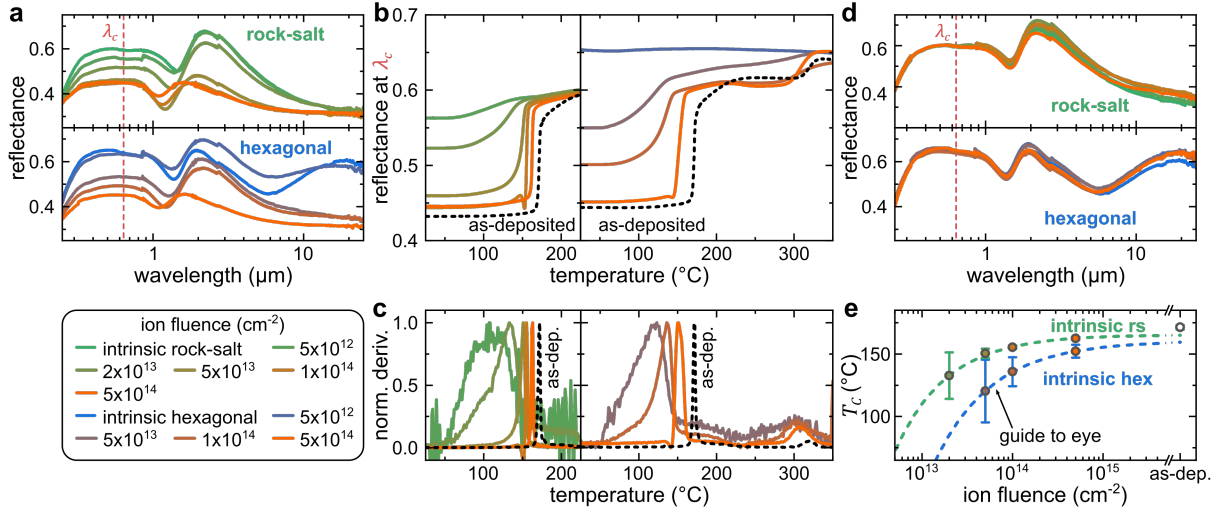


Figure 5.8: (a) Reflectance spectra of GST films ($d \approx 100$ nm) on Si initially in the rock-salt (green) and hexagonal phase (blue) and after successive ion irradiation with various ion fluences ($E_{Ar^+} = 75$ keV), respectively. (b) Reflectance at a wavelength of $\lambda_c = 635$ nm during heating (heating rate 20 K/min) of the samples from (a) and (c) the corresponding normalized derivatives. (d) Reflectance spectra after each annealing step. (e) Critical temperatures for crystallization T_C (amorphous to rock-salt) as a function of ion fluence. Error bars correspond to the full-width at half maximum of the first derivatives shown in (c).

previously discussed. Thus, no change in reflectance at 635 nm can be observed in the TRR curve of the $N_I = 5 \times 10^{12} \text{ cm}^{-2}$ irradiated sample in figure 5.8b. Consequently, the reflectance of this sample remains constant upon heating. Increasing the ion fluence to $5 \times 10^{13} \text{ cm}^{-2}$ leads also to a decrease in reflectance below the value of a comparable rock-salt GST film. Two distinguishable phase transitions are observable in the respective TRR curve, which correspond first to a transition from highly defective or amorphous regions to rock-salt phase and second to a conversion from rock-salt to hexagonal GST. While the first transition is comparable to the case of irradiated initially rock-salt GST, the second transition is very broad. This particular intermediate state appears also to be stable up to temperatures of about 50 °C.

Further increasing the induced lattice damage leads to a shift of both transitions to higher temperatures. The reflectance after the first transition of the GST film irradiated with $1 \times 10^{14} \text{ cm}^{-2}$ matches well with the value of rock-salt GST revealing a complete structural conversion from the hexagonal to rock-salt phase prior to annealing, which was discussed in section 5.3.2. Note that due to the non-uniform damage profile, there are also highly defective or amorphous regions within the film reducing the overall reflectance below the rock-salt value (before annealing). The second transition from rock-salt to hexagonal structure upon heating to ~ 300 °C is still broadened compared to the as-deposited film, which might be also caused by the defect distribution.

Furthermore, the highest used ion fluence ($5 \times 10^{14} \text{ cm}^{-2}$) leads to amorphization of

the initially hexagonal GST film. However, the shift in crystallization temperature is significantly higher than the about 10 °C observed for the highest irradiated, initially rock-salt GST film. This likely is a result of an incomplete amorphization of the film for this ion fluence. However, the second transition, i.e., the conversion from rock-salt to hexagonal, is in the vicinity of and as sharp as the intrinsic (as-deposited) phase transition. This implies that the second transition may not be affected by the local arrangement of the amorphous state prior to crystallization.

Again critical temperatures for crystallization T_C (amorphous to rock-salt) were determined from the first derivative (shown in figure 5.8c) of the TRR curves as a function of ion fluence (see figure 5.8e). It is evident that T_C increases with increasing ion fluence towards to value of the transition from as-deposited amorphous GST for both initial phases. However, fitting of an exponential decay indicates that T_C of irradiated GST saturates below the value of as-deposited GST films, which is indeed expected from the previous section. Additionally, the width of the transitions is given as the full width at half maximum from the first derivative of the TRR curves (error bars in figure 5.8e). Obviously, the transitions become sharper with increasing ion fluence.

Furthermore, the reflectance spectra taken after each annealing step are given in figure 5.8d for both initial phases, respectively. As the reflectance is similar after all irradiation-annealing steps, it is evident that intermediate states can be totally recovered via thermal annealing regardless of the initial crystal structure, which correlates well with the reconfigurability of ion beam amorphized GST films approved in the previous section. Moreover, the intermediate states presented here are stable up to about 50 °C corresponding to stable induced lattice defects at ambient temperatures.

5.6. Tailorable near-zero reflection – an application

Introducing the degree of freedom to tailor the amount of disorder in GST thin films already enables the design of diverse optical devices. Thin films are conventionally utilized as optical coatings to either suppress or enhance the light reflection of an optical device. Commonly, dielectric materials are exploited as single- or multi-layer coatings with thicknesses of a quarter- or half-wavelength resulting in anti-reflection or high-reflection, respectively. Moreover, it was recently demonstrated that lossy coatings lead to a reduction of the respective layer thickness for anti-reflection coatings [62, 63]. However, anti- and high-reflection coatings are both based on thin film interference effects that strongly depend on the layer thickness and refractive index. Standard optical materials are limited to distinct values of the refractive index. Thus, to achieve a desired optical response, commonly elaborated multi-layer stacks are fabricated. Phase-change materials, such as GST, readily provide multiple refractive index values

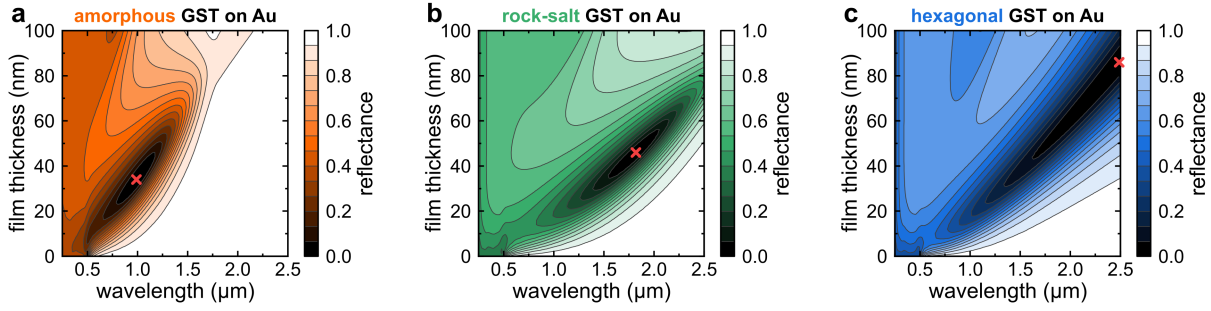


Figure 5.9.: Calculated reflectance maps as a function of film thickness and wavelength for an arbitrary GST thin film on Au in the (a) amorphous (as-deposited), (b) rock-salt, and (c) hexagonal phase, respectively. Red crosses mark the position of minimal reflectance.

depending on their phase. Moreover, tailoring disorder in GST can be utilized to enable a refractive index trajectory, where the optical properties can be designed at will. Thus, appropriate stacking of a thin GST film on top of suitable substrates allows for switchable optical responses. This can be found in numerous applications such as color tuning, thermal emitters, or optical limiters [254–256].

As the refractive index of all GST phases is generally lower than that of metals in the NIR spectral range, it is possible to exploit an appropriately designed GST thin film on top of a metallic reflector with high refractive index to achieve near-zero reflectance. In order to obtain a suitable GST layer that can effectively suppress light reflection of a gold substrate, the reflectance of such a stack was calculated as a function of film thickness and wavelength for all GST phases (refractive index values of GST and Au were taken from section 4.4 and reference [257], respectively) and is depicted in figure 5.9.

With GST in the amorphous (as-deposited) state there is a reflectance near zero around $\lambda \approx 1 \mu\text{m}$, while the corresponding GST film thickness is roughly 30 to 40 nm (see figure 5.9a). For higher wavelengths the reflectance drastically increases to almost 1 (> 0.95). In that region amorphous GST is basically transparent and the high reflectance can be attributed to the Au substrate. The lower wavelength limit of high reflectance is red-shifted with increasing GST thickness, as absorption in the film strongly depends on the optical path length of light.

Furthermore, switching GST to the rock-salt phase leads to a red-shift of the near-zero reflection with a slightly increased required film thickness, which is shown in figure 5.9b (red cross). Remarkably, while the region around $1.8 \mu\text{m}$ shows near-zero reflectance ($R < 5 \times 10^{-4}$) for rock-salt GST, in the same region high reflection ($R > 0.98$) is obtained for the amorphous phase. As a result a reflectance contrast of $\gtrsim 98\%$ can be achieved for a switchable GST thin film with a thickness of about 50 nm on Au. This is clearly a consequence of the combination of different refractive indices

of the amorphous and rock-salt GST phase and the interference effect within the GST film that is enhanced by the highly reflective Au substrate. Note that for a comparable GST film on a Si substrate there is a reflectance contrast of only $\sim 30\%$ over the whole NIR spectral range.

Furthermore, a reflectance map was calculated for a hexagonal GST thin film on Au (see figure 5.9c). Here, the reflectance minimum is shifted further to higher wavelengths and also to higher film thicknesses. Moreover, the region of minimal reflectance values is expanded well in the IR, which is a result of high refractive index values due to the strong Drude contribution of hexagonal GST in that particular region. However, as hexagonal GST is thus more suitable for near-zero reflection at wavelengths higher than $2\ \mu\text{m}$ and thicker films, it is less applicable for e.g. telecommunication wavelengths ($\lambda \approx 1550\ \text{nm}$) where rock-salt GST might be used preferably.

5.6.1. Intrinsic properties of a GST thin film on Au

Figure 5.10a shows an SEM image of a cross-section lamella that was taken out of an approximately 40 nm rock-salt GST film on a gold coated silicon substrate (Au/Si, compare section 3.1). The platinum layer was deposited after the optical measurements on top of GST as it is required for FIB lamella preparation. The thickness of the Au layer, which was deposited on top of a titanium adhesion layer for higher stability, was chosen in order to achieve optically bulk-like behavior of the stack (compare also appendix A.1). Due to the sputter deposition of the Au/Ti layer, the interface between GST and Au as well as the GST surface (prior to Pt deposition) show increased roughness compared to the Ti-Si interface and GST films on bare Si substrates from previous sections. Subsequently to the GST deposition the sample was thermally annealed up to $300\ ^\circ\text{C}$ in an Ar atmosphere. It is known that Au films tend to form clusters at temperatures above $300\ ^\circ\text{C}$ despite the added Ti adhesion layer [258]. Consequently the annealing temperature was limited to $300\ ^\circ\text{C}$; heating a sample to higher temperatures indeed lead to clustering of the Au layer, which could already be seen by eye. Thus, the conversion of GST into the hexagonal phase was not accessible, which was confirmed by XRD (see figure 5.10b). Here, only reflections of the rock-salt GST phase and from the Au substrate can be identified.

Figure 5.10c shows the reflectance spectra of GST thin films deposited on Au/Si with three different thicknesses of about 30 nm, 35 nm, and 40 nm prior and subsequent to thermal annealing. The GST films in the amorphous (as-deposited) state show the predicted reflectance minima around $\lambda \approx 1\ \mu\text{m}$ and high reflectance values for higher wavelengths. However, the measured high reflectance values are significantly lower than the predicted calculated values, which is a result of scattering losses at the

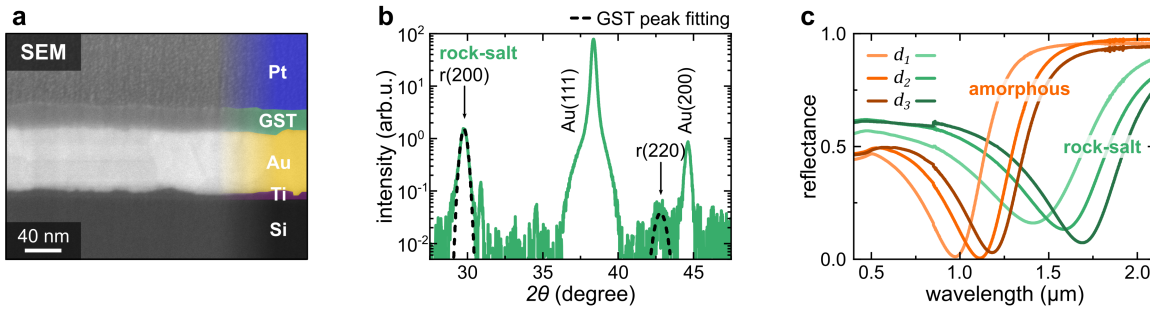


Figure 5.10.: (a) SEM image of a cross-sectional lamella and (b) XRD pattern of an approximately 40 nm GST film on a gold coated silicon substrate in the rock-salt phase. The Pt layer was deposited for lamella preparation and was not present in the optical measurements. (c) Experimental reflectance spectra of as-deposited amorphous and rock-salt GST films on Au/Si with three different thicknesses ($d_1 \approx 30$ nm, $d_2 \approx 35$ nm, and $d_3 \approx 40$ nm).

rough surface and interface of the GST layer. Conversion of the amorphous films to rock-salt GST shifts the reflectance minima to higher wavelengths as expected from the previous calculations. A value of about 7% is measured at the wavelength of minimal reflectance ($1.7 \mu\text{m}$) for the thickest rock-salt GST film ($d \approx 40$ nm). Thus, although the used thicknesses are below 40 nm and the rock-salt GST films do not show near-zero reflectance, an immense reflectance contrast of about 80% is achieved. This confirms that appropriate stacking of GST thin films on top of a metallic reflector such as Au results in near-zero reflectance. The point of minimal reflection depends slightly on the GST film thickness but even more on the phase (diverse optical properties).

5.6.2. Manipulating near-zero reflection via tailoring disorder

As demonstrated in section 5.3.3, gradual changes of the optical properties can be induced by tailoring the amount of disorder inside an initially rock-salt GST thin film via ion irradiation. Thus, gradually tailoring the refractive index can be utilized in order to manipulate near-zero reflection of the samples from the previous section. For this purpose, the approximately 40 nm rock-salt GST film on top of Au/Si was irradiated with 30 keV Gallium-ions at room temperature. The usage of Ga instead of Ar was chosen because further experiments on the same set of samples were performed using a focused ion beam system. Commonly, FIB systems are restricted to a Ga^+ -ion source and a maximal acceleration voltage of 30 kV. However, the irradiations here were performed using the large-scale accelerator, but in order to ensure comparability 30 keV Ga^+ -ions were used. *In-situ* electrical measurements on a hexagonal GST thin film confirmed that Ga^+ -ions can also be utilized to amorphize GST thin films (for details see Appendix A.2).

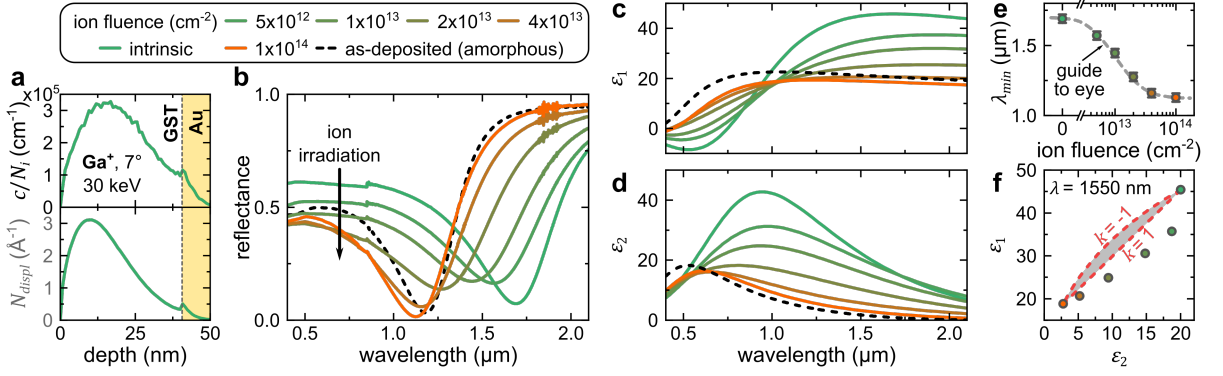


Figure 5.11.: (a) Ga concentration per ion fluence c/N_i (top) and total displacements per ion N_{displ} (bottom) for Ga^+ -ions into a rock-salt GST film on Au. (b) Reflectance spectra of an approximately 40 nm GST film on Au/Si after successive ion irradiation with various ion fluences. Additionally, the reflectance spectrum of the same film in the as-deposited amorphous state is shown (black dashed line). (c) Real ϵ_1 and (d) imaginary part ϵ_2 of the effective permittivity of various irradiated GST films extracted from fits to the corresponding spectra in (b). (e) Point of minimal reflectance λ_{min} as a function of ion fluence. (f) Permittivity values at $\lambda = 1.55$ μm from (c) and (d) in comparison to predictions from effective medium theory (gray shaded area) with Wiener boundaries (red dashed lines).

Due to the restrictions to 30 keV Ga^+ -ions and the desired GST film thicknesses to achieve near-zero reflection on Au, it is crucial to estimate the irradiation damage profile, which is given in figure 5.11a together with the normalized Ga concentration profile. Apparently, the damage profile of Ga into rock-salt GST ($d \approx 40$ nm) has a maximum at about 10 nm while being very non-uniform. As demonstrated in sections 5.3.3 and 5.3.1 the non-uniformity might have an influence on the reflectance spectrum due to a gradient index inside the film.

Reflectance spectra of an initially rock-salt GST film ($d \approx 40$ nm) on Au/Si are given in figure 5.11b prior and after successive Ga^+ -ion irradiation for various ion fluences. Additionally, the reflectance of the same sample in the as-deposited amorphous state (black dashed line) is shown. Increasing disorder induced by the ion beam leads to a continuous change of the reflectance spectrum. Further irradiation with ion fluences above $N_i = 1 \times 10^{14} \text{ cm}^{-2}$ does not change the spectrum significantly (not shown), which indicates an amorphization threshold of the GST film at this ion fluence. Moreover, complete amorphization is also implied by comparing the amorphized reflectance spectrum ($N_i = 1 \times 10^{14} \text{ cm}^{-2}$) with that of the as-deposited (amorphous) state. Slight differences are a result of slightly different refractive indices of diverse amorphous states, which was discussed previously (and in more detail in section 7.1). Note, that at the highest shown ion fluence less than 0.1 at.% Ga is incorporated at the ion range maximum of the Ga concentration. Nevertheless, Ga^+ -ions can be also used to tailor disorder in GST films while there is no evidence of distinct differences to Ar^+ irradiation.

Apparently, tailoring the amount of induced disorder inside the GST film allows for manipulating the point of minimal reflectance between the rock-salt and amorphized state. Figure 5.11e shows the wavelength of minimal reflection λ_{\min} as a function of ion fluence. A gradual blue-shift of λ_{\min} from $\sim 1.7 \mu\text{m}$ for the intrinsic rock-salt state to about $1.1 \mu\text{m}$ at the amorphization threshold is observed. Furthermore, there is a gradual increase of the reflectance value at $\lambda \approx 1.7 \mu\text{m}$ with increasing ion fluence. Considering that the reflectance of the intrinsic state can be further reduced by appropriately choosing the desired GST film thickness, this method allows for arbitrarily tailoring the optical response between near-zero and high reflection.

Furthermore, effective optical properties of the intermediate GST phases were extracted by fitting the reflectance spectra using again the Tauc-Lorentz model and transfer matrix method (as described in section 3.5). The extracted optical constants correspond to effective values, as the GST film is treated like a single layer in the fit neglecting the non-uniform damage profile. The real and imaginary part of the effective permittivity are given in figure 5.11c and d, respectively, for the GST thin film in the as-deposited, rock-salt, and intermediate states. Note that the GST film thickness increases upon progressive ion irradiation caused by the lower density of amorphous compared to crystalline GST (compare section 4.4) [250]. Moreover, ion beam sputtering reduces the film thickness, but was estimated via SRIM [81] to be less than 1 nm for the highest ion fluence and can thus be neglected. The thickness change is considered in the fit; however, it only slightly influences the resulting optical properties. The effective permittivity gradually changes upon progressive ion irradiation until saturating at the amorphization threshold. Moreover, slight differences of the optical constants between the ion beam amorphized and as-deposited amorphous states are clearly visible. Nevertheless, tailoring disorder in GST thin films can indeed be utilized to gradually modify the optical properties of GST.

Figure 5.11f illustrates the effective permittivity values at $\lambda = 1.55 \mu\text{m}$ of the successively irradiated GST film (color-code corresponds to fluence values of figure 5.11b-d). Effective permittivity values can be calculated via effective medium theory (gray shaded area) considering an effective medium as a two component system consisting of amorphous inclusions with sizes much smaller than the wavelength of light inside a crystalline matrix. For the calculation the extracted permittivity values of intrinsic rock-salt and amorphized ($N_i = 1 \times 10^{14} \text{ cm}^{-2}$) GST were used. The effective permittivity can then be calculated via:

$$\tilde{\epsilon}_{\text{eff}}^k = f\tilde{\epsilon}_{\text{am}}^k + (1 - f)\tilde{\epsilon}_{\text{rs}}^k, \quad (5.2)$$

with the amorphous fraction f and the anisotropy exponent k depending on the specific micro-geometry. Moreover, all possible effective optical constants of any composite are

restricted to two extreme cases: that is polarized light with an E-field vector that is either parallel or perpendicular to a lamellar structure, which is known as the Wiener bounds [259]. The upper ($k = 1$) and the lower bound ($k = -1$) are restricting all possible values of the mixture (red dashed lines in figure 5.11f).

The extracted permittivity values of the successively irradiated GST film are not within the predicted effective medium range; thus, they do not represent a simple two component mixture of amorphous and crystalline regions. As was discussed in section 5.3.3 prior to creating amorphous regions inside the crystalline matrix defective regions comprising point defects and small defect clusters are formed. These defective regions might have considerable different optical constants than either amorphous or rock-salt GST, which would lead to the non-trivial permittivity trajectory.

5.6.3. Comparison of large-scale and focused ion beam irradiation

Focused ion beam (FIB) irradiation can be also utilized to induce disorder in GST thin films. Moreover, an FIB further allows to irradiate very confined regions with arbitrary shapes and sizes. This would enable controlling the amount of disorder in GST locally, which opens new routes for realizing diverse optical devices (see chapter 6). However, first it is necessary to compare the effect of FIB irradiation with that of the large-scale accelerator on the properties of GST. Therefore, one GST thin film on Au/Si from section 5.6.1 with a thickness of ~ 35 nm was irradiated in restricted areas of $200 \times 200 \mu\text{m}^2$ with 30 keV Ga^+ -ions using the FIB as schematically depicted in figure 5.12b. Note that the same ion fluences as for the large-scale irradiation were used. Reflectance spectra inside the irradiated areas were taken using a microscope that is attached to an FTIR (see section 3.2.2) and are shown in figure 5.12c for the ~ 35 nm GST film. The depicted wavelength range is limited by the used InGaAs-detector of the FTIR but certainly covers the interesting region that contains reflectance minima for all phases. The overall trend that is visible in the reflectance spectra of the FIB irradiated sample is in good agreement with the reflectance spectra from the large-scale irradiated sample shown in figure 5.12a. Differences in the values of λ_{min} can be attributed to the slightly different film thicknesses. Although the same ion fluences were used, the film thickness further plays a role in determining the integral amount of induced lattice damage, which leads to a slightly lowered amorphization threshold for the thinner film. However, clearly FIB irradiation can be utilized to tailor disorder in GST thin films with an additional control of the shape and size of irradiated regions.

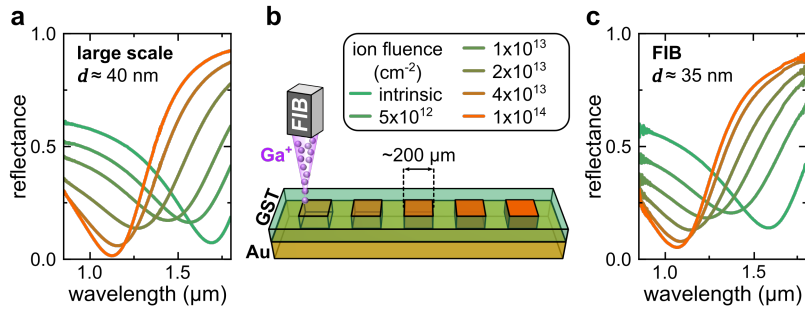


Figure 5.12.: (a) Reflectance spectra of an approximately 40 nm GST film on Au/Si after successive ion irradiation with various ion fluences using the large-scale accelerator. (b) Schematic depiction of local ion irradiation in restricted areas of approximately $200 \times 200 \mu\text{m}^2$ using the focused ion beam. (c) Reflectance spectra of irradiated regions inside an approximately 35 nm GST film on Au/Si with various ion fluences using the FIB.

5.7. Conclusions

This chapter unambiguously demonstrated that ion irradiation can be utilized to tailor disorder in a phase-change material. A combination of *in-situ* optical and electrical measurements was performed at room temperature during noble gas ion bombardment of initially rock-salt and hexagonal GST thin films, respectively. Ion irradiation of approximately 100 nm GST films on SiO_2/Si with 180 keV Ar^+ -ions results in complete amorphization of GST, which occurs at ion fluences of $\sim 1 \times 10^{14} \text{ cm}^{-2}$ and $\sim 5 \times 10^{14} \text{ cm}^{-2}$ for the rock-salt and hexagonal phase, respectively. The lower amorphization threshold of the rock-salt phase can be attributed to its inherently present amount of disorder in contrast to the ordered hexagonal phase (compare section 2.3.1). The phase transformation from crystalline to amorphous is accompanied with drastic changes of the respective reflectance and resistance.

Furthermore, *ex-situ* optical and structural measurements on tailored disorder reveal several structural and electronic transitions in GST thin films. While the transition from rock-salt to amorphous GST is caused by progressive amorphization via the accumulation of lattice defects, several transitions occur in hexagonal GST upon ion irradiation. Already the creation of point defects and small defect clusters leads to disordering of inherent vacancy layers (van der Waals gaps) that are responsible for the metal-like conduction inside hexagonal GST. The vacancy disordering process drives the metal-insulator transition via the formation of localized states accompanied with a reduction of carrier mobility. Moreover, XRD measurements reveal that further ion irradiation leads to a conversion from the hexagonal to the rock-salt phase prior to progressive amorphization caused by high ion fluences.

Furthermore, *in-situ* and *ex-situ* measurements were compared and *in-situ* measurements with different ion fluxes were performed both revealing different annealing

behavior of defects for rock-salt and hexagonal GST, respectively. Van der Waals gaps in hexagonal GST serve as preferential sinks for defects to recombine leading to an increased annealing rate compared to the rock-salt phase. A noticeable higher amorphization threshold in hexagonal than rock-salt GST corresponds to a higher resistance against ion beam induced disorder and thus a more stable hexagonal phase.

Thermal annealing of ion irradiated GST thin films revealed reconfigurability of amorphized films, while intermediate states with tailored disorder can be also fully reversed but are stable for temperatures up to $\sim 50^\circ\text{C}$ making tailoring disorder in GST attractive for diverse applications.

Appropriately stacking a thin GST film ($d \approx 40\text{ nm}$) on top of a gold reflector results in near-zero reflection in the near infrared. Further, tailoring disorder inside the initially rock-salt GST film allows for manipulating the point of minimal reflection but also enables arbitrary and precisely tuning the reflectance between low and high values. These gradually tailorable optical properties of GST thin films can be further extended to lateral patterning of confined regions using local ion irradiation via the FIB. This extension will be targeted in the next chapter.

6. Artificial phase coexistence enabled by ion beam patterning

The previous chapter demonstrated in detail that homogeneous ion irradiation can be utilized to tailor disorder in GST thin films. Beyond that, the optical properties of GST can be modified in tightly confined regions by combining ion irradiation with lithographic patterning or direct patterning using a focused ion beam. Thus, a focused ion beam system was utilized to locally irradiate GST films in order to tailor disorder in appropriate regions, which is discussed within this chapter. Through gaining the control over shape and distribution of tailored disorder, new routes for the design of optical devices, such as metasurfaces, become accessible. First, it is demonstrated that an anisotropic metasurface based on a FIB-patterned GST thin film on an Au/Si substrate exhibits dichroism. Second, exploiting the limits of FIB patterning, which are examined via optical nanoimaging techniques, ultimately allows for grayscale patterning at the nanoscale. Transmission electron microscopy measurements were performed in collaboration with Dr. Philipp Schöppe. Optical nanoimaging was carried out at Harvard University by Dr. Yue Luo, Maximilian Zapf, and Maurizio Ritzer. Parts of the results presented in this chapter are published in references [65, 67].

6.1. Dichroism in an anisotropic GST metasurface

A focused ion beam system can be utilized to tailor disorder up to complete amorphization of GST thin films, as already shown in section 5.6.3. The advantage of a FIB versus a large-scale accelerator is obviously the small focal spot of the ion beam. This tightly focused beam (~ 5 nm) readily enables to locally irradiate predefined regions on the nanoscale inside a GST film. Thus, local ion beam-induced amorphization of an initially crystalline GST film results in artificial phase coexistence. Optical functionality can be introduced by obtaining control over the size, shape, and distribution of appropriately designed, amorphized regions.

An initially rock-salt GST film ($d \approx 35$ nm, compare section 5.6.1) was directly patterned in restricted areas of $150 \times 150 \mu\text{m}^2$ using 30 keV Ga^+ -ions and an ion fluence of $6 \times 10^{14} \text{ cm}^{-2}$, i.e., well above the amorphization threshold of such a rock-salt GST film (see section 5.6.3). Various periodic stripe structures were realized with different periods of 10 μm and 250 nm while both have a fill factor of approximately 50% (ratio of irradiated to pristine area), which is schematically depicted in figure 6.1a. The selected

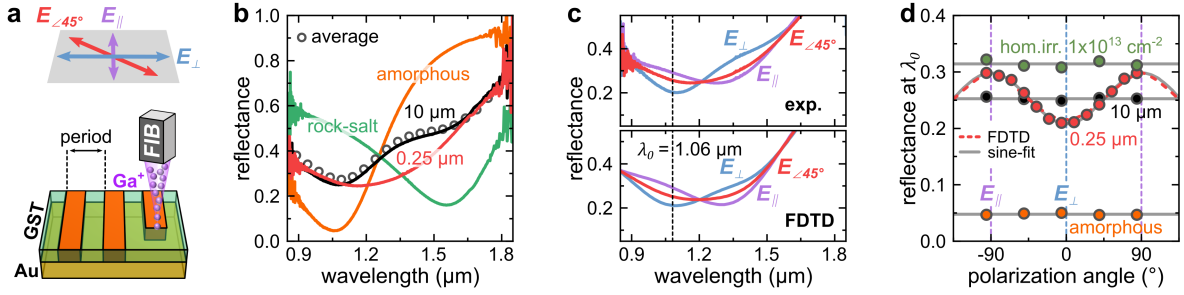


Figure 6.1.: (a) Schematic depiction of local ion irradiation of nanometer-sized stripe patterns in an initially rock-salt GST thin film on Au using a focused Ga^+ -ion beam. (b) Reflectance spectra of irradiated stripe patterns with periods of $10\ \mu\text{m}$ (black) and $250\ \text{nm}$ (red) inside an approximately $35\ \text{nm}$ GST film on Au/Si. For comparison, the spectra of a pristine (rock-salt; green) and a completely irradiated regions (amorphous; orange) are shown, while gray circles represent the average of the reflectance of rock-salt and amorphous GST. (c) Experimental and FDTD simulated, polarization-dependent reflectance spectra of the stripe pattern with the $250\ \text{nm}$ period for light polarized perpendicular (blue), parallel (purple), and at an 45° angle (red) with respect to the stripes. (d) Polarization-dependent reflectance at $\lambda_0 = 1.06\ \mu\text{m}$ as a function of polarization angle for the stripe pattern in (b). Further, the polarization dependence of larger regions, which were either fully amorphized (orange) or in an intermediate state ($1 \times 10^{13}\ \text{cm}^{-2}$, green) is depicted. Solely the small stripe pattern with subwavelength dimension shows a sine-like behavior (gray lines), which matches well with the FDTD simulation (red dashed line).

feature sizes are either significantly above or below the wavelength of near-infrared light. However, the Gaussian ion beam profile of the FIB (see section 3.4.1) and lateral ion beam straggling (compare section 2.1) likely results in a stripe width that exceeds the intended value. Thus, a transition region between amorphous and crystalline GST is inevitable. The intended irradiated width of the $250\ \text{nm}$ stripe pattern was therefore adjusted accordingly as the effect is obviously more pronounced for the smaller stripe pattern. A more detailed examination on the influence of the FIB beam profile and lateral straggling to the effective size of irradiated regions will be presented in section 6.2.2.

Near-infrared reflectance measurements were performed at the regions containing the stripe patterns as well as regions of pristine (rock-salt) and completely amorphized GST. The resulting reflectance spectra are given in figure 6.1b. The spectra of both the rock-salt and amorphous GST region show distinct reflectance minima at $\sim 1.58\ \mu\text{m}$ and $\sim 1.06\ \mu\text{m}$, respectively, caused by thin film interference. The average of the reflectance of rock-salt and amorphous GST (given by gray circles in figure 6.1b) describes well the obtained reflectance spectra of the $10\ \mu\text{m}$ (in period; black line) stripe pattern, which is reasonable for feature sizes much larger than near-IR wavelengths. On the contrary, the reflectance of the smaller stripe pattern with a period of $250\ \text{nm}$ significantly differs and cannot be described by any combination of the reflectance of rock-salt and amorphous GST. Thus, effective optical properties are

observed for this particular stripe pattern with subwavelength dimensions. This can be readily regarded as an anisotropic GST metasurface, which was further confirmed by measuring polarization-dependent reflectance. Figure 6.1c (top) depicts the measured reflectance for different polarizations: electric field vector being either parallel (E_{\parallel}), perpendicular (E_{\perp}), or at an angle of 45° ($E_{\angle 45^{\circ}}$) with respect to the stripes (compare figure 6.1a). Clearly, the reflectance modulates depending on the polarization of light confirming an anisotropic GST metasurface with dichroism, which is the characteristic of some materials to possess different absorption coefficients for differently polarized light. Here, this dichroism is achieved by anisotropically structuring a GST film leading to artificial phase coexistence with subwavelength dimensions.

Furthermore, finite-difference time-domain (FDTD) simulations were carried out in order to describe the effective optical properties of the subwavelength stripe pattern. A simplified FDTD model for the 250 nm stripe pattern consisting of an 110 nm wide amorphized stripe surrounded by 40 nm transition regions embedded in a rock-salt GST film (width of intrinsic region: 60 nm) on Au is assumed using the obtained permittivity values of amorphized ($N_i = 1 \times 10^{14} \text{ cm}^{-2}$) and rock-salt GST, and periodic boundary conditions (see also Appendix A.2). The defective transition region is modeled with the effective permittivity of an intermediate state irradiated with a low ion fluence of $5 \times 10^{12} \text{ cm}^{-2}$ (compare section 5.6.2). The permittivity of the gold substrate was taken from reference [257]. Stripe width values in the FDTD model were optimized by comparing the simulated polarization-dependent reflectance with the measurement, while the reflectance spectra of the optimized FDTD model are given in figure 6.1c (bottom). Note that also the GST film thickness within each region is adjusted according to density differences of each phase [250] (compare section 4.4), while ion beam-induced sputtering is negligible for these ion fluences ($< 1 \text{ nm}$, estimated using SRIM). Already the assumption of a simplified three step model, which does not represent the real gradual permittivity trend, results in reflectance values that resemble well the experimentally obtained spectra. Slight differences in absolute values can be attributed to film morphology, in particular surface roughness, besides the simplifications. Furthermore, neglecting the defective transition region in the FDTD simulation leads to significantly different results that do not match the measured reflectance.

Figure 6.1d shows the reflectance at a fixed wavelength ($\lambda_0 = 1.06 \mu\text{m}$) of both stripe patterns, a homogeneously irradiated intermediate state ($N_i = 1 \times 10^{13} \text{ cm}^{-2}$) and a completely amorphized GST region as a function of polarization angle. Moreover, the predicted reflectance values calculated by FDTD simulations of the subwavelength stripe pattern are given (red dashed line). Both experimental and FDTD calculated reflectance values confirm a sine-like modulation depending on the polarization angle

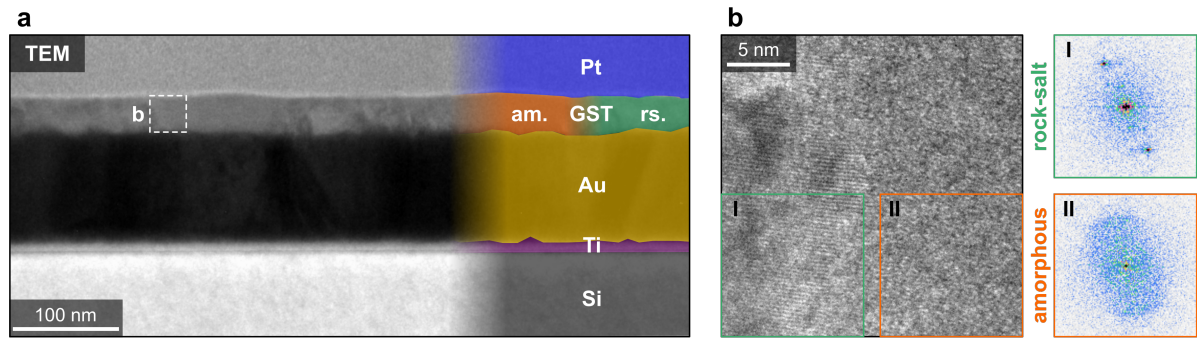


Figure 6.2.: (a) TEM overview image of a cross-sectional lamella taken out of the stripe pattern with a period of 250 nm. (b) High-resolution TEM micrograph taken at a rock-salt amorphous interface. Corresponding FFTs for a respective rock-salt (I) and amorphous (II) area are depicted.

only for the subwavelength stripe pattern. No detectable polarization dependence is observed for completely amorphized and the intermediate GST state, which corroborates the isotropic nature of ion beam induced disorder. Additionally, the 10 μm stripe pattern also do not show a significant polarization dependence despite a small reflectance modulation that is predicted by FDTD. Likely, sample roughness or other measurements uncertainties prevent resolving the small polarization dependence.

Transmission electron microscopy (TEM) measurements were performed on a cross-sectional lamella that was prepared out of the 250 nm stripe pattern in order to investigate the local structure of the different GST regions. Figure 6.2a depicts a TEM overview image of the lamella (thickness ~ 100 nm) revealing the layer sequence of the stack: a GST film on top of a gold layer and the silicon substrate with an additional titanium adhesion layer. Note that the platinum layer at the top was deposited during lamella preparation and, thus, had no influence on the optical measurements, which were performed beforehand. Apparently, differently textured regions can be identified within the GST film. Alternating regions with high and no texture indicate the artificial phase coexistence of rock-salt and amorphous GST. As the pristine rock-salt GST film is polycrystalline, which was confirmed by XRD (compare section 5.6.1), a highly textured appearance in the TEM image is expected. Moreover, these regions seem to be roughly 130 to 150 nm wide. No structure can be identified within the GST film in between the textured regions, which clearly indicates amorphous material. These roughly 100 to 120 nm broad regions show a slight increase in height (density decrease) that further corroborates amorphization caused by the ion beam. Note that defective but yet crystalline GST appears also textured in TEM; thus, pristine and defective, rock-salt regions cannot be easily distinguished. The observed widths of crystalline and amorphized regions agree well with the values anticipated by the FDTD model that was discussed previously.

To confirm the local structure, a high-resolution TEM measurement was performed at a representative interface between a rock-salt and amorphous region. Lattice planes can be identified in the left-hand side of the TEM image in figure 6.2b, while no structure is observed in the right-hand side of the image. A fast Fourier transformation (FFT) of a defined region that contains lattice planes (region I) evidently shows distinct spots corresponding to the detected lattice planes of the rock-salt structure. No such spots can be observed in the FFT of region II confirming amorphization of GST upon FIB irradiation in very confined regions. Yet again, no defective, crystalline regions can be detected in the high-resolution TEM micrograph. However, these regions are necessary to explain the optical response of the subwavelength stripe pattern. Thus, further investigations are necessary to examine the effect of the FIB beam profile in combination with lateral straggling on the local disorder distribution, which is demonstrated in the following sections.

6.2. Spatially resolved phase coexistence via optical nanoimaging

The previous section demonstrated that locally inducing disorder in GST thin films via FIB irradiation can be used to create optical elements. Adding the ability to control not only the size and shape of irradiated regions but also to tailor the optical properties at the nanoscale enables an extra degree of freedom in the design of diverse optical devices [64]. Conventional far-field methods are restricted to probing the effective optical properties while their resolution is diffraction-limited. To circumvent this restriction and in order to resolve the local optical properties of irradiated regions within a GST film, optical nanoimaging techniques, such as photo-induced force microscopy (PiFM) and scattering-type scanning near-field optical microscopy (SNOM), were exploited. Both PiFM and SNOM have the ability to probe the local dielectric function spatially resolved with nanometer resolution while also allowing to simultaneously measure the topography (AFM). The distinct differences of the permittivity between amorphous, rock-salt, and hexagonal GST (compare section 4.4) readily provides the basis of the imaging contrast of PiFM and SNOM, as both measurements probe the local polarizability of a sample surface. The polarizability α is calculated via:

$$\alpha \left(\text{\AA}^3 \right) = \frac{\epsilon - 1}{\epsilon + 2} \times \frac{3 \times 10^{24}}{4\pi n}, \quad (6.1)$$

with the permittivity ϵ and atomic density n . The magnitude and phase of α is given in figure 6.3a for all GST phases, respectively.

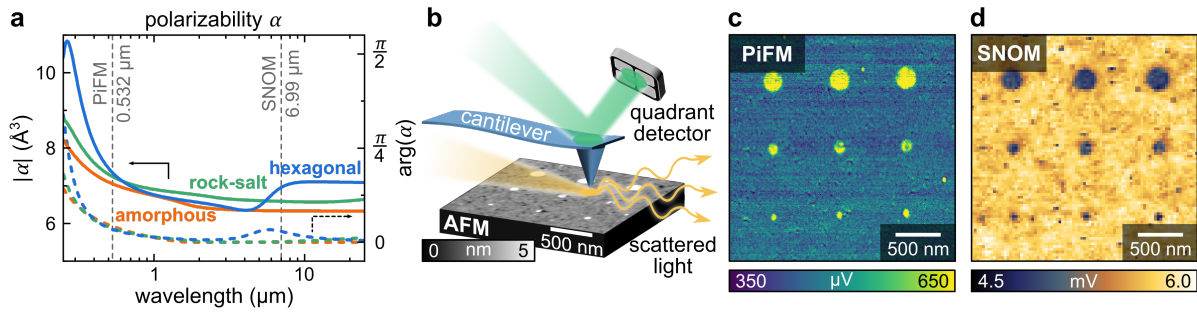


Figure 6.3.: (a) Magnitude $|\alpha|$ and phase $\arg(\alpha)$ of the complex polarizability of the amorphous (orange), rock-salt (green), and hexagonal (blue) GST phase. Dashed lines mark the wavelengths used for PiFM and SNOM measurements. (b) Schematic of the experimental setup for optical nanoimaging. A representative AFM map of FIB irradiated circular regions inside a hexagonal GST thin film is displayed. (c,d) Associated PiFM (c) and SNOM (d) maps of the irradiated pattern from (b).

Optical nanoimaging measurements were performed at two different probing wavelengths: 532 nm for PiFM and 6.993 μm for SNOM (both marked in figure 6.3a). This examination, thus, allows to investigate the effects of FIB irradiation on the optical properties of GST in a broad wavelength range from visible to infrared. While distinct differences are clearly visible, mainly in the magnitude of the polarizability for all GST phases at both probing wavelengths, there is a significantly higher contrast between the hexagonal and the amorphous phase in the infrared in both magnitude and phase compared to rock-salt GST. The latter is a consequence from the large contribution of free carriers (Drude response) to the optical properties of hexagonal GST (compare section 4.4).

Figure 6.3b schematically depicts the experimental setup for optical nanoimaging of FIB irradiated circular regions within a representative 50 nm thick hexagonal GST film on Si. Additionally the AFM topography map of this sample is shown, which reveals already a height contrast between irradiated, amorphized (white) and pristine, hexagonal GST (gray). This height difference is a consequence of swelling of the irradiated regions due to the less dense amorphous phase with respect to hexagonal GST [250]. Moreover, a clear differentiation between hexagonal and amorphous regions is evident in both the PiFM and SNOM map in figure 6.3c and d, respectively. While bright, yellow regions mark irradiated and thus amorphous regions for PiFM, the same areas appear dark in the SNOM map. As the contrast in both methods strongly depends on the experimental conditions (compare section 3.3.2), the fact of opposing contrasts in PiFM and SNOM are irrelevant for this study. Nevertheless, both optical nanoimaging methods clearly show a distinct contrast between irradiated and pristine GST regions and thus enable a further investigation of the limits of FIB irradiation. Therefore, nanoimaging measurements were carried out at several ~ 50 nm thick GST films on Si that were converted to the rock-salt and hexagonal phase, respectively. Various

6. Artificial phase coexistence enabled by ion beam patterning

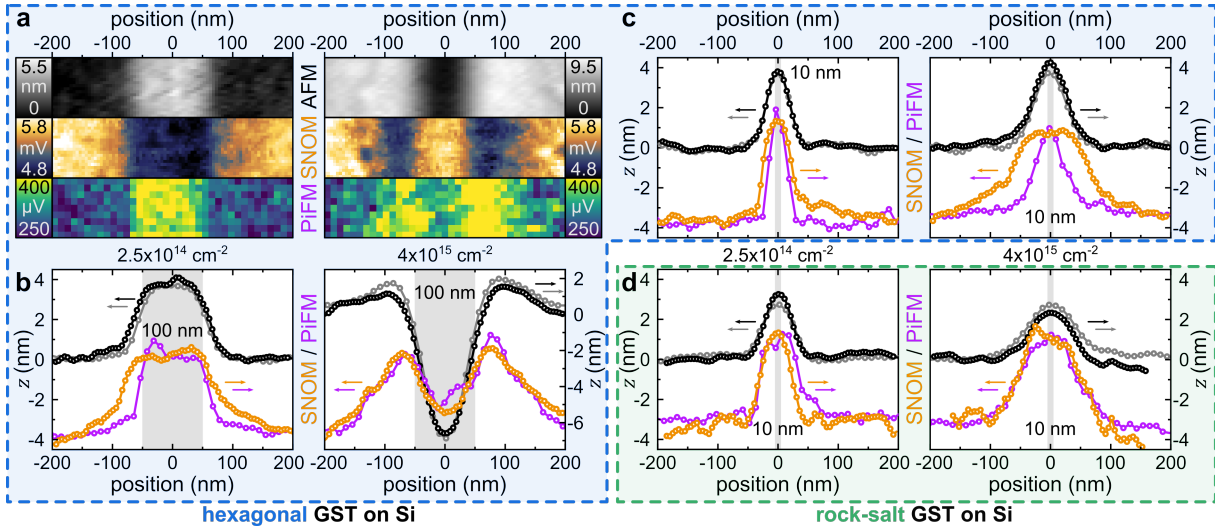


Figure 6.4.: (a) Topography (AFM; measured via SNOM setup), SNOM, and PiFM maps of intended 100 nm wide stripes that were irradiated with an ion fluence of $2.5 \times 10^{14} \text{ cm}^{-2}$ (left) and $4 \times 10^{15} \text{ cm}^{-2}$ (right), respectively, embedded in a hexagonal GST thin film ($d \approx 50 \text{ nm}$) on Si. (b) Corresponding line scans of the topography z (black, gray; measured via SNOM, PiFM setup, respectively), SNOM (orange), and PiFM signal (purple) of the stripes from (a). For comparability, the SNOM signal is inverted in the line scans. (c,d) Line scans of stripes with a predicted width of 10 nm (irradiated with $2.5 \times 10^{14} \text{ cm}^{-2}$ (left) and $4 \times 10^{15} \text{ cm}^{-2}$ (right), respectively) that are embedded in a hexagonal (c) or rock-salt (d) GST thin film on Si.

stripe structures were directly patterned using 30 keV Ga^+ -ions of the FIB at room temperature. To explore the spatial limits of FIB irradiation, the intended stripe width was gradually reduced from 1 μm down to $\sim 10 \text{ nm}$, which is approximately the focal spot size of the FIB.

Representative maps of the topography measured in AFM mode (here using the SNOM setup) together with the SNOM and PiFM amplitude are depicted in figure 6.4a for two exemplary irradiated, 100 nm wide stripes within a hexagonal GST film ($d \approx 50 \text{ nm}$) on Si. All maps reveal a distinct contrast between irradiated and intrinsic regions for the stripe that was irradiated with an ion fluence of $2.5 \times 10^{14} \text{ cm}^{-2}$. However, a trench occurs for a noticeably higher ion fluence ($4 \times 10^{15} \text{ cm}^{-2}$) in the topography map, which is a consequence of ion beam induced sputtering that becomes significant for such high ion fluences. Moreover, within the irradiated regions a reversed contrast is observed in both PiFM and SNOM correlating well with the sputtered trench. As the optical signals are almost completely independent from the topography of the sample, the distinct optical properties within the sputtered region might be a consequence of overall degradation (caused by e.g. preferential sputtering) of the GST film and/or gallium incorporation at this high ion fluence. Note that no PiFM contrast was observed when the excitation laser was switched off corroborating distinguishable optical and topographical signals. Figure 6.4b shows corresponding line

scans of the respective topography, SNOM, and PiFM maps of the two stripes from figure 6.4a. Here, topography line scans are depicted for both measurement setups being in perfect agreement. An increase of film thickness by roughly 4 nm is observed for the stripe irradiated with a fluence of $2.5 \times 10^{14} \text{ cm}^{-2}$. The width of the optical signals correlates well with the swelling of the irradiated regions. Regions outside the predefined irradiation areas are also affected by the FIB with gradually decreasing defect concentrations, which can be clearly observed in all signals due to the Gaussian shaped beam profile of common FIB systems [260] (see also appendix A.2). Increasing the ion fluence to $4 \times 10^{15} \text{ cm}^{-2}$ leads to a broadening of the affected regions with the additional occurrence of the aforementioned sputtered trench. The broadening effect that is a consequence of lateral straggling of the Ga^+ -ions and the FIB beam profile will be discussed in detail in section 6.2.2.

Line scans of significantly smaller stripes with a predefined width of 10 nm are depicted in figure 6.4c using the same ion fluences that were used for the 100 nm stripes (see figure 6.4a,b). Remarkably, no significant sputtering is observed for the higher ion fluence ($4 \times 10^{15} \text{ cm}^{-2}$), thus mainly broadening occurs with increasing ion fluence. The negligible sputtering effect might be a consequence of enhanced redeposition of sputtered atoms. While the optical signals are quite similar in shape and correlate well with the topography of the lower ion fluence ($2.5 \times 10^{14} \text{ cm}^{-2}$), comparing the optical signals of the stripe with higher ion fluence reveals a significantly broader shape in SNOM than in PiFM, which matches well with the findings of chapter 5: As PiFM operates in the visible while SNOM probes infrared light, both methods are sensitive to changes of the optical properties in distinct wavelength ranges. In the previous chapter, it was shown that homogeneous ion irradiation of initially hexagonal GST thin films leads first to a metal-insulator transition accompanied with drastic changes of the permittivity in the infrared. Further irradiation then drives progressive amorphization that leads to different optical properties also in the visible (compare section 5.3.1). Regions outside the predefined areas are also affected by the impinging ions containing gradually decreasing defect concentrations. Low defect concentrations are sufficient to alter the Drude response of hexagonal GST while the permittivity in the visible remains constant as the crystalline matrix is yet unaffected, which in turn leads to a widened SNOM profile compared to PiFM.

For comparison, similar stripes were also irradiated within a rock-salt GST film and their line scans are shown in figure 6.4d. Contrary to the irradiated stripes inside the hexagonal GST film, here, the optical signals of both PiFM and SNOM match well with the topography scans for low and high ion fluences. As rock-salt GST has a negligible Drude contribution in the infrared and only progressive amorphization occurs upon ion bombardment without further electronic or structural transitions, the

optical properties change equally in the visible and infrared depending on the induced disorder. Moreover, the similarity of the PiFM and SNOM scans for irradiated stripes within rock-salt GST further corroborates that the differences in optical signals observed for hexagonal GST are clearly a consequence of various electronic and structural transitions upon increasing disorder.

6.2.1. Gradually tailorable optical properties at the nanoscale

To further investigate the influence of FIB irradiation induced tailored disorder on the local optical properties of GST, multiple stripe structures with different intended widths (w) were irradiated with various ion fluences inside hexagonal and rock-salt GST thin films, respectively. For each stripe and ion fluence AFM, SNOM, and PiFM maps were obtained. First, multiple topography (z) line scans across each stripe were extracted. An exemplary line scan is given in the inset of figure 6.5a together with a fitted modified Gaussian model, which corresponds to:

$$z(x) = \begin{cases} z_0 + \Delta z \exp -((x - x_1)/b)^2 & , x \leq x_1 \\ z_0 + \Delta z & , x_1 < x < x_2 \\ z_0 + \Delta z \exp -((x - x_2)/b)^2 & , x \geq x_2 \end{cases} \quad (6.2)$$

with an arbitrary offset height of pristine GST regions z_0 and the local film thickness change Δz of irradiated with respect to pristine regions. Further, the width of a constant plateau between Gaussian-like transition regions (with standard deviation b) is indicated by x_1 and x_2 . For each intended stripe width and ion fluence, 10 separate line scans were fitted with equation 6.2. The extracted values for Δz of each line scan were averaged and are depicted in figure 6.5a and d as a function of ion fluence for stripes irradiated within a hexagonal and rock-salt GST film, respectively.

For an hexagonal GST film, disorder induced swelling reaches maximal values of about 3 – 5 nm for all stripe widths in an ion fluence range of $1 \times 10^{14} - 1 \times 10^{15} \text{ cm}^{-2}$, which matches well an estimated value Δd for a homogeneously amorphized, initially hexagonal GST film. The penetration depth of the 30 keV Ga^+ -ions was estimated via SRIM to be roughly 40 nm (compare figure 5.11a); thus, the resulting change in film thickness Δd due to the density decrease caused by amorphization of a hexagonal GST film [250] is roughly 3.5 nm. Furthermore, the widest stripe structures ($w = 1 \mu\text{m}$) reveals a gradual increase of Δz that is followed by a strong decrease with increasing ion fluences. The latter is caused by progressive erosion due to ion beam induced sputtering that becomes significant for high ion fluences. Moreover, the sputtering yield for the 30 keV Ga^+ -ions in hexagonal GST films can be again estimated using SRIM and is plotted in figure 6.5a (gray solid line). The strong decrease of Δz for the 1 μm stripes

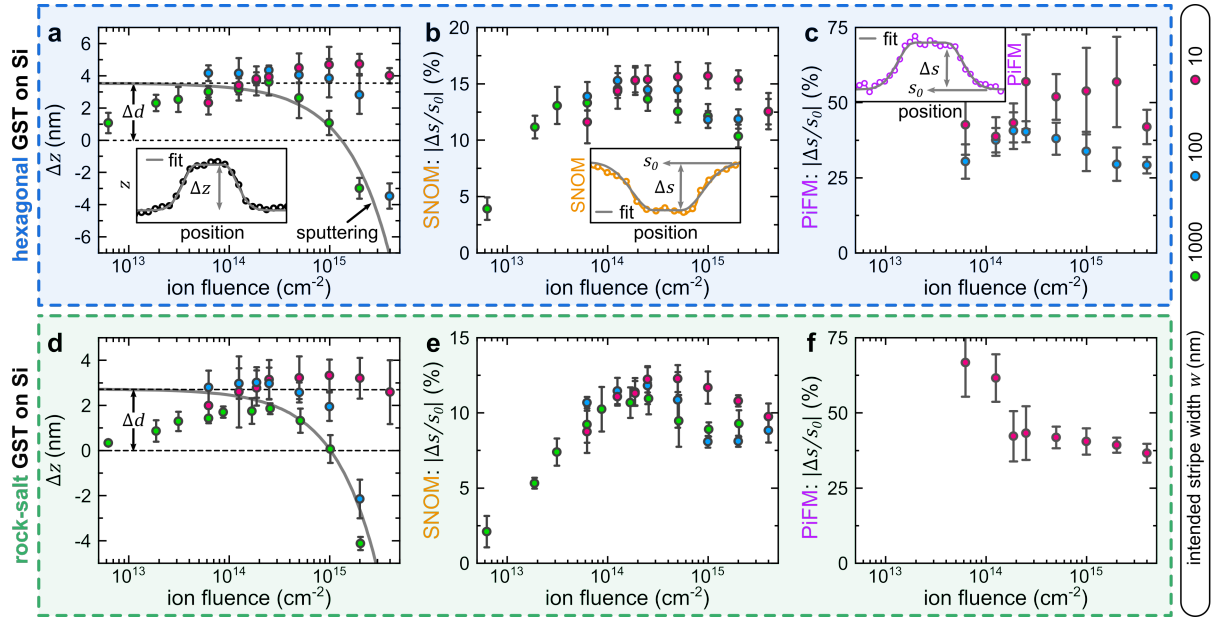


Figure 6.5.: (a,d) Change in film thickness (Δz) and absolute value of the normalized difference of the (b,e) SNOM and (c,f) PiFM amplitude ($|\Delta s/s_0|$) upon irradiation of various stripe structures within initially hexagonal (a-c) and rock-salt (d-f) GST thin films on Si, respectively. Average values and error bars are extracted out of modified Gaussian fits to 10 individual line scans for various stripe widths ranging from 1000 to 10 nm as a function of the ion fluence. The insets in (a) and (b) show representative AFM and SNOM line scans of a 100 nm stripe together with the fits for visualization. Horizontal dashed lines in (a,d) mark the expected film thickness change (Δd) between the crystalline and amorphous film due to their density difference, while gray lines correspond to a decrease of Δz due to ion beam sputtering (calculated via SRIM [81]).

correlates remarkably well with the estimated sputtering yield. The gradual increase for low ion fluences saturates at about $1 \times 10^{14} \text{ cm}^{-2}$ and can be clearly assigned to a disorder-driven structural transition from crystalline to amorphous GST. Moreover, the maximal increase in height of the $1 \mu\text{m}$ stripes matches well with the estimated value Δd for a completely amorphized GST film indicating the amorphization threshold at this respective ion fluence. Reducing the stripe widths leads to a shift of the observed trend towards higher ion fluences. As previously mentioned, redeposition of sputtered atoms and lateral straggling of penetrating ions are responsible for this shift as they have a more significant impact for smaller irradiation areas. Nevertheless, even for such small irradiation areas ion beam induced swelling is observed revealing amorphization of GST on the nanoscale.

Optical nanoimaging was performed on the same stripes from figure 6.5a to probe changes to the local optical properties of locally induced disorder in GST. Again, multiple line scans across each stripe were extracted from the SNOM and PiFM measurements, respectively. As the optical signals follow the trend in topography, they were also fitted with the modified Gaussian model (compare equation 6.2). Exemplary

lines scans of a representative stripe are shown in the insets of figure 6.5b and c for SNOM and PiFM, respectively. For each intended stripe width and ion fluence, the change in optical amplitude Δs between irradiated and pristine GST regions was extracted and averaged for 10 individual line scans. Moreover, Δs was normalized to the optical amplitude of pristine (crystalline) GST regions s_0 as only relative changes in both optical signals are reliable. The normalized change in optical amplitude $|\Delta s/s_0|$ is depicted in figure 6.5b and c for various stripe structures extracted from SNOM and PiFM measurements, respectively. The influence of locally increasing disorder on the optical properties can thus be examined in the infrared and visible spectral region, respectively. The SNOM amplitude change $|\Delta s/s_0|$ gradually increases for the 1 μm stripes and saturates at around $6 \times 10^{13} \text{ cm}^{-2}$, which is significantly below the amorphization threshold obtained from topography measurements. This results from the disorder-driven metal-insulator transition in hexagonal GST that occurs upon ion bombardment for lower ion fluences than the structural transition from crystalline to amorphous (compare section 5.3.1). For ion fluences higher than the amorphization threshold ($\gtrsim 1 \times 10^{14} \text{ cm}^{-2}$), the value of $|\Delta s/s_0|$ slightly decreases indicating again marginally altered local optical properties of amorphous GST due to either overall degradation or Ga incorporation at such high ion fluences. Further, the trend of smaller stripe structures is again shifted towards higher ion fluences.

Unfortunately, PiFM measurements could not be performed on the stripes with an intended width of 1 μm . Additionally, as the ion fluence corresponds to amount of impinging ions per area, lower ion fluences than $6 \times 10^{13} \text{ cm}^{-2}$ are not accessible for the smaller stripe structures due to restrictions of the FIB such as ion beam current and the resulting short irradiation times. Thus, only the change in PiFM amplitude for the 100 nm and 10 nm stripe structures are presented in figure 6.5c. As PiFM probes at visible wavelengths, here, the optical amplitude is more sensitive to the structural transition from hexagonal to amorphous. It appears that saturation is reached for ion fluences in the range of $2 \times 10^{14} - 4 \times 10^{14} \text{ cm}^{-2}$, which thus corroborates the amorphization threshold for the smaller stripe structures observed in the topography measurements.

The same examination of irradiated stripes within a hexagonal GST film was performed for a rock-salt GST film, which is shown in figure 6.5d-f. Similar trends can be observed in the change in film thickness given in figure 6.5d. However, due to a lower density difference between the rock-salt and amorphous phase compared to hexagonal GST, the expected change Δd is significantly smaller ($\sim 2.8 \text{ nm}$), which is again in good agreement with the 1 μm stripes. Comparing the optical signals from the rock-salt GST film with the hexagonal one reveals that indeed the maximal change in SNOM amplitude is observed for significantly higher ion fluences. This further corroborates

the electronic metal-insulator transition in hexagonal GST, which is not present in rock-salt GST. Moreover, the maximal value of the SNOM amplitude difference between amorphous and pristine GST regions is slightly lower for rock-salt compared the hexagonal GST, which matches well with the calculated polarizability of the respective phases (compare figure 6.3). Only the PiFM scans of the smallest stripe structure could be evaluated, as fitting of the 100 nm stripes was not accessible due to a high noise level in these particular measurements. No clear trend can be identified for the 10 nm stripes.

In general these results clearly show that the optical properties of initially crystalline (hexagonal or rock-salt) GST thin films can be controlled locally – at the nanoscale – and tailored gradually by inducing disorder via FIB irradiation. Further, several disorder-driven electronic and structural transitions in hexagonal GST that appear upon ion irradiation (discussed in detail in section 5.3.1) were also observed in confined nanosized regions.

6.2.2. Exploring the spatial limits of locally tailored disorder

The aim of this thesis is to not only to tailor the optical properties locally but also to gain control over the size and shape of irradiated regions within a crystalline GST film. Thus, the spatial limits of FIB irradiation were investigated. Figure 6.6a shows a representative PiFM map of an intended 100 nm wide stripe that was irradiated within a hexagonal GST film with an ion fluence of $1 \times 10^{15} \text{ cm}^{-2}$. The respective line scan is also depicted in figure 6.6a to illustrate the defined total full width at half maximum (FWHM). Using again the modified Gaussian model (equations 6.2) to describe the shape of the optical amplitude, the total FWHM can be described as the sum of the constant plateau between the Gaussian-like edges and their respective half widths at half maximum: $\text{FWHM} = 2\sqrt{\ln 2}b + |x_2 - x_1|$. It is worth noting that $|x_2 - x_1|$ may differ from the intended stripe width w . Nevertheless, an effective broadening of the irradiated regions can thus be calculated as the discrepancy between the total FWHM and the intended stripe width. As the total FWHM is extracted to be $\sim 140 \text{ nm}$ for the representative stripe with $w = 100 \text{ nm}$ in figure 6.6a, this leads to an effective broadening of 40 nm for this respective ion fluence. Such evaluations were performed for various irradiated stripes within hexagonal GST in both SNOM and PiFM measurements, which are depicted in figure 6.6c and d, respectively.

The effective broadening is almost constant for ion fluences up to $5 \times 10^{14} \text{ cm}^{-2}$, an ion fluence that is significantly higher than the amorphization threshold observed in the previous section. However, there is a distinct difference between the observed broadening in SNOM and PiFM measurements. While values of roughly 10 – 20 nm

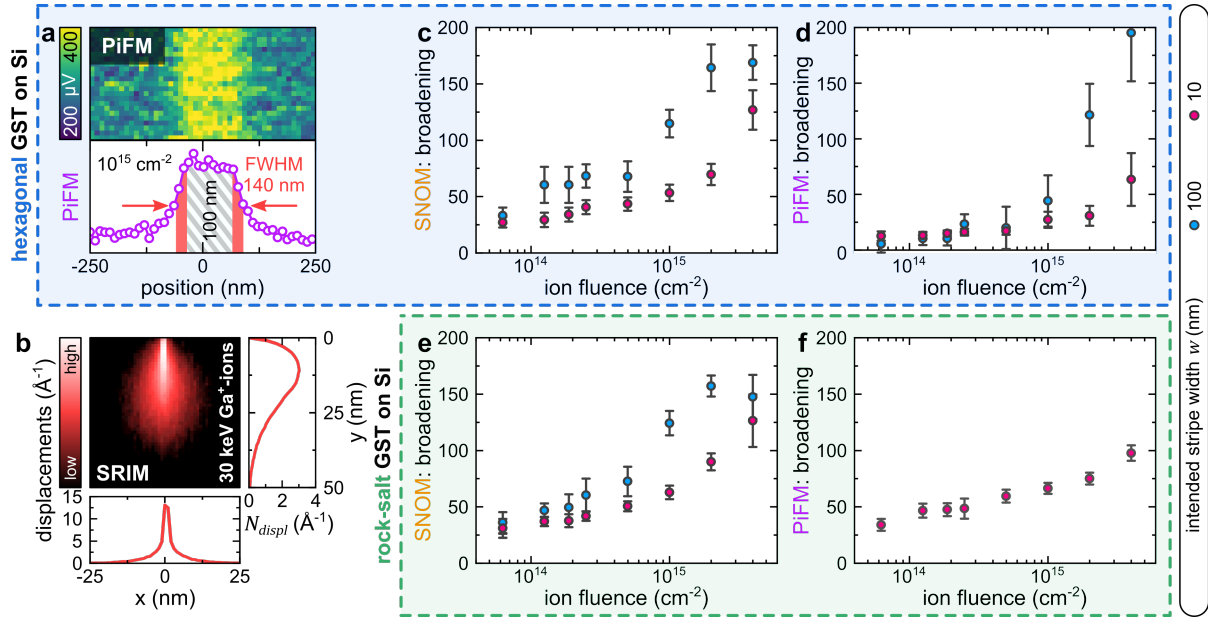


Figure 6.6.: (a) PiFM map and respective line scan of an intentional 100 nm wide stripe (ion fluence: $1 \times 10^{15} \text{ cm}^{-2}$) with an FWHM of roughly 140 nm, leading to an effective broadening of 40 nm. (b) Two dimensional distribution of the total displacements per ion and unit length of 30 keV Ga⁺-ions inside GST (x, y map integrated over z) along with integrations over x (right) and over y (bottom) visualizes the penetration depth and the effect of lateral straggling, respectively. (c-f) Effective broadening as a function of ion fluence extracted out of modified Gaussian fits (10 line scans per value) of the (c,e) SNOM and (d,f) PiFM signal of irradiated stripes within initially hexagonal (c,d) and rock-salt (e,f) GST thin films.

are obtained in PiFM, these values are at least doubled for SNOM. This effect was already discussed previously as it is a consequence of gradually decreasing defect concentrations that lead to different changes to the optical properties in the distinct spectral regions – visible (PiFM) and infrared (SNOM). The latter is caused by vacancy disordering reducing the metallicity of hexagonal GST leading to a decrease of the Drude contribution in the infrared. With increasing ion fluence, the effective broadening increases drastically for all stripe widths, in both SNOM and PiFM, reaching values of up to 200 nm. This effect can be assigned to the beam profile of the FIB (compare appendix A.2), which comprises of two Gaussians and an exponential tail [260]. While the smallest Gaussian with the highest ion flux, called resolution Gaussian, can be focused down to about 5 nm in modern FIB systems, a superimposed second Gaussian (milling Gaussian) is commonly about 50 nm in FWHM containing a two orders of magnitude lower ion flux. Moreover, the exponential tail with 3 orders of magnitude lower ion flux than the resolution Gaussian heavily limits any structure sizes of highly irradiated regions. This is a consequence of induced lattice damage that exceeds the predefined regions. However, for low ion fluences, the FIB beam profile only slightly influences the effective broadening. Here, lateral straggling physically limits

the smallest achievable structure sizes of any irradiated elements. Figure 6.6b illustrates the effect of lateral straggling resulting from nuclear collision cascades of random deflections after a primary knock-on of a Ga^+ -ion in GST. The displacements per unit length and impinging ion were simulated using SRIM, revealing a three-dimensional damage distribution. The lateral distribution of induced displacements can be described by the superposition of a sharp Gaussian that relates to primary knock-ons and a broad Gaussian that corresponds to multiple collisions of deflected ions. While the first one is only about 1 – 2 nm, the second resembles the lateral straggling, which is also responsible for the shifts towards higher ion fluences of the trends for smaller stripe widths.

The same examination was performed for an initially rock-salt GST film, which is shown in figure 6.6e,f. Note that again the PiFM measurements of the intended 100 nm stripes were not evaluated due to the high noise level. The overall trends are very similar to the observations of hexagonal GST. However, all values of the effective broadening are significantly higher for the rock-salt film. This offset results from a disadvantageous focusing of the FIB on the sample's surface in this case. Thus, despite lateral straggling and the FIB beam profile being the basic restrictions for highly confined irradiations, having the sample surface exactly in the focal plane of the FIB is crucial to obtain nanometer sized irradiated regions. Furthermore, the effective broadening observed via SNOM or PiFM is very similar for the rock-salt GST film, which further corroborates the previous findings on the various transitions in hexagonal GST.

In conclusion, the smallest size of any irradiated region within a crystalline GST film is physically limited by lateral straggling for ion fluences below the amorphization threshold assuming ideal positioning of the sample's surface in the FIB focal plane. For high ion fluences, the FIB beam profile leads to amorphization well outside the predefined regions and thus heavily limits any structure sizes. Nevertheless, the FIB beam profile only slightly influences the effective size of irradiated regions within crystalline GST films below their amorphization threshold. In addition to tailoring the local optical properties of GST, this allows to control the size and shape of irradiated regions.

6.3. Grayscale nanopatterning of GST

The ability to gradually tailor the optical properties of GST at the nanoscale readily facilitates its use in a variety of optical applications. As nanosized building blocks of metasurfaces, for instance, are commonly restricted to binary states, adding the ability of grayscale manipulation of such elements enables a novel degree of freedom for

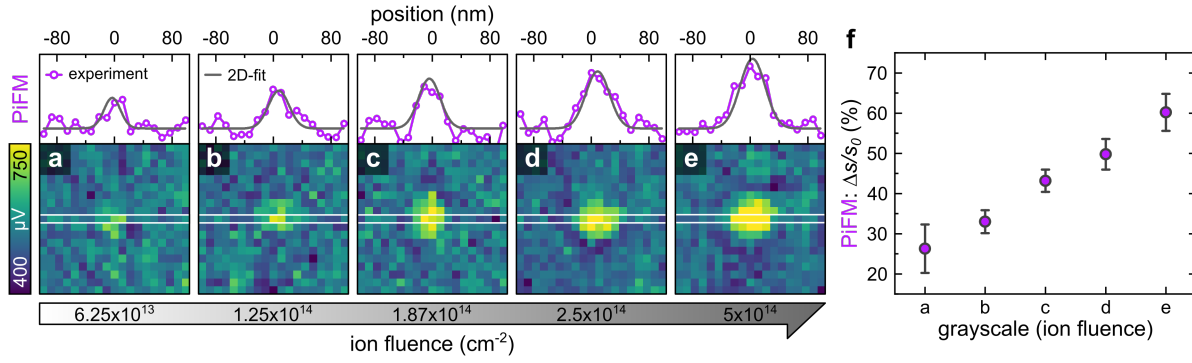


Figure 6.7.: (a-e) PiFM maps of irradiated spots with an intended diameter of 20 nm and increasing ion fluence. Line scans through the center of each spot (purple) are depicted along with an associated line scan of a fitted 2D Gaussian model (gray). (f) Corresponding relative PiFM amplitude change ($\Delta s/s_0$) for each spot showing the potential of grayscale adjustment of the optical properties of GST at the nanoscale.

designing diverse optical devices [64]. To demonstrate this grayscale nanopatterning of GST, small spots with a predefined diameter of 20 nm were irradiated within a hexagonal GST film. The respective measured PiFM maps from multiple spots with increasing ion fluence ($6.25 \times 10^{13} - 5 \times 10^{14}$ cm⁻²) are depicted in figure 6.7a-e. Note that the highest used ion fluence presumably results in amorphization of GST within the irradiated region, which was demonstrated previously. Two-dimensional fits of the PiFM maps were performed for all spots using a 2D Gaussian model. Additionally, line scans of the PiFM amplitude and 2D-fit through the center of each spot are given in figure 6.7a-e indeed revealing a gradually increasing optical contrast between irradiated and pristine GST. While the spot for the lowest ion fluence (6.25×10^{13} cm⁻²) is hardly visible caused by the PiFM noise level, the 2D-fit allows for identifying even this low optical contrast. Furthermore, choosing appropriate ion fluences results in linearly spaced grayscale values of the PiFM difference between irradiated and pristine GST, which are depicted in figure 6.7f as a function of grayscale level. Note that the given values correspond to the PiFM amplitude; thus, they likely do not represent linearly spaced values of the permittivity or refractive index. Moreover, the completely amorphized spot (in figure 6.7e) shows a FWHM of about 40 nm due to the aforementioned broadening effect caused by lateral straggling and the FIB beam profile. As the size of the irradiated spots clearly depends on the applied ion fluence, the intended diameter should be adjusted properly in order to achieve similar spot sized for all grayscale levels. Nevertheless, the ability to gradually tailor the optical properties of GST at the nanoscale with sizes down to 40 nm is evidently demonstrated circumventing the diffraction limit of common laser light sources used for direct laser writing [28, 36].

6.4. Conclusions

Within this chapter, it was demonstrated that local ion irradiation of crystalline GST films using a focused ion beam enables gradually tailored optical properties at the nanoscale. First, periodic amorphous stripe structures were directly patterned into a rock-salt GST thin film on an Au/Si substrate using 30 keV Ga⁺-ions of the FIB leading to an artificial phase coexistence. With structure sizes well below the wavelength of the probing light, the anisotropic pattern behaves like a metasurface with effective optical properties. The resulting optical dichroism was confirmed by FDTD simulations, while the simulation model was based on the findings of cross-sectional TEM investigations. Second, the limits of FIB patterning of intrinsic hexagonal and rock-salt GST films were examined via optical nanoimaging techniques, in particular PiFM and SNOM using visible and infrared probing wavelengths, respectively. While distinct contrasts in both optical signals were observed for irradiated regions within the crystalline films, significant differences occurred for the hexagonal and rock-salt phase. Irradiated regions inside hexagonal GST appear broader in SNOM than in PiFM due to a strong decrease of the Drude response resulting from the metal-insulator transition in hexagonal GST for already small amounts of defects. In contrast, this effect was not observed for rock-salt GST since there is a negligible Drude contribution.

Furthermore, it was shown that any structure size of irradiated regions embedded in crystalline GST is limited physically by lateral straggling and technically by the FIB beam profile assuming an ideally positioned sample in the FIB's focal plane. Moreover, tailoring the amount of induced lattice disorder ultimately enables grayscale patterning at the nanoscale. By this means, grayscale elements comprising irradiated spots with diameters of about 40 nm within a hexagonal GST thin film were fabricated. These nanosized grayscale elements can in principle act as a multilevel storage system [55]. By appropriately adjusting the induced ion fluence at least 8 distinct optical grayscale levels become accessible corresponding to a 3 bit system. Thus, high storage densities beyond 300 Gbit/in² can be achieved considering a square arrangement of the 8-level spots with sizes below 80 nm, which corresponds to double the spot size (~ 40 nm). Moreover, the grayscale elements remarkably demonstrate that the optical properties of GST can be gradually tailored with sizes well below the diffraction limit of common direct laser writing [28, 36]. Furthermore, through gaining the control over the shape and distribution of tailored disorder, new routes for the design of optical devices, such as metasurfaces, become accessible.

7. Ion beam impurity doping of GST for active optical devices

While the previous chapters focused on tailoring disorder in GST via ion irradiation, the effect on the optical properties of impurities, in particular Ga^+ -ions from the FIB, was considered disadvantageous. However, impurity doping with a variety of elements has been demonstrated to effectively alter the crystallization kinetics of GST [169, 177–183, 185–189]. As doping during deposition is commonly used for increasing the phase stability in PCRAM applications [170–176], spatially selective doping of GST based on ion implantation through lithographically patterned masks yields the ability to shift the critical temperature T_C for crystallization in restricted regions. Artificial phase coexistence can thus be achieved upon heating, which readily facilitates its use in active optical devices. This chapter reports on ion beam impurity doping of GST thin films in order to modify the phase-change from amorphous to rock-salt phase. First, the impact of noble gas irradiation on as-deposited amorphous GST is investigated to differentiate the effects of impurity doping and defects. Second, multiple GST films were implanted with various group V elements in order to examine the mechanism that is responsible for the shift in T_C , in particular the contributions from lattice strain or electronic doping. Finally, spatially selective ion beam doping using lithographic masking is demonstrated. Measurements of diverse amorphous phases and impurity doping of group V elements were performed in collaboration with Robin Schock (see his master thesis [68]). The implantation of box-like profiles and measurements on area-selectively implanted GST were carried out together with Jacob Grandmontagne (see his bachelor thesis [69]).

7.1. Polymorphism of amorphous GST

Noble gas ion irradiation was performed on as-deposited, amorphous GST thin films in order to investigate the impact of induced defects on the crystallization kinetics separate from any chemical effect. Thus, multiple as-deposited GST films ($d \approx 100$ nm) on Si were irradiated with 55 keV Ar^+ -ions with various ion fluences. The reflectance spectra obtained for each sample are depicted in figure 7.1a revealing unaffected optical properties of irradiated GST for ion fluences below $1 \times 10^{15} \text{ cm}^{-2}$. However, while minor variations can be observed for fluences of $5 \times 10^{15} \text{ cm}^{-2}$ and $1 \times 10^{16} \text{ cm}^{-2}$, a strong decrease in reflectance in the near-IR can be observed for $3 \times 10^{16} \text{ cm}^{-2}$ and

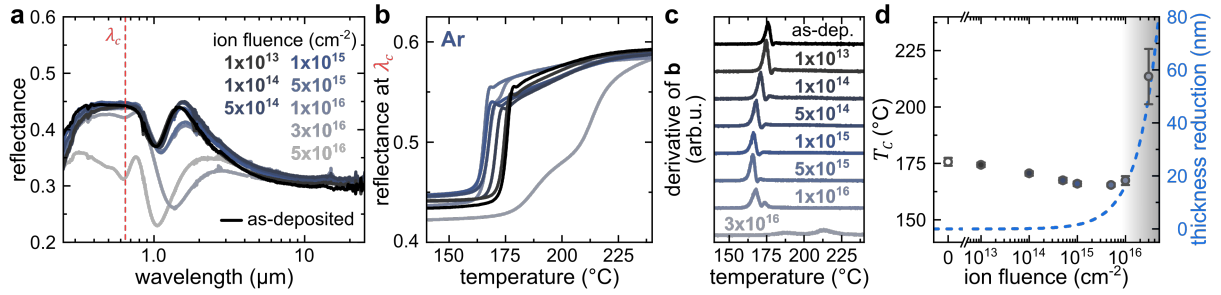


Figure 7.1.: (a) Reflectance spectra of intrinsic and irradiated amorphous (as-deposited) GST films ($d \approx 100$ nm) on Si, which were irradiated with 55 keV Ar^+ -ions and various ion fluences. (b) Reflectance at a wavelength of $\lambda_c = 635$ nm of the as-deposited and irradiated films from (a) during heating (heating rate 20 K/min). (c) Derivative of the reflectance change as a function of temperature. (d) (left scale) Critical temperatures for crystallization as a function of ion fluence. Error bars correspond to the full-width at half maximum of the first derivatives shown in (c). (right scale) GST film thickness reduction caused by ion beam sputtering (estimated via SRIM). Gray shaded area marks regime of strong film degradation caused by preferential sputtering.

additionally in the visible for $5 \times 10^{16} \text{ cm}^{-2}$. These strong decreases can be attributed to thinning of the GST films caused by significant ion beam induced sputtering. Sputtering yields for each atomic species were estimated using SRIM to be 0.81, 1.02, and 3.32 atoms/ion for Ge, Sb, and Te, respectively, for the given implantation parameters. Taking into account the initial stoichiometry of GST ($\text{Ge}_2\text{Sb}_2\text{Te}_5$: 1 : 1 : 2.5) reveals preferential sputtering of the heavier elements – Sb and Te – leading to a Ge enrichment at the surface [217]. This variation in composition together with a significant film thickness reduction (see figure 7.1d) causes the change in reflectance for such high ion fluences.

The crystallization kinetics of the conversion from amorphous to rock-salt of these samples were investigated using temperature-resolved reflectance (TRR) measurements, as presented in figure 7.1b. Here, absolute values were calculated using the measured reflectance values at $\lambda_c = 635$ nm of the samples before heating. Moreover, first order derivatives of $R(T)$ are depicted in figure 7.1c. Clearly, Ar^+ -ion irradiation leads to a gradual decrease of the critical temperature for crystallization T_C with increasing ion fluence (see also figure 7.1d). However, for the highly irradiated film with $N_i = 3 \times 10^{16} \text{ cm}^{-2}$ a strong increase of T_C is observed accompanied with a very broad transition. Note that no transition was observed for the film with the highest ion fluence ($N_i = 5 \times 10^{16} \text{ cm}^{-2}$; not shown). The thickness reduction caused by ion beam sputtering was estimated via SRIM and is given in figure 7.1d. The estimation reveals a film thickness reduction of ~ 50 nm for the GST film irradiated with $3 \times 10^{16} \text{ cm}^{-2}$ leading to the Ge enrichment. Actually, Ge-rich GST compounds were found to possess an increased stability of the amorphous phase [261, 262].

The shift in T_C observed for the lower ion fluences can be attributed to the altered short-range order in the amorphous GST phase upon ion irradiation. It is reported that the as-deposited amorphous phase comprises Ge that is partially three-fold coordinated in defective octahedra while $\sim 30\%$ is tetrahedrally coordinated (compare section 2.3.1) [114]. The accompanied homopolar Ge-Ge and Te-Te (so called "wrong") bonds, that are only present in the amorphous phase and not observed for crystalline GST, thus inhibit the crystallization process of GST [116]. Reports on EXAFS¹ and Raman spectroscopy of amorphous GST revealed a reduction in the amount of homopolar bonds upon ion irradiation leading to the enhanced crystallization kinetics, i.e., a decrease of T_C [209]. Moreover, the local bond rearrangement that is caused by the atomic mobility induced by the ion collision cascade results in an altered short-range order. This might be accompanied with slightly different optical properties of irradiated GST compared to as-deposited GST that was also observed in sections 5.3.1, 5.3.3, and 5.6.2.

Nevertheless, ion irradiation of as-deposited, amorphous GST thin films leads to a decrease of T_C before ion beam sputtering leads to a significant Ge-enrichment accompanied with off-stoichiometric GST. The enhanced crystallization kinetics are a consequence of reduced homopolar bonds upon ion bombardment. Both effects has to be considered in the next sections where impurity doping of GST films is discussed.

7.2. Impurity doping with group V elements

There are a variety of elements that are proposed in literature to effectively manipulate the crystallization process of phase-change materials (compare section 2.3.5). Among many others, nitrogen doping of GST was found to increase the amorphous phase stability, i.e., increasing the crystallization temperature T_C . While doping of GST is commonly achieved during film growth, ion implantation was also demonstrated to modify the crystallization process (see also section 2.3.5). However, the underlying mechanism that inhibits the phase-change from amorphous to rock-salt in doped GST is still a matter of debate and clearly depends on the doping element.

7.2.1. Manipulating the crystallization process in GST

Multiple as-deposited (amorphous; $d \approx 100$ nm) GST thin films on Si were irradiated with N^+ , P^+ , As^+ , Sb^+ , and Bi^+ -ions using various ion fluences. Respective ion energies and fluences were selected in order to achieve a projected range centered in the middle of the GST film ($R_p \approx 50$ nm) and comparable peak concentrations ranging

¹Extended X-ray absorption fine structure

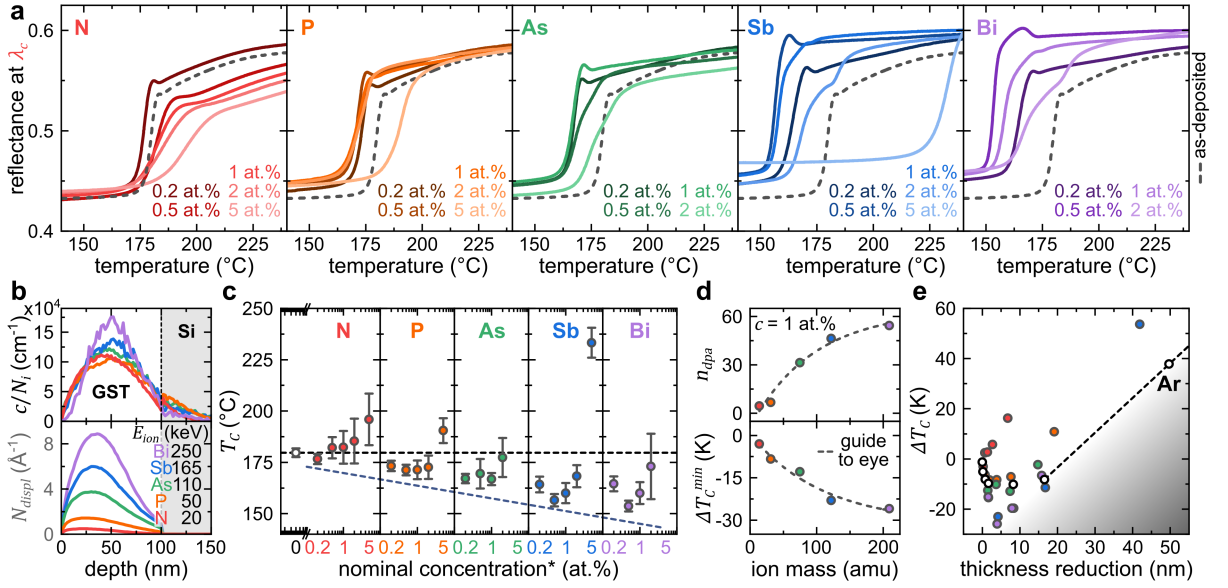


Figure 7.2.: (a) Reflectance at $\lambda_c = 635$ nm of various group V ion implanted GST films on Si ($d \approx 100$ nm) during heating (heating rate 25 K/min). Additionally, a representative TRR curve of a comparable as-deposited GST film is depicted (dashed lines). (b) Ion concentration normalized to ion fluence c/N_i (top) and total displacements per incident ion N_{displ} (bottom) as a function of depth as simulated with SRIM for each ion species from (a) at 7° incidence angle. (c) Critical temperatures for crystallization T_C as a function of nominal dopant concentration for all ion species. Nominal concentration values correspond to peak values of (b); however, the actual concentration distribution may differ, which is caused by a film thickness reduction (sputtering). Error bars display the full-width at half maximum of the first derivatives of the respective TRR curve. (d) The number of displacements per atom n_{dpa} (calculated with peak values of N_{displ} from (b)) for a nominal dopant concentration of 1 at.% is compared to the difference in critical temperature ΔT_C^{min} of the lowest obtained T_C as a function of ion mass. (e) Change in critical temperature ΔT_C as a function of film thickness reduction caused by ion beam sputtering of GST. Additionally, the values of argon irradiated GST films are shown to separate the effect of doping.

from 0.2 at.% to 5 at.% for all ion species, respectively, which was estimated using SRIM simulations, as shown in figure 7.2b. All samples were annealed to 250 °C using the TRR setup subsequent to ion implantation allowing to monitor the phase-change from amorphous to rock-salt. Figure 7.2a depicts the reflectance at $\lambda_c = 635$ nm upon heating (constant heating rate of 25 K/min) for all ion species and nominal peak concentrations as a function of temperature. Additionally, the reflectance change of a comparable intrinsic, as-deposited GST film is shown as dashed lines in figure 7.2a. Indeed, ion implantation significantly influences the crystallization process of GST thin films.

Further insights can be obtained by determining the crystallization temperature T_C that is again defined as the maximum of the first order derivative of the TRR curve (not shown here). The extracted T_C values are depicted for all ion species and nominal

concentrations in figure 7.2c. Note that nominal concentration is marked with an asterisk, as these values correspond to the peak concentration estimated via SRIM. However, as previously demonstrated (compare figure 7.1d), ion irradiation with high ion fluences leads to a significant thickness reduction due to sputtering accompanied with a flattened ion distribution profile that is not considered in the SRIM simulation. Thus, the resulting peak concentrations are likely lower than expected, in particular, for higher ion fluences and heavy masses.

Besides a small decrease for 0.2 at.%, N doping leads to a gradual increase of T_C . While the first decrease can be attributed to ion irradiation induced defects accompanied with a reduction of homopolar (Ge-Ge, Te-Te) bonds in amorphous GST enhancing the crystallization kinetics (discussed in section 7.1), the following increase with increasing N content indicates a clear effect of impurity doping.

Similar trends can be identified for all other ion species investigated. Additionally, with increasing concentration the transitions become broader for all ion species, which is represented by the error bars in figure 7.2c. This may be attributed to the heterogeneous doping profiles for all elements. However, the first decrease of T_C is more pronounced for heavier ions; figure 7.2d depicts the difference in T_C for the lowest obtained T_C compared to the intrinsic case (denoted ΔT_C^{min}) as a function of ion mass. Evidently, ΔT_C^{min} decreases with increasing ion mass. Moreover, the estimated number of displacements per atom n_{dpa} is also shown as a function of ion mass for a peak concentration of 1 at.% of the respective element. Indeed, both curves follow a similar trend with inverse slopes (indicated by the dashed line in figure 7.2d). With increasing ion mass, n_{dpa} increases drastically for the same nominal concentration (compare also N_{displ} in figure 7.2b). Thus, heavier ions induce more defects for the same peak concentration likely accompanied with a higher reduction of homopolar bonds in amorphous GST, which leads to the more pronounced decrease of T_C compared to lighter ions.

A significant increase of T_C is observed for nominal concentrations above 1 at.% for all group V elements (see 7.2c). However, the effect of preferential sputtering accompanied with a GST film degradation needs to be considered, in particular, for the higher concentrations in order to confirm that the shift in T_C is caused by impurity doping. Thus, figure 7.2e shows the difference in critical temperature ΔT_C for all ion species as a function of film thickness reduction (Δd) caused by ion beam sputtering. Additionally, the values of Ar irradiated (as-deposited) GST films are depicted. As no doping effect is expected for noble gas irradiation, it was concluded in section 7.1 that the strong increase in T_C is correlated to off-stoichiometric GST (Ge-enriched) caused by preferential sputtering. Such effect shows the same tendency like what is expected from impurity doping of GST, i.e., an increase of T_C . Despite that the increase of T_C for very high concentrations of all group V elements might be a superposition of impurity

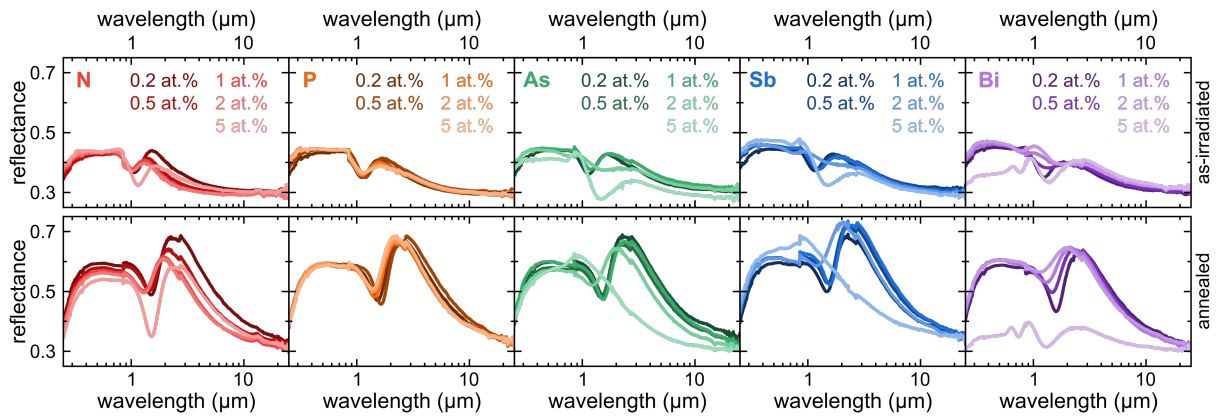


Figure 7.3.: Reflectance spectra of various group V ion implanted GST films ($d \approx 100$ nm) on Si. While spectra of the films in the as-irradiated state are displayed in the upper row, the lower row shows the spectra subsequently to a thermal annealing step up to 250 °C of the samples.

doping and Ge-enrichment, all values of ΔT_C are significantly above the dashed line in figure 7.2e that connects ΔT_C of Ar irradiated GST films with fluences of $1 \times 10^{16} \text{ cm}^{-2}$ ($\Delta d \approx 15$ nm) and $3 \times 10^{16} \text{ cm}^{-2}$ ($\Delta d \approx 50$ nm). As this simple assumption does not represent the real effect, it mainly resembles its upper limit. Thus, a further increase can be clearly correlated to impurity doping.

The increase of T_C upon doping with various elements was frequently demonstrated [212, 216, 217], while two models emerged to explain the effect of increased stability of the amorphous phase in doped GST [170, 182]. The first model proposes an induced strain field for light doping elements. For instance, N has an atomic radius of 0.65 Å, which is well below the radii of Ge, Sb, and Te (1.25 Å, 1.45 Å, and 1.40 Å) [263]. Thus, it is unlikely that N substitutes atoms from their lattice sites and preferably locates at tetrahedral interstitial sites. This leads to a distortion of the lattice accompanied with an induced strain field, which retards the crystallization process. On the other hand, the second model proposes that chemical bonds might change from a metallic mode towards a dielectric mode caused by increased amount of covalent bonds. The latter might be more applicable for heavier elements as they may substitute lattice atoms and form more covalent bonds, which is facilitated by similar electronegativity values of P (2.19), As (2.18), Sb (2.05), and Bi (2.02) compared to Ge (2.01), Sb, and Te (2.02). This might be further corroborated considering the implantation of Sb. While Sb is already an element of GST, it can be easily built into the matrix by, for instance, filling the inherent vacancies of GST. However, Sb shows also a significant effect on the crystallization process, which has also been reported by others [264]. Thus, the formation of additional covalent bonds likely causes the reduced atomic diffusivity that inhibits the crystallization process at least for the heavier dopants.

Figure 7.3 depicts the reflectance spectra of all group V doped GST thin films in the as-irradiated and annealed state, respectively, to evaluate the effect of doping on the optical properties of GST. Note, no TRR curve is shown for the 5 at.% As-doped GST film in figure 7.2a (technical issue), the spectra of this sample are depicted in figure 7.3. While negligible changes of the reflectance are observed for P-doped GST up to 5 at.%, N doping leads to a slight decrease of the reflectance of annealed (rock-salt) GST in the visible region, which was also found in the TRR curves (see figure 7.2a). However, heavier elements tend to have a more pronounced impact on the optical properties of GST. While small variations of the reflectance of both the amorphous and rock-salt phase are detected for 2 at.% As, Sb, and Bi content, respectively, doping with 5 at.% severely changes the optical properties of GST. This effect is most apparent for Bi doping, where no phase-change is observed for annealing the sample with 5 at.% Bi content to 250 °C and the reflectance differs drastically to GST films with lower Bi contents. The enhanced impact of heavier ions on the optical properties can be either related to the increased amount of induced lattice damage or to the higher sputtering yields, i.e., more pronounced preferential sputtering. Moreover, the significant incorporation of impurities, that was proposed before, might also impact the optical properties. However, as N doping leads also to a gradual decrease of the reflectance of rock-salt GST and, here, lattice damage and sputtering are very low, the induced strain field might also affect the optical properties of GST, in particular distorting the rock-salt structure.

7.2.2. Reconfigurability of doped GST films

Repeated switching between amorphous and crystalline states was performed on the group V implanted GST films to further demonstrate the applicability of impurity doping of GST for optical devices. Therefore, all samples were irradiated with 55 keV Ar⁺-ions and an ion fluence of $N_i = 7 \times 10^{14} \text{ cm}^{-2}$ after the first annealing step that was discussed in the previous section. It was demonstrated in chapter 5 that such an irradiation leads to complete amorphization of initially rock-salt GST thin films.

Repeated re-amorphization and annealing to 250 °C for the conversion to the rock-salt phase were conducted for all group V implanted GST films and are depicted in figure 7.4a-e. In the case of N doping, there is a drastic decrease of T_C upon cycling, whereas the largest effect occurs after the first re-amorphization step. This is caused by an overall decrease of T_C due to the induced lattice damage of Ar irradiation that facilitates the crystallization process. Additionally, T_C of a comparable intrinsic GST film that was also cycled is shown for all ion species in figure 7.4a-e to visualize this effect (compare also section 5.5.1). Only the highest N-doped sample shows a slightly

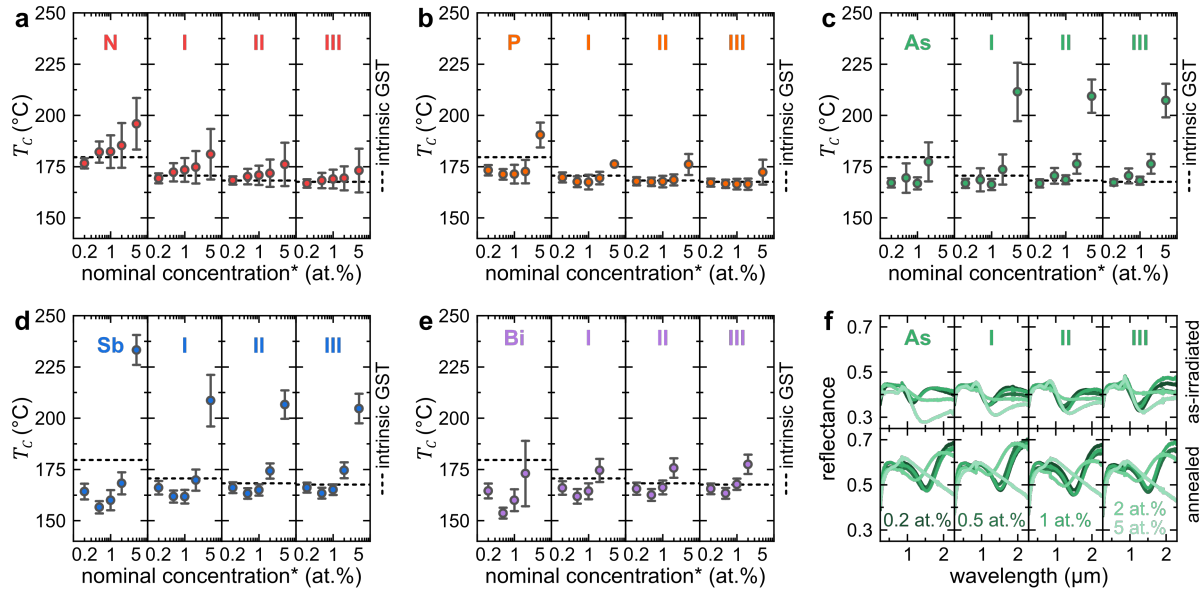


Figure 7.4.: (a-e) Critical temperatures for crystallization T_C of multiple, implanted GST films on Si as a function of nominal dopant concentration for all ion species. Subsequent to the first annealing step, each sample was repeatedly irradiated with 55 keV Ar^+ -ions (above the amorphization threshold; $N_i = 7 \times 10^{14} \text{ cm}^{-2}$) followed by additional annealing steps (I to III). Error bars correspond to the full-width at half maximum of the first derivatives of the respective TRR curve. Dashed lines display T_C values of a comparable intrinsic (non-implanted) GST film that was also cycled accordingly. (f) Reflectance spectra of the As^+ -ion implanted GST films. The upper row depicts the reflectance after As implantation and each re-amorphization step (I-III), while the reflectance after each annealing step (heating to 250 °C) is displayed in the lower row.

increased T_C after 3 cycles, while no shift is present for GST films with a N content below 2 at.% (compared to the intrinsic yet cycled GST film). Thus, the overall N content that contributes to impurity doping effects decreases drastically upon multiple cycles of re-amorphization and annealing. Ion irradiation might cause displacements of N that can then form volatile N_2 . Upon annealing, N_2 might be able to diffuse out and, therefore, does not contribute to impurity doping anymore and thus T_C is the same as for the non-implanted films.

A similar trend can be observed for P-doped GST films in figure 7.4b. Here, the formation of P molecules is unlikely. However, as P is much lighter compared to Ge, Sb, and Te, it might also diffuse out of the sample at elevated temperatures and/or agglomerate at, for instance, grain boundaries or interfaces. This would lead to a reduction of the strain field, which would again facilitate the crystallization process.

On the other hand, heavier ions show opposite effects. The shift towards lower crystallization temperatures for low doping concentrations reduces upon cycling, while being most pronounced for Bi doping (see figure 7.4e). After the first annealing step most of the induced lattice damage might be restored. Re-amorphization with Ar irradiation

causes again a reduction of homopolar bonds, but to a smaller extent compared to the heavier Bi. Thus, the shift of T_C caused by damage approaches the value of intrinsic GST. Furthermore, T_C also decreases within the doping regime for high concentrations of As and Sb upon cycling. Moreover, while Sb and As both show similar trends, As exhibits a slightly higher T_C for the 5 at.% doped sample; thus, for subsequent experiments in the next section As was chosen as it is a good compromise between doping effect and induced lattice damage. Figure 7.4f depicts the reflectance of both the as-irradiated and annealed state of the various As-doped GST films upon cycling. No significant change is observed for multiple re-amorphization and annealing steps. Actually, this behavior was observed for all group V elements.

7.3. Spatially selective impurity doping – proof of concept

If it is possible to achieve well separated phase transitions of intrinsic and doped GST, spatially selective impurity doping would readily facilitate the design of optical devices that are based on artificial phase coexistence within GST films. As the changes in crystallization temperature are stable upon multiple cycles of re-amorphization and crystallization, this would further allow for active in and out tuning of the phase coexistence, i.e., the optical response of the device. Thus, within this section spatially selective impurity doping of GST films is investigated.

Before laterally varying doping concentrations within a GST film are fabricated, the doping effect of As should be enhanced via the introduction of a more uniform implantation profile. Therefore, multiple ion irradiations with varying ion energy (30 keV, 140 keV, and 180 keV) were performed on GST films on Si. Appropriately choosing the ion fluence for each energy results in box-like implantation and doping profiles (values given in appendix A.1), which are depicted for various As concentrations in figure 7.5a. The reflectance spectra on as-implanted (with As box-profile) and annealed (to 250 °C) GST films are depicted in figure 7.5b. Already doping with 0.2 at.% As leads to a significant change of the reflectance mainly in the near-IR spectral region. Here, oscillations that are present in the intrinsic case caused by thin film interference vanish. This is likely a consequence of the doping profile as a significant amount of As extends well into the Si substrate for the used ion energies (140 keV and 180 keV), which leads to a significant interface mixing [82]. Thus, the softening of the interface leads to the decrease of the interference fringes. For higher concentrations new fringes occur that cannot be explained only by a film thickness reduction, i.e., a shift of the interference fringes of as-deposited GST. Moreover, they become more pronounced

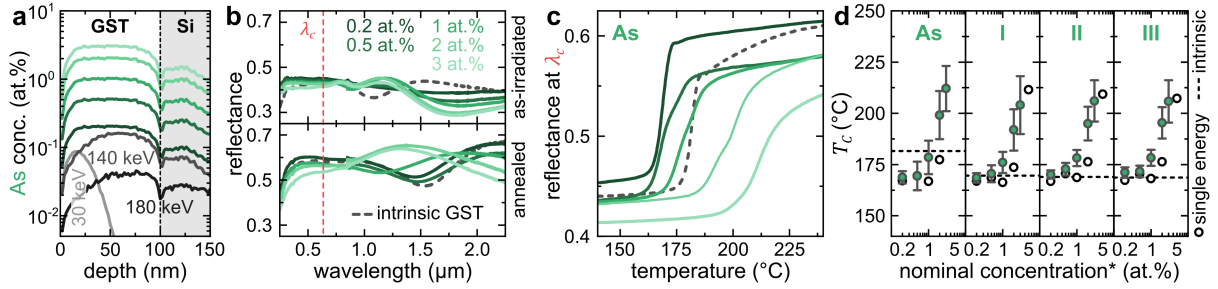


Figure 7.5.: (a) Sum As concentration profiles (green) within a 100 nm GST film on Si for multiple ion fluences calculated via SRIM at 7° incidence angle. Additionally, single energy profiles are depicted only for the lowest sum concentration (0.2 at.%). (b) Reflectance spectra of the box-like As^+ -ion implanted GST films in the as-irradiated (120 keV Ar^+ -ions, $N_i = 7 \times 10^{14} \text{ cm}^{-2}$; top) and annealed (after heating to 250°C ; bottom) state. The reflectance of an intrinsic is also depicted for comparison. (c) Reflectance at $\lambda_c = 635 \text{ nm}$ of the as-deposited and implanted films from (b) during heating (heating rate 25 K/min). (d) Critical temperatures for crystallization T_C of samples from (b) as a function of nominal As concentration. Subsequent to the first annealing step, each sample was repeatedly amorphized followed by additional annealing steps (I to III).

with increasing As content, while their positions remains constant despite a significant film thickness reduction ($\sim 30 \text{ nm}$ for 3 at.%). This further corroborates that interface mixing is occurring. However, these effects observed for the as-irradiated states were not detected in the reflectance spectra of annealed As-doped GST. Here, a clear contribution of thin-film interference can be detected that clearly depends on the reduced film thickness. Moreover, the lower As concentrations match well with the intrinsic (rock-salt) GST film, which might indicates a reconstruction of the interface due to the atomic mobility upon thermal annealing.

Nevertheless, there is still a distinct difference of the optical properties between amorphous and crystalline As-doped GST, which can be further observed in the TRR curves that are depicted in figure 7.5c. At visible wavelengths (here 635 nm) the reflectance in both amorphous and crystalline phases decreases for higher As concentrations. However, there is a gradual increase of the crystallization temperature T_C with increasing As content after a first decrease due to ion beam induced lattice damage. Figure 7.5d shows T_C for box-profile As-doped GST films upon repeated cycles of re-amorphization and annealing. Additionally, the values of single energy implants (compare figure 7.4) are given for comparison. Indeed, uniform ion implantation enhances the doping effect of As compared to the single energy implant, which is attributed to the increased integral As concentration within the GST film. Already the implantation of 2 at.% As leads to an increase of T_C to $\sim 195^\circ\text{C}$ (after cycle III); thus, the transitions of intrinsic yet cycled and implanted GST are well separated, which readily enables the envisioned in and out tuning of phase coexistence for spatially selective doped GST films.

An as-deposited GST film ($d \approx 100 \text{ nm}$) on Si was covered with a lithographic mask

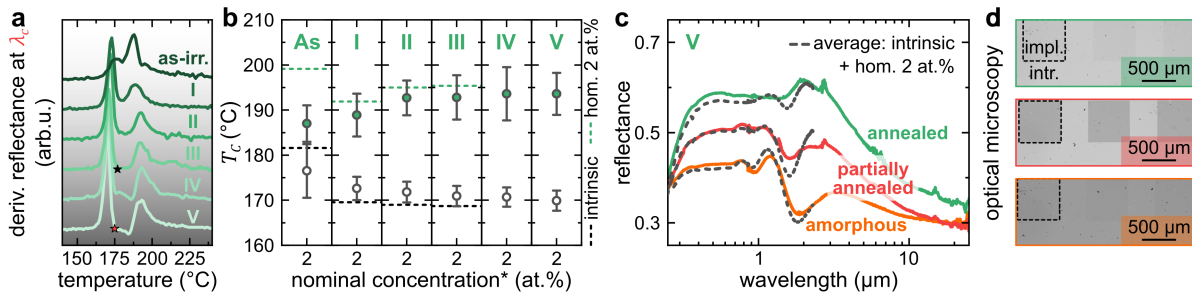


Figure 7.6.: (a) Derivative of the reflectance at $\lambda = 635$ nm as a function of temperature for the area-selectively As⁺-ion implanted GST film in the as-irradiated state and after various re-amorphization steps (I to V; 120 keV Ar⁺-ions, $N_i = 7 \times 10^{14} \text{ cm}^{-2}$). Stars mark the cycles and corresponding temperatures at which heating was interrupted to obtain lateral phase coexistence. (b) Critical temperatures T_C of samples from (a) for the crystallization of intrinsic (white) and implanted (green) regions. Dashed lines display T_C values of a comparable intrinsic and homogeneously implanted (with 2 at.%) GST film that were also cycled accordingly. (c) Reflectance spectra of the area-selectively implanted GST film in the amorphous (Ar irradiated; orange), partially annealed (to ~ 175 °C; red) and completely annealed (to 250 °C; green) states taken in cycle V. For comparison, reflectance spectra were calculated as an average of the homogeneously implanted (with 2 at.%) GST film and a comparable intrinsic GST film (gray dashed lines) for the amorphous (both regions amorphous), partially annealed (intrinsic is rock-salt, implanted is amorphous), and completely annealed (both regions crystalline) states. (d) Optical microscopy images of the area-selectively implanted GST film in the states from (c).

with various square openings with sizes of 500 μm to 800 μm arranged in a square grid with cell size of 1000 μm . The thickness of the mask was thick enough so that no ions were able to penetrate through and reach the GST film; thus, only the opened regions were implanted with 2 at.% As using the box-profile shown in figure 7.5a. The mask was removed prior to any further characterization (for details see section 3.4.1).

Figure 7.6a depicts the first order derivative of the TRR curves of the area-selectively implanted GST film in the as-irradiated state and after multiple cycles (I to V). Note that the spot-size of the TRR setup is 2.9 mm; thus, the laser light averages over most of the fabricated structure. After ion implantation two distinct peaks occur in the derivative of the reflectance change upon thermal annealing. However, these two peaks are not separated. Separation arises after re-amorphization and becomes even more pronounced after some cycles. Extracting the peak positions, i.e., the critical temperature T_C that is depicted in figure 7.6b for all cycles, reveals that the transition temperatures of intrinsic and implanted regions are quite different than the expected values from homogeneous As implantation. However, T_C of both intrinsic and implanted regions approaches the values of homogeneous samples upon repeated cycling.

Within the last cycle (V), the heating was interrupted at 175 °C; thus, only the intrinsic regions were crystallized while the implanted regions remain amorphous. To clarify this, reflectance measurements were performed before heating, after annealing to

175 °C, and after a second annealing step to 250 °C and are depicted in figure 7.6c. When both regions are amorphous the reflectance indeed matches well with the average of the reflectance of amorphous, intrinsic and amorphous, homogeneously implanted GST films (gray dashed line). The reflectance of the partially annealed film is in between the reflectance of amorphous and completely annealed. The spectra of both the partially and completely annealed states match also well with the averages of intrinsic and homogeneously implanted GST films assuming that implanted regions are either amorphous or crystalline, respectively, while the intrinsic regions are crystalline in both cases. This assumption is indeed observed within an optical microscope, which is depicted in figure 7.6d for the three different states from before. While the square structures are barely visible in the amorphous and completely annealed case, they are clearly distinguishable in the partially annealed state due to the distinct different reflectance of amorphous and crystalline GST in the visible spectral region. Therefore, in and out tuning of artificial phase coexistence in GST thin films using spatially selective ion implantation is unambiguously demonstrated as a proof of concept.

7.4. Conclusions

Within this chapter, it was demonstrated that impurity doping via ion implantation can be utilized to modify the crystallization process of GST thin films. Two opposing effects occur for the implantation of group V elements into GST thin films. First, the crystallization process is facilitated by the reduction of homopolar bonds caused by ion beam induced lattice damage for low doping concentrations. This was further corroborated by noble gas irradiations of as-deposited GST films as, here, no impurity doping effect is expected. Moreover, it was found that heavier ions have a more pronounced damaging effect that is accompanied with a higher reduction of the homopolar bonds destabilizing the amorphous phase. Second, the crystallization is retarded by higher contents of impurities, while various effects are proposed for different ion species. While light ions, like N, may induce a strain field due to their localization at tetrahedral interstitial sites, heavier ions may be able to substitute atoms from their lattice sites or fill the inherent vacancies in GST, which leads to the formation of additional covalent bonds inhibiting the crystallization process.

Repeated re-amorphization via ion irradiation and annealing of doped GST films was performed. The effect of induced lattice damage becomes similar for all ion species, as after multiple cycles only the contribution of Ar⁺-ion irradiation used to re-amorphize GST is dominant. While the doping effect of the lighter ions diminishes, it is roughly constant for the heavier ions upon cycling.

Enhancing the doping effect within As-doped GST by the introduction of a more

uniform implantation profile leads to well separated transitions of intrinsic (re-amorphized) and doped GST already for doping concentrations of 2 at.%. This separation was utilized to achieve artificial phase coexistence within a spatially selective implanted GST thin film by heating the sample to a temperature that is between the phase-change regimes of intrinsic and implanted regions.

8. Conclusion and outlook

The integration of phase-change materials as active media into optical devices allows to control the optical response on demand, resulting in dynamically switchable, tunable, and reconfigurable functionalities. One of the most prominent phase-change materials is the ternary chalcogenide $\text{Ge}_2\text{Sb}_2\text{Te}_5$ (GST), which exhibits drastic changes in optical and electrical properties when switching between amorphous and crystalline states. Conventional direct laser writing was recently utilized to create active photonic devices comprising artificial phase coexistence [28, 36]. However, any structure size is diffraction-limited by the laser light. Focused ion beam irradiation was introduced within this thesis to overcome this limitation by appropriately inducing lattice disorder culminating in amorphization of GST.

Three approaches were proposed and addressed for the successful integration of ion beam modified GST into active optical devices. **(I)** Tailoring the amount of lattice disorder, i.e., gaining an optical response on demand, allows to substitute conventional elaborate multi-layer coatings with one single GST layer. **(II)** The introduction of spatially selective ion irradiation enables artificial phase coexistence in GST films with feature sizes, that are not constrained by the diffraction-limit. This approach facilitates inherently flat, reconfigurable optical metasurfaces. **(III)** Spatially selective ion implantation yields locally varying impurity doping concentrations, i.e., different crystallization temperatures of GST, which readily enables active in- and out-tuning of an optical functionality.

Within **Chapter 4** the intrinsic structural and optical properties of amorphous, rock-salt, and hexagonal GST thin films were investigated. Thermal annealing of the as-deposited samples was performed using a custom-built temperature-resolved reflectance setup, which was realized within this thesis. This lead, first, to crystallization of amorphous GST into the rock-salt phase and, second, to the conversion into the hexagonal phase associated with an insulator-metal transition. The latter is attributed to a vacancy ordering process of the randomly distributed vacancies in the disordered rock-salt phase. Optical constants were carefully determined for all GST phases over the entire visible to mid-infrared spectral range.

Tailoring disorder in a phase-change material by means of ion irradiation, i.e., inducing atomic displacements (defect engineering), was introduced in **Chapter 5**. Combinatorial *in-situ* optical and electrical measurements during noble gas ion irradiation

revealed amorphization of initially rock-salt and hexagonal GST thin films that was accompanied with drastic changes of the reflectance and resistance, respectively. A significantly lower amorphization threshold was found for the rock-salt (ion fluence of $N_i \approx 1 \times 10^{14} \text{ cm}^{-2}$) compared to hexagonal phase ($\sim 5 \times 10^{14} \text{ cm}^{-2}$).

Multiple, initially crystalline GST thin films were irradiated with various Ar^+ -ion fluences and subsequently *ex-situ* structurally and optically characterized. By this means, several structural and electronic transitions were observed upon increasing disorder. The accumulation of lattice defects culminates in progressive amorphization of initially rock-salt GST films. However, several transitions occur upon ion bombardment of initially hexagonal GST. Inducing small amounts of disorder, i.e., the creation of point defects and small defect clusters, leads to disordering of the inherent vacancy layers. These van der Waals gaps in the hexagonal phase are responsible for the metal-like conduction (degenerate p-type semiconductor); hence, the disordering process causes the formation of localized states associated with a reduced carrier mobility that drives the metal-insulator transition. Furthermore, a structural conversion from hexagonal to rock-salt GST was observed via XRD; yet, this structural transition was found to be disentangled from the electronic metal-insulator transition, which is in good agreement with previous studies [59, 100, 128]. High ion fluences then cause progressive amorphization of the initially hexagonal GST films.

The differences in dynamic defect recombination during ion bombardment of rock-salt and hexagonal GST films were examined by comparing *in-situ* and *ex-situ* optical measurements and further by varying the ion flux in the *in-situ* measurements. A higher annealing rate caused by the van der Waals gaps, which act as preferential sinks for defect recombination of mainly Ge and Sb atoms [61], was observed within the hexagonal phase compared to rock-salt GST. Consequently, hexagonal GST has a higher resistance against ion irradiation considering the higher amorphization threshold.

Intermediate states between amorphous and crystalline phases become accessible by tailoring the amount of lattice disorder in GST films. It was determined that such intermediate states are stable up to $\sim 50^\circ\text{C}$. Moreover, ion beam induced lattice disorder can be completely reversed by appropriate thermal annealing giving rise to reconfigurable optical devices.

Near-zero reflection in the near infrared spectral region was achieved by appropriately coating a gold reflector with a thin GST film ($d \approx 40 \text{ nm}$). Accessing intermediate states of disorder, i.e., tailoring optical properties of the initially rock-salt GST film, revealed a tunable point of minimal reflection over a broad spectral range. Moreover, the gradually tailored optical properties allowed for precisely adjusting the near infrared ($\lambda \approx 1.7 \mu\text{m}$) reflectance between low ($\lesssim 0.1$) and high values ($\gtrsim 0.9$), which corresponds to a tremendous maximal reflectance difference of $\sim 80\%$. Further-

more, calculations demonstrated that appropriately designing the GST film thickness ($d \approx 50$ nm) would result in a reflectance difference above $\sim 98\%$. Hence, these results unambiguously demonstrate that approach **(I)** proposed within this thesis was successfully implemented by tailoring the optical properties of GST thin films. Similar to a femtosecond laser treatment of GST [53–55], ion irradiation readily serves as a tool to access intermediate states with effective optical properties enabled by tailoring disorder in GST.

Chapter 6 introduced focused ion beam irradiation of crystalline GST films in highly confined regions to address approach **(II)**. Direct patterning of a rock-salt GST film stacked on an Au/Si substrate resulted in artificial lateral phase coexistence. Such an anisotropic metasurface comprising regularly arranged amorphous stripes embedded in the crystalline matrix with feature size below the wavelength of probing light showed optical dichroism.

To further decrease the sizes of irradiated areas, the spatial limits of FIB irradiation on intrinsic hexagonal and rock-salt GST films were systematically investigated via optical nanoimaging techniques. Both PiFM and SNOM measurements, while operating at visible and infrared probing wavelengths, respectively, revealed distinct contrasts in the respective optical signals between irradiated and pristine regions. It was determined that any feature size is physically limited by lateral straggling of the ions, i.e., their lateral distribution caused by random nuclear collision cascades, and technically by the FIB's beam profile.

Appropriately adjusting the induced ion fluences, i.e., the amount of induced disorder, and the size of the irradiated regions allowed for grayscale patterning at the nanoscale. Thus, grayscale elements that consist of irradiated spots with sizes of about 40 nm were realized within a hexagonal GST film. By this means, gradually optical properties on the nanoscale, thus well below the diffraction limit of direct laser writing, are unambiguously demonstrated.

These results revealed that spatially selective ion irradiation of GST enables a novel degree of freedom and opens up new routes for designing non-volatile, reconfigurable, and inherently planar optical metasurfaces [64].

Chapter 7 introduced an alternate route to achieve lateral phase coexistence, that is, the incorporation of impurity atoms in restricted areas. Impurity doping by means of ion implantation in GST films is known to enhance the stability of the amorphous phase [212, 216, 217]. However, the implantation of group V elements into GST thin films revealed two opposing effects; while low ion fluence irradiations yielded enhanced crystallization kinetics caused by a significant reduction of homopolar bonds in the

amorphous phase, high impurity contents retarded the crystallization process. The former was corroborated by similar results obtained from noble gas irradiation of as-deposited GST films where no doping effect is expected. Different explanations for the latter effect were proposed: while light ions may occupy interstitial sites inducing a strain field, heavy ions may form additional covalent bonds when they substitute lattice atoms or occupy vacancy sites.

Approach **(III)** was addressed with a proof of concept device based on spatially selective impurity doping. As⁺-ion implantation was performed through a hundreds of microns-sized predefined lithography mask. Two well separated transitions of intrinsic and doped ($c_{As} \approx 2$ at.%) GST regions occurred in the temperature-resolved reflectance measurements. In this way, artificial phase coexistence was achieved by heating the sample appropriately so that intrinsic regions are crystallized while implanted regions are yet amorphous.

A significant reduction of the size of implanted regions, for instance via electron beam lithography, may enable the design of optical devices based on impurity doping of GST. Thus, active tuning of an optical response can be achieved by carefully adjusting the phase of distinct regions within the GST film. Furthermore, regions with different, appropriate doping concentrations may be also accessible by a multi-implantation process; this would enable various stages of phase coexistence that are accompanied with distinct optical responses.

The three chapters about tailoring disorder (**Chapter 5**), ion beam patterning (**Chapter 6**), and impurity doping (**Chapter 7**) of GST thin films have successfully demonstrated the proposed approaches to facilitate the integration of ion beam modified GST into active optical devices. Within this thesis, several simple structures were realized as a proof of concept; future works should rely on more complex structures of artificial phase coexistence that yield optical functionalities. The optical constants determined within this thesis should be used to carry out optical simulations with defined optical applications in mind. Furthermore, combining traditional metasurfaces with an artificially structured GST spacer layer may provide fascinating possibilities, such as tuning the optical response of individual nanoantennas. Moreover, the approaches presented within this thesis may serve already various applications in the fields of photonics or meta-optics. Metasurfaces comprising artificial phase coexistence are inherently flat compared to their traditional counterparts; hence, they allow to fabricate stacked multi-layer devices with optical functionalities dedicated to each layer. The experimentally obtained results presented within this thesis provide a valuable contribution to the design of active, inherently planar, non-volatile, and reconfigurable optical devices enabled by the modification of phase-change materials.

Bibliography

- [1] Poslad, S., *Ubiquitous computing: Smart devices, environments and interactions*; Wiley: Chichester, 2009.
- [2] Azuma, R.; Baillet, Y.; Behringer, R.; Feiner, S.; Julier, S.; MacIntyre, B. *IEEE Computer Graphics and Applications* **2001**, *21*, 34.
- [3] Hua, H.; Javidi, B. *Optics Express* **2014**, *22*, 13484.
- [4] Lee, C.-K.; Moon, S.; Lee, S.; Yoo, D.; Hong, J.-Y.; Lee, B. *Optics Express* **2016**, *24*, 19531.
- [5] Maimone, A.; Georgiou, A.; Kollin, J. S. *ACM Transactions on Graphics* **2017**, *36*, 1.
- [6] Lee, G.-Y.; Hong, J.-Y.; Hwang, S.; Moon, S.; Kang, H.; Jeon, S.; Kim, H.; Jeong, J.-H.; Lee, B. *Nature Communications* **2018**, *9*, 4562.
- [7] Kildishev, A. V.; Boltasseva, A.; Shalaev, V. M. *Science* **2013**, *339*, 1232009.
- [8] Yu, N.; Capasso, F. *Nature Materials* **2014**, *13*, 139.
- [9] Khorasaninejad, M.; Capasso, F. *Science* **2017**, *358*, eaam8100.
- [10] Yu, N.; Genevet, P.; Kats, M. A.; Aieta, F.; Tetienne, J.-P.; Capasso, F.; Gaburro, Z. *Science* **2011**, *334*, 333.
- [11] Zheludev, N. I.; Kivshar, Y. S. *Nature Materials* **2012**, *11*, 917.
- [12] Keren-Zur, S.; Avayu, O.; Michaeli, L.; Ellenbogen, T. *ACS Photonics* **2016**, *3*, 117.
- [13] Desiatov, B.; Mazurski, N.; Fainman, Y.; Levy, U. *Optics Express* **2015**, *23*, 22611.
- [14] Aieta, F.; Genevet, P.; Kats, M. A.; Yu, N.; Blanchard, R.; Gaburro, Z.; Capasso, F. *Nano Letters* **2012**, *12*, 4932.
- [15] Khorasaninejad, M.; Chen, W. T.; Devlin, R. C.; Oh, J.; Zhu, A. Y.; Capasso, F. *Science* **2016**, *352*, 1190.
- [16] Li, G.; Zhang, S.; Zentgraf, T. *Nature Reviews Materials* **2017**, *2*, 523.
- [17] Sartorello, G.; Olivier, N.; Zhang, J.; Yue, W.; Gosztola, D. J.; Wiederrecht, G. P.; Wurtz, G.; Zayats, A. V. *ACS Photonics* **2016**, *3*, 1517.
- [18] Zheng, G.; Mühlenbernd, H.; Kenney, M.; Li, G.; Zentgraf, T.; Zhang, S. *Nature Nanotechnology* **2015**, *10*, 308.
- [19] Wan, W.; Gao, J.; Yang, X. *ACS Nano* **2016**, *10*, 10671.

- [20] Akselrod, G. M.; Huang, J.; Hoang, T. B.; Bowen, P. T.; Su, L.; Smith, D. R.; Mikkelsen, M. H. *Advanced Materials* **2015**, *27*, 8028.
- [21] Cheng, F.; Gao, J.; Luk, T. S.; Yang, X. *Scientific Reports* **2015**, *5*, 11045.
- [22] Schuller, J. A.; Zia, R.; Taubner, T.; Brongersma, M. L. *Physical Review Letters* **2007**, *99*, 107401.
- [23] Kuznetsov, A. I.; Miroshnichenko, A. E.; Brongersma, M. L.; Kivshar, Y. S.; Luk'yanchuk, B. *Science* **2016**, *354*, aag2472.
- [24] Lin, D.; Fan, P.; Hasman, E.; Brongersma, M. L. *Science* **2014**, *345*, 298.
- [25] Ambrosio, A. *Journal of Optics* **2018**, *20*, 113002.
- [26] Zheludev, N. I. *Science* **2015**, *348*, 973.
- [27] Sautter, J.; Staude, I.; Decker, M.; Rusak, E.; Neshev, D. N.; Brener, I.; Kivshar, Y. S. *ACS Nano* **2015**, *9*, 4308.
- [28] Wang, Q.; Rogers, E. T. F.; Gholipour, B.; Wang, C.-M.; Yuan, G.; Teng, J.; Zheludev, N. I. *Nature Photonics* **2016**, *10*, 60.
- [29] Park, J.; Kang, J.-H.; Liu, X.; Brongersma, M. L. *Scientific Reports* **2015**, *5*, 15754.
- [30] Zhao, Q.; Kang, L.; Du, B.; Li, B.; Zhou, J.; Tang, H.; Liang, X.; Zhang, B. *Applied Physics Letters* **2007**, *90*, 011112.
- [31] Yao, Y.; Shankar, R.; Kats, M. A.; Song, Y.; Kong, J.; Loncar, M.; Capasso, F. *Nano Letters* **2014**, *14*, 6526.
- [32] Kats, M. A.; Blanchard, R.; Genevet, P.; Yang, Z.; Qazilbash, M. M.; Basov, D. N.; Ramanathan, S.; Capasso, F. *Optics letters* **2013**, *38*, 368.
- [33] Gholipour, B.; Zhang, J.; MacDonald, K. F.; Hewak, D. W.; Zheludev, N. I. *Advanced Materials* **2013**, *25*, 3050.
- [34] De Galarreta, C. R.; Alexeev, A. M.; Au, Y.-Y.; Lopez-Garcia, M.; Klemm, M.; Cryan, M.; Bertolotti, J.; Wright, C. D. *Advanced Functional Materials* **2018**, *28*, 1704993.
- [35] Gholipour, B.; Karvounis, A.; Yin, J.; Soci, C.; MacDonald, K. F.; Zheludev, N. I. *NPG Asia Materials* **2018**, *10*, 533.
- [36] Li, P.; Yang, X.; Masz, T. W. W.; Hanss, J.; Lewin, M.; Michel, A.-K. U.; Wuttig, M.; Taubner, T. *Nature Materials* **2016**, *15*, 870.
- [37] Raeis-Hosseini, N.; Rho, J. *Materials* **2017**, *10*, 1046.
- [38] Tittl, A.; Michel, A.-K. U.; Schäferling, M.; Yin, X.; Gholipour, B.; Cui, L.; Wuttig, M.; Taubner, T.; Neubrech, F.; Giessen, H. *Advanced Materials* **2015**, *27*, 4597.

- [39] Michel, A.-K. U.; Chigrin, D. N.; Maß, T. W. W.; Schönauer, K.; Salinga, M.; Wuttig, M.; Taubner, T. *Nano Letters* **2013**, *13*, 3470.
- [40] Wei, M.; Song, Z.; Deng, Y.; Liu, Y.; Chen, Q. *Materials Letters* **2019**, *236*, 350.
- [41] Yin, X.; Steinle, T.; Huang, L.; Taubner, T.; Wuttig, M.; Zentgraf, T.; Giessen, H. *Light, Science & Applications* **2017**, *6*, 17016.
- [42] Wuttig, M.; Bhaskaran, H.; Taubner, T. *Nature Photonics* **2017**, *11*, 465.
- [43] Ovshinsky, S. R. *Physical Review Letters* **1968**, *21*, 1450.
- [44] Yamada, N.; Ohno, E.; Akahira, N.; Nishiuchi, K.; Nagata, K.; Takao, M. *Japanese Journal of Applied Physics* **1987**, *26*, 61.
- [45] Wuttig, M.; Yamada, N. *Nature materials* **2007**, *6*, 824.
- [46] Raoux, S.; Welnic, W.; Ielmini, D. *Chemical reviews* **2010**, *110*, 240.
- [47] Wolfram H. P. Pernice; Harish Bhaskaran *Applied Physics Letters* **2012**, *101*, 171101.
- [48] Yamada, N.; Ohno, E.; Nishiuchi, K.; Akahira, N.; Takao, M. *Journal of Applied Physics* **1991**, *69*, 2849.
- [49] Yamada, N. *physica status solidi (b)* **2012**, *249*, 1837.
- [50] Raoux, S.; Jordan-Sweet, J. L.; Kellock, A. J. *Journal of Applied Physics* **2008**, *103*, 114310.
- [51] Weidenhof, V.; Friedrich, I.; Ziegler, S.; Wuttig, M. *Journal of Applied Physics* **2001**, *89*, 3168.
- [52] Weidenhof, V.; Pirch, N.; Friedrich, I.; Ziegler, S.; Wuttig, M. *Journal of Applied Physics* **2000**, *88*, 657.
- [53] Michel, A.-K. U.; Zalden, P.; Chigrin, D. N.; Wuttig, M.; Lindenberg, A. M.; Taubner, T. *ACS Photonics* **2014**, *1*, 833.
- [54] Konishi, M.; Santo, H.; Hongo, Y.; Tajima, K.; Hosoi, M.; Saiki, T. *Applied Optics* **2010**, *49*, 3470.
- [55] Wang, Q.; Maddock, J.; Rogers, E. T. F.; Roy, T.; Craig, C.; Macdonald, K. F.; Hewak, D. W.; Zheludev, N. I. *Applied Physics Letters* **2014**, *104*, 121105.
- [56] Karvounis, A.; Gholipour, B.; MacDonald, K. F.; Zheludev, N. I. *Applied Physics Letters* **2016**, *109*, 051103.
- [57] Gholipour, B.; Piccinotti, D.; Karvounis, A.; MacDonald, K. F.; Zheludev, N. I. *Nano Letters* **2019**, *19*, 1643.

- [58] De Bastiani, R.; Piro, A. M.; Grimaldi, M. G.; Rimini, E. *Nuclear Instruments and Methods in Physics Research Section B: Beam Interactions with Materials and Atoms* **2007**, *257*, 572.
- [59] Privitera, S. M. S.; Mio, A. M.; Smecca, E.; Alberti, A.; Zhang, W.; Mazzarello, R.; Benke, J.; Persch, C.; La Via, F.; Rimini, E. *Physical Review B* **2016**, *94*.
- [60] Privitera, S. M. S.; Mio, A. M.; Dück, M.; Persch, C.; Zimbone, M.; Wuttig, M.; Rimini, E. *Journal of Physics D: Applied Physics* **2018**, *51*, 495103.
- [61] Mio, A. M.; Privitera, S. M. S.; Zimbone, M.; Bragaglia, V.; Jacobs, S.; Persch, C.; Arciprete, F.; Calarco, R.; Wuttig, M.; Rimini, E. *Journal of Physics D: Applied Physics* **2020**, *53*, 134001.
- [62] Kats, M. A.; Sharma, D.; Lin, J.; Genevet, P.; Blanchard, R.; Yang, Z.; Qazilbash, M. M.; Basov, D. N.; Ramanathan, S.; Capasso, F. *Applied Physics Letters* **2012**, *101*, 221101.
- [63] Kats, M. A.; Blanchard, R.; Genevet, P.; Capasso, F. *Nature materials* **2013**, *12*, 20.
- [64] Phan, T.; Sell, D.; Wang, E. W.; Doshay, S.; Edee, K.; Yang, J.; Fan, J. A. *Light, Science & Applications* **2019**, *8*, 48.
- [65] Hafermann, M.; Zapf, M.; Ritzer, M.; Printschler, A.; Luo, Y.; Ambrosio, A.; Wilson, W. L.; Ronning, C. *ACS Applied Nano Materials* **2020**, *3*, 4486.
- [66] Printschler, A., bachelor thesis, Friedrich Schiller University Jena, 2020.
- [67] Hafermann, M.; Schöppe, P.; Rensberg, J.; Ronning, C. *ACS Photonics* **2018**, *5*, 5103.
- [68] Schock, R. T. K., master thesis, Friedrich Schiller University Jena, 2020.
- [69] Grandmontagne, J., bachelor thesis, Friedrich Schiller University Jena, 2020.
- [70] Wesch, W.; Wendler, E., *Ion Beam Modification of Solids: Ion-Solid Interaction and Radiation Damage*; Springer Series in Surface Sciences, Vol. v.61; Springer International Publishing: Cham, 2016.
- [71] Li, J.; Stein, D.; McMullan, C.; Branton, D.; Aziz, M. J.; Golovchenko, J. A. *Nature* **2001**, *412*, 166.
- [72] Akcöltekin, E.; Peters, T.; Meyer, R.; Duvenbeck, A.; Klusmann, M.; Monnet, I.; Lebius, H.; Schleberger, M. *Nature Nanotechnology* **2007**, *2*, 290.
- [73] Jain, I. P.; Agarwal, G. *Surface Science Reports* **2011**, *66*, 77.
- [74] Ridgway, M. C.; Giulian, R.; Sprouster, D. J.; Kluth, P.; Araujo, L. L.; Llewellyn, D. J.; Byrne, A. P.; Kremer, F.; Fichtner, P. F. P.; Rizza, G.; Amekura, H.; Toulemonde, M. *Physical Review Letters* **2011**, *106*, 095505.

- [75] Jubera, M.; Villarroel, J.; García-Cabañes, A.; Carrascosa, M.; Olivares, J.; Agullo-López, F.; Méndez, A.; Ramiro, J. B. *Applied Physics B* **2012**, *107*, 157.
- [76] Weber, W. J.; Duffy, D. M.; Thomé, L.; Zhang, Y. *Current Opinion in Solid State and Materials Science* **2015**, *19*, 1.
- [77] Nastasi, M.; Mayer, J. W., *Ion Implantation and Synthesis of Materials*; Springer Berlin Heidelberg: Berlin, Heidelberg, 2006.
- [78] Rensberg, J.; Zhang, S.; Zhou, Y.; McLeod, A. S.; Schwarz, C.; Goldflam, M.; Liu, M.; Kerbusch, J.; Nawrodt, R.; Ramanathan, S.; Basov, D. N.; Capasso, F.; Ronning, C.; Kats, M. A. *Nano Letters* **2016**, *16*, 1050.
- [79] He, Z.; Zhao, R.; Chen, X.; Chen, H.; Zhu, Y.; Su, H.; Huang, S.; Xue, J.; Dai, J.; Cheng, S.; Liu, M.; Wang, X.; Chen, Y. *ACS applied materials & interfaces* **2018**, *10*, 42524.
- [80] Lin, Z.; Carvalho, B. R.; Kahn, E.; Lv, R.; Rao, R.; Terrones, H.; Pimenta, M. A.; Terrones, M. *2D Materials* **2016**, *3*, 022002.
- [81] Ziegler, J. F.; Ziegler, M. D.; Biersack, J. P. *Nuclear Instruments and Methods in Physics Research Section B: Beam Interactions with Materials and Atoms* **2010**, *268*, 1818.
- [82] Nastasi, M.; Mayer, J.; Hirvonen, J. K., *Ion-Solid Interactions*; Cambridge University Press: 2010.
- [83] Nordlund, K.; Ghaly, M.; Averback, R. S. *Journal of Applied Physics* **1998**, *83*, 1238.
- [84] Abedrabbo, S.; Arafah, D.-E.; Salem, S. *Journal of Electronic Materials* **2005**, *34*, 468.
- [85] Abedrabbo, S.; Arafah, D. E.; Gokce, O.; Wielunski, L. S.; Gharaibeh, M.; Celik, O.; Ravindra, N. M. *Journal of Electronic Materials* **2006**, *35*, 834.
- [86] International Union of Crystallography *Acta Crystallographica Section A Foundations of Crystallography* **1992**, *48*, 922.
- [87] Wuttig, M.; Steimer, C. *Applied Physics A* **2007**, *87*, 411.
- [88] Ríos, C.; Stegmaier, M.; Hosseini, P.; Di Wang; Scherer, T.; Wright, C. D.; Bhaskaran, H.; Pernice, W. H. P. *Nature Photonics* **2015**, *9*, 725.
- [89] Wong, H.-S. P.; Raoux, S.; Kim, S.; Liang, J.; Reifenberg, J. P.; Rajendran, B.; Asheghi, M.; Goodson, K. E. *Proceedings of the IEEE* **2010**, *98*, 2201.
- [90] Yamada, N.; Kojima, R.; Hisada, K.; Mihara, T.; Tsuchino, A.; Fujinoki, N.; Birukawa, M.; Matsunaga, T.; Yasuda, N.; Fukuyama, Y.; Ito, K.; Tanaka, Y.; Kimura, S.; Takata, M. *Advanced Optical Materials* **2013**, *1*, 820.

- [91] Lencer, D.; Salinga, M.; Wuttig, M. *Advanced materials (Deerfield Beach, Fla.)* **2011**, 23, 2030.
- [92] Matsunaga, T.; Akola, J.; Kohara, S.; Honma, T.; Kobayashi, K.; Ikenaga, E.; Jones, R. O.; Yamada, N.; Takata, M.; Kojima, R. *Nature materials* **2011**, 10, 129.
- [93] Kelton, K. F.; Greer, A. L., *Nucleation in condensed matter: Applications in materials and biology*; Pergamon materials series; Pergamon: Oxford, U.K., 2010.
- [94] Salinga, M., Ph.D. thesis, RWTH Aachen University, 2008.
- [95] Kalikmanov, V. I. In *Nucleation Theory*, Kalikmanov, V. I., Ed.; Lecture Notes in Physics, Vol. 860; Springer Netherlands: Dordrecht, 2013, pp 17–41.
- [96] Sear, R. P. *Journal of Physics: Condensed Matter* **2007**, 19, 033101.
- [97] Bruns, G.; Merkelbach, P.; Schlockermann, C.; Salinga, M.; Wuttig, M.; Happ, T. D.; Philipp, J. B.; Kund, M. *Applied Physics Letters* **2009**, 95, 043108.
- [98] Santala, M. K.; Reed, B. W.; Topuria, T.; Raoux, S.; Meister, S.; Cui, Y.; LaGrange, T.; Campbell, G. H.; Browning, N. D. *Journal of Applied Physics* **2012**, 111, 024309.
- [99] Saxena, N.; Persch, C.; Wuttig, M.; Manivannan, A. *Scientific reports* **2019**, 9, 19251.
- [100] Siegrist, T.; Jost, P.; Volker, H.; Woda, M.; Merkelbach, P.; Schlockermann, C.; Wuttig, M. *Nature materials* **2011**, 10, 202.
- [101] Rocca, J.; García, J. L.; Ureña, M. A.; Fontana, M.; Arcondo, B. *Materials Research* **2019**, 22, 1.
- [102] Chen, M.; Rubin, K. A.; Barton, R. W. *Applied Physics Letters* **1986**, 49, 502.
- [103] Iwasaki, H.; Harigaya, M.; Nonoyama, O.; Kageyama, Y.; Takahashi, M.; Yamada, K.; Deguchi, H.; Ide, Y. *Japanese Journal of Applied Physics* **1993**, 32, 5241.
- [104] Matsunaga, T.; Yamada, N. *Japanese Journal of Applied Physics* **2004**, 43, 4704.
- [105] Afonso, C. N.; Solis, J.; Catalina, F.; Kalpouzios, C. *Applied Physics Letters* **1992**, 60, 3123.
- [106] Shportko, K. V. *Scientific reports* **2019**, 9, 6030.
- [107] Park, J.-W.; Baek, S. H.; Kang, T. D.; Lee, H.; Kang, Y.-S.; Lee, T.-Y.; Suh, D.-S.; Kim, K. J.; Kim, C. K.; Khang, Y. H.; Da Silva, J. L. F.; Wei, S.-H. *Applied Physics Letters* **2008**, 93, 021914.
- [108] Zallen, R., *The physics of amorphous solids*; VCH: 1998.
- [109] Kolobov, A. V.; Fons, P.; Frenkel, A. I.; Ankudinov, A. L.; Tominaga, J.; Uruga, T. *Nature materials* **2004**, 3, 703.

- [110] Andrikopoulos, K. S.; Yannopoulos, S. N.; Voyiatzis, G. A.; Kolobov, A. V.; Ribes, M.; Tominaga, J. *Journal of Physics: Condensed Matter* **2006**, *18*, 965.
- [111] Andrikopoulos, K. S.; Yannopoulos, S. N.; Kolobov, A. V.; Fons, P.; Tominaga, J. *Journal of Physics and Chemistry of Solids* **2007**, *68*, 1074.
- [112] Hosokawa, S.; Ozaki, T.; Hayashi, K.; Happo, N.; Fujiwara, M.; Horii, K.; Fons, P.; Kolobov, A. V.; Tominaga, J. *Applied Physics Letters* **2007**, *90*, 131913.
- [113] Wefnic, W.; Pamungkas, A.; Detemple, R.; Steimer, C.; Blügel, S.; Wuttig, M. *Nature materials* **2006**, *5*, 56.
- [114] Caravati, S.; Bernasconi, M.; Kühne, T. D.; Krack, M.; Parrinello, M. *Applied Physics Letters* **2007**, *91*, 171906.
- [115] Akola, J., J. Larrucea, and R. O. Jones *European Phase-Change and Ovonic Symposium 2010* **2010**.
- [116] Jóvári, P.; Kaban, I.; Steiner, J.; Beuneu, B.; Schöps, A.; Webb, A. *Journal of physics. Condensed matter : an Institute of Physics journal* **2007**, *19*, 335212.
- [117] Jóvári, P.; Kaban, I.; Steiner, J.; Beuneu, B.; Schöps, A.; Webb, M. A. *Physical Review B* **2008**, *77*, 035202.
- [118] Kohara, S.; Kato, K.; Kimura, S.; Tanaka, H.; Usuki, T.; Suzuya, K.; Tanaka, H.; Moritomo, Y.; Matsunaga, T.; Yamada, N.; Tanaka, Y.; Suematsu, H.; Takata, M. *Applied Physics Letters* **2006**, *89*, 201910.
- [119] Akola, J.; Jones, R. O. *Physical Review B* **2007**, *76*, 235201.
- [120] Akola, J.; Jones, R. O. *Journal of Physics: Condensed Matter* **2008**, *20*, 465103.
- [121] Hegedüs, J.; Elliott, S. R. *Nature Materials* **2008**, *7*, 399.
- [122] Caravati, S.; Bernasconi, M.; Kühne, T. D.; Krack, M.; Parrinello, M. *Journal of Physics: Condensed Matter* **2009**, *21*, 255501.
- [123] Akola, J.; Jones, R. O.; Kohara, S.; Kimura, S.; Kobayashi, K.; Takata, M.; Matsunaga, T.; Kojima, R.; Yamada, N. *Physical Review B* **2009**, *80*, 020201.
- [124] Xu, M.; Cheng, Y. Q.; Sheng, H. W.; Ma, E. *Physical Review Letters* **2009**, *103*, 195502.
- [125] Carria, E.; Mio, A. M.; Gibilisco, S.; Miritello, M.; d'Acapito, F.; Grimaldi, M. G.; Rimini, E. *Electrochemical and Solid-State Letters* **2011**, *14*, H480.
- [126] Nonaka, T.; Ohbayashi, G.; Toriumi, Y.; Mori, Y.; Hashimoto, H. *Thin Solid Films* **2000**, *370*, 258.
- [127] Yamada, N.; Matsunaga, T. *Journal of Applied Physics* **2000**, *88*, 7020.

- [128] Wuttig, M.; Lüsebrink, D.; Wamwangi, D.; Welnic, W.; Gillessen, M.; Dronskowski, R. *Nature materials* **2007**, *6*, 122.
- [129] Fukata, N.; Kasuya, A.; Suezawa, M. *Japanese Journal of Applied Physics* **2001**, *40*, L854.
- [130] Shamoto, S.; Yamada, N.; Matsunaga, T.; Proffen, T.; Richardson, J. W.; Chung, J.-H.; Egami, T. *Applied Physics Letters* **2005**, *86*, 081904.
- [131] Urban, P.; Schneider, M. N.; Erra, L.; Welzmler, S.; Fahrnbauer, F.; Oeckler, O. *CrystEngComm* **2013**, *15*, 4823.
- [132] Petrov, I. I., R. M. Imamov, and Z. G. Pinsker *Soviet physics / Crystallography* **1968**, *13*, 339.
- [133] Kooi, B. J.; de Hosson, J. T. M. *Journal of Applied Physics* **2002**, *92*, 3584.
- [134] Matsunaga, T.; Yamada, N.; Kubota, Y. *Acta crystallographica. Section B, Structural science* **2004**, *60*, 685.
- [135] Mio, A. M.; Privitera, S. M. S.; Bragaglia, V.; Arciprete, F.; Cecchi, S.; Litrico, G.; Persch, C.; Calarco, R.; Rimini, E. *Scientific reports* **2017**, *7*, 2616.
- [136] Wang, J.-J.; Xu, Y.-Z.; Mazzarello, R.; Wuttig, M.; Zhang, W. *Materials (Basel, Switzerland)* **2017**, *10*, 1.
- [137] Momand, J.; Lange, F. R.; Wang, R.; Boschker, J. E.; Verheijen, M. A.; Calarco, R.; Wuttig, M.; Kooi, B. J. *Journal of Materials Research* **2016**, *31*, 3115.
- [138] Yamanaka, S.; Ogawa, S.; Morimoto, I.; Ueshima, Y. *Japanese Journal of Applied Physics* **1998**, *37*, 3327.
- [139] Kim, J.-J.; Kobayashi, K.; Ikenaga, E.; Kobata, M.; Ueda, S.; Matsunaga, T.; Kifune, K.; Kojima, R.; Yamada, N. *Physical Review B* **2007**, *76*, 115124.
- [140] Kato, T.; Tanaka, K. *Japanese Journal of Applied Physics* **2005**, *44*, 7340.
- [141] Subramaniam, D.; Pauly, C.; Liebmann, M.; Woda, M.; Rausch, P.; Merkelbach, P.; Wuttig, M.; Morgenstern, M. *Applied Physics Letters* **2009**, *95*, 103110.
- [142] Pirovano, A.; Lacaita, A. L.; Benvenuti, A.; Pellizzer, F.; Bez, R. *IEEE Transactions on Electron Devices* **2004**, *51*, 452.
- [143] Shportko, K.; Kremers, S.; Woda, M.; Lencer, D.; Robertson, J.; Wuttig, M. *Nature Materials* **2008**, *7*, 653.
- [144] Mott, N. F.; Davis, E. A., *Electronic processes in non-crystalline materials*, 2. ed., 1st published in paperback; Oxford classic texts in the physical sciences; Oxford Univ. Press: Oxford, 2012.

- [145] Cohen, M. H.; Fritzsche, H.; Ovshinsky, S. R. In *Disordered Materials*, Adler, D., Schwartz, B. B., Silver, M., Eds.; Springer US: Boston, MA, 1991, pp 14–16.
- [146] Singh, P.; Singh, A. P.; Kanda, N.; Mishra, M.; Gupta, G.; Thakur, A. *Applied Physics Letters* **2017**, *111*, 261102.
- [147] Klein, A.; Dieker, H.; Späth, B.; Fons, P.; Kolobov, A.; Steimer, C.; Wuttig, M. *Physical Review Letters* **2008**, *100*, 016402.
- [148] Sun, Z.; Pan, Y.; Zhou, J.; Sa, B.; Ahuja, R. *Physical Review B* **2011**, *83*, 113201.
- [149] Edwards, A.; Pineda, A.; Schultz, P.; Martin, M.; Thompson, A.; Hjalmanson, H.; Umrigar, C. *Physical Review B* **2006**, *73*, 045210.
- [150] Moss, T. S., *Optical Properties of Semiconductors*; Butterworths: London, 1959.
- [151] Tsafack, T.; Piccinini, E.; Lee, B.-S.; Pop, E.; Rudan, M. *Journal of Applied Physics* **2011**, *110*, 063716.
- [152] Kohary, K.; Burlakov, V. M.; Pettifor, D. G. *Physical Review B* **2005**, *71*, 235309.
- [153] Ohara, K.; Temleitner, L.; Sugimoto, K.; Kohara, S.; Matsunaga, T.; Pusztai, L.; Itou, M.; Ohsumi, H.; Kojima, R.; Yamada, N.; Usuki, T.; Fujiwara, A.; Takata, M. *Advanced Functional Materials* **2012**, *22*, 2251.
- [154] Mott, N. F. *Proceedings of the Royal Society of London. A. Mathematical and Physical Sciences* **1982**, *382*, 1.
- [155] Anderson, P. W. *Physical Review* **1958**, *109*, 1492.
- [156] Zhang, B.; Zhang, W.; Shen, Z.; Chen, Y.; Li, J.; Zhang, S.; Zhang, Z.; Wuttig, M.; Mazzarello, R.; Ma, E.; Han, X. *Applied Physics Letters* **2016**, *108*, 191902.
- [157] Lencer, D.; Salinga, M.; Grabowski, B.; Hickel, T.; Neugebauer, J.; Wuttig, M. *Nature materials* **2008**, *7*, 972.
- [158] Volker, H.; Jost, P.; Wuttig, M. *Advanced Functional Materials* **2015**, *25*, 6390.
- [159] Jost, P.; Volker, H.; Poitz, A.; Poltorak, C.; Zalden, P.; Schäfer, T.; Lange, F. R. L.; Schmidt, R. M.; Holländer, B.; Wirtsohn, M. R.; Wuttig, M. *Advanced Functional Materials* **2015**, *25*, 6399.
- [160] Zhang, W.; Thiess, A.; Zalden, P.; Zeller, R.; Dederichs, P. H.; Raty, J.-Y.; Wuttig, M.; Blügel, S.; Mazzarello, R. *Nature materials* **2012**, *11*, 952.
- [161] Zhang, W.; Wuttig, M.; Mazzarello, R. *Scientific reports* **2015**, *5*, 13496.
- [162] Bragaglia, V.; Arciprete, F.; Zhang, W.; Mio, A. M.; Zallo, E.; Perumal, K.; Giussani, A.; Cecchi, S.; Boschker, J. E.; Riechert, H.; Privitera, S.; Rimini, E.; Mazzarello, R.; Calarco, R. *Scientific reports* **2016**, *6*, 23843.

- [163] Zhang, B.; Wang, X.-P.; Shen, Z.-J.; Li, X.-B.; Wang, C.-S.; Chen, Y.-J.; Li, J.-X.; Zhang, J.-X.; Zhang, Z.; Zhang, S.-B.; Han, X.-D. *Scientific reports* **2016**, *6*, 25453.
- [164] Hilmi, I.; Lotnyk, A.; Gerlach, J. W.; Schumacher, P.; Rauschenbach, B. *Materials & Design* **2017**, *115*, 138.
- [165] Park, Y.-J.; Cho, J.-Y.; Jeong, M.-W.; Na, S.; Joo, Y.-C. *Scientific reports* **2016**, *6*, 21466.
- [166] Wetnic, W.; Botti, S.; Reining, L.; Wuttig, M. *Physical Review Letters* **2007**, *98*, 236403.
- [167] Orava, J.; Wágner, T.; Šik, J.; Přikryl, J.; Frumar, M.; Beneš, L. *Journal of Applied Physics* **2008**, *104*, 043523.
- [168] Zhang, Y. et al. *Nature Communications* **2019**, *10*, 4279.
- [169] Wang, Q.; Konze, P. M.; Liu, G.; Liu, B.; Chen, X.; Song, Z.; Dronskowski, R.; Zhu, M. *The Journal of Physical Chemistry C* **2019**, *123*, 30640.
- [170] Jeong, T. H.; Kim, M. R.; Seo, H.; Park, J. W.; Yeon, C. *Japanese Journal of Applied Physics* **2000**, *39*, 2775.
- [171] Kim, S. M.; Jun, J. H.; Choi, D. J.; Hong, S. K.; Park, Y. J. *Japanese Journal of Applied Physics* **2005**, *44*, L208.
- [172] Lai, Y.; Qiao, B.; Feng, J.; Ling, Y.; Lai, L.; Lin, Y.; Tang, T.; Cai, B.; Chen, B. *Journal of Electronic Materials* **2005**, *34*, 176.
- [173] Seo, H.; Jeong, T.-H.; Park, J.-W.; Yeon, C.; Kim, S.-J.; Kim, S.-Y. *Japanese Journal of Applied Physics* **2000**, *39*, 745.
- [174] Shelby, R. M.; Raoux, S. *Journal of Applied Physics* **2009**, *105*, 104902.
- [175] Li, T.; Wu, L.; Ji, X.; Zheng, Y.; Liu, G.; Song, Z.; Shi, J.; Zhu, M.; Song, S.; Feng, S. *AIP Advances* **2018**, *8*, 025201.
- [176] Zhou, X.; Xia, M.; Rao, F.; Wu, L.; Li, X.; Song, Z.; Feng, S.; Sun, H. *ACS applied materials & interfaces* **2014**, *6*, 14207.
- [177] Gao, Q.; Chen, L. *Applied Physics A* **2019**, *125*, 564.
- [178] Gu, T.; Wang, J.; Liu, H.; Wang, Z.; Luo, Y.; Liu, P.; Zhong, J.; Wang, G. *Vacuum* **2017**, *145*, 258.
- [179] Jeong, S.-M.; Kim, K.-H.; Choi, S.-M.; Lee, H.-L. *Japanese Journal of Applied Physics* **2009**, *48*, 045503.
- [180] Ling, Y.; Lin, Y.; Qiao, B.; Lai, Y.; Feng, J.; Tang, T.; Cai, B.; Chen, B. *Japanese Journal of Applied Physics* **2006**, *45*, L349.

- [181] Yang, F.; Tang, X.; Chen, T.; Wang, M.; Le Zhang; Han, J.; Wan, L.; Ke, D.; Dai, Y. *Computational Materials Science* **2019**, *168*, 253.
- [182] Jeong, T. H.; Seo, H.; Lee, K. L.; Choi, S. M.; Kim, S. J.; Kim, S. Y. *Japanese Journal of Applied Physics* **2001**, *40*, 1609.
- [183] Madhavan, V. E.; Carignano, M.; Kachmar, A.; Sangunni, K. S. *Scientific reports* **2019**, *9*, 12985.
- [184] Wang, G.; Nie, Q.; Shen, X.; Wang, R. P.; Wu, L.; Fu, J.; Xu, T.; Dai, S. *Applied Physics Letters* **2012**, *101*, 051906.
- [185] Babich, A.; Sherchenkov, A.; Kozyukhin, S.; Lazarenko, P.; Boytsova, O.; Shuliyev, A. *Journal of Thermal Analysis and Calorimetry* **2017**, *127*, 283.
- [186] Park, T.-J.; Choi, S.-Y.; Kang, M.-J. *Thin Solid Films* **2007**, *515*, 5049.
- [187] Guo, P.; Burrow, J. A.; Sevison, G. A.; Sood, A.; Asheghi, M.; Hendrickson, J. R.; Goodson, K. E.; Agha, I.; Sarangan, A. *Applied Physics Letters* **2018**, *113*, 171903.
- [188] Guo, S.; Ding, X. J.; Zhang, J. Z.; Hu, Z. G.; Ji, X. L.; Wu, L. C.; Song, Z. T.; Chu, J. H. *Applied Physics Letters* **2015**, *106*, 052105.
- [189] Guo, P.; Sarangan, A.; Agha, I. *Applied Sciences* **2019**, *9*, 530.
- [190] Kolobov, A. V.; Krbal, M.; Fons, P.; Tominaga, J.; Uruga, T. *Nature chemistry* **2011**, *3*, 311.
- [191] Mitrofanov, K. V. et al. *Scientific reports* **2016**, *6*, 20633.
- [192] Lotnyk, A.; Bernütz, S.; Sun, X.; Ross, U.; Ehrhardt, M.; Rauschenbach, B. *Acta Materialia* **2016**, *105*, 1.
- [193] Xu, M.; Zhang, W.; Mazzarello, R.; Wuttig, M. *Advanced science (Weinheim, Baden-Wuerttemberg, Germany)* **2015**, *2*, 1500117.
- [194] Xu, M.; Cheng, Y. Q.; Wang, L.; Sheng, H. W.; Meng, Y.; Yang, W. G.; Han, X. D.; Ma, E. *Proceedings of the National Academy of Sciences of the United States of America* **2012**, *109*, E1055.
- [195] Caravati, S.; Bernasconi, M.; Kühne, T. D.; Krack, M.; Parrinello, M. *Physical Review Letters* **2009**, *102*, 205502.
- [196] Caravati, S.; Sosso, G. C.; Bernasconi, M.; Parrinello, M. *Physical Review B* **2013**, *87*, 094117.
- [197] Krbal, M.; Kolobov, A. V.; Haines, J.; Fons, P.; Levelut, C.; Le Parc, R.; Hanfland, M.; Tominaga, J.; Pradel, A.; Ribes, M. *Physical Review Letters* **2009**, *103*, 115502.
- [198] Sun, Z.; Zhou, J.; Pan, Y.; Song, Z.; Mao, H.-K.; Ahuja, R. *Proceedings of the National Academy of Sciences of the United States of America* **2011**, *108*, 10410.

- [199] Kalikka, J.; Zhou, X.; Dilcher, E.; Wall, S.; Li, J.; Simpson, R. E. *Nature Communications* **2016**, *7*, 11983.
- [200] Zhou, X.; Kalikka, J.; Ji, X.; Wu, L.; Song, Z.; Simpson, R. E. *Advanced Materials* **2016**, *28*, 3007.
- [201] Bragaglia, V.; Jenichen, B.; Giussani, A.; Perumal, K.; Riechert, H.; Calarco, R. *Journal of Applied Physics* **2014**, *116*, 054913.
- [202] Wang, R.; Zhang, W.; Momand, J.; Ronneberger, I.; Boschker, J. E.; Mazzarello, R.; Kooi, B. J.; Riechert, H.; Wuttig, M.; Calarco, R. *NPG Asia Materials* **2017**, *9*, e396.
- [203] Simpson, R. E.; Fons, P.; Kolobov, A. V.; Fukaya, T.; Krbal, M.; Yagi, T.; Tominaga, J. *Nature Nanotechnology* **2011**, *6*, 501.
- [204] Tominaga, J.; Kolobov, A. V.; Fons, P.; Nakano, T.; Murakami, S. *Advanced Materials Interfaces* **2014**, *1*, 1300027.
- [205] Loke, D.; Lee, T. H.; Wang, W. J.; Shi, L. P.; Zhao, R.; Yeo, Y. C.; Chong, T. C.; Elliott, S. R. *Science* **2012**, *336*, 1566.
- [206] Zhu, M.; Xia, M.; Rao, F.; Li, X.; Wu, L.; Ji, X.; Lv, S.; Song, Z.; Feng, S.; Sun, H.; Zhang, S. *Nature Communications* **2014**, *5*, 4086.
- [207] Xia, M.; Zhu, M.; Wang, Y.; Song, Z.; Rao, F.; Wu, L.; Cheng, Y.; Song, S. *ACS applied materials & interfaces* **2015**, *7*, 7627.
- [208] De Bastiani, R.; Piro, A. M.; Crupi, I.; Grimaldi, M. G.; Rimini, E. *Nuclear Instruments and Methods in Physics Research Section B: Beam Interactions with Materials and Atoms* **2008**, *266*, 2511.
- [209] De Bastiani, R.; Piro, A. M.; Grimaldi, M. G.; Rimini, E.; Baratta, G. A.; Strazzulla, G. *Applied Physics Letters* **2008**, *92*, 241925.
- [210] Rimini, E.; de Bastiani, R.; Carria, E.; Grimaldi, M. G.; Nicotra, G.; Bongiorno, C.; Spinella, C. *Journal of Applied Physics* **2009**, *105*, 123502.
- [211] De Bastiani, R.; Carria, E.; Gibilisco, S.; Grimaldi, M. G.; Pennisi, A. R.; Gotti, A.; Pirovano, A.; Bez, R.; Rimini, E. *Physical Review B* **2009**, *80*, 245205.
- [212] Privitera, S.; Rimini, E.; Zonca, R. *Applied Physics Letters* **2004**, *85*, 3044.
- [213] Liu, B.; Song, Z.; Zhang, T.; Feng, S.; Chen, B. *Applied Surface Science* **2005**, *242*, 62.
- [214] Liu, B.; Song, Z.; Zhang, T.; Xia, J.; Feng, S.; Chen, B. *Thin Solid Films* **2005**, *478*, 49.

- [215] Kim, Y.; Baeck, J. H.; Cho, M.-H.; Jeong, E. J.; Ko, D.-H. *Journal of Applied Physics* **2006**, *100*, 083502.
- [216] Privitera, S.; Rimini, E.; Bongiorno, C.; Pirovano, A.; Bez, R. *Nuclear Instruments and Methods in Physics Research Section B: Beam Interactions with Materials and Atoms* **2007**, *257*, 352.
- [217] Carria, E.; Mio, A. M.; Gibilisco, S.; Miritello, M.; Grimaldi, M. G.; Rimini, E. *Electrochemical and Solid-State Letters* **2011**, *14*, H124.
- [218] Dieker, H.; Wuttig, M. *Thin Solid Films* **2005**, *478*, 248.
- [219] Pouchou, J. L., Pichoir, F. I., Heinrich, K. F. J., & Newbury, D. E., *Electron probe quantitation*; Plenum press: 1991.
- [220] Russ, J. C.; Frs, M. A.; Kiessling, R.; Charles, J., *Fundamentals of Energy Dispersive X-Ray Analysis: Butterworths Monographs in Materials*; Elsevier Science: Burlington, 1984.
- [221] Waseda, Y.; Matsubara, E.; Shinoda, K., *X-Ray Diffraction Crystallography: Introduction, Examples and Solved Problems*; Springer-Verlag Berlin Heidelberg: Berlin, Heidelberg, 2011.
- [222] Pecharsky, V. K.; Zavalij, P. Y., *Fundamentals of Powder Diffraction and Structural Characterization of Materials*, 2. ed.; Springer US: Boston, MA, 2009.
- [223] Jellison, G. E. *Optical Materials* **1992**, *1*, 41.
- [224] Chandler-Horowitz, D.; Amirtharaj, P. M. *Journal of Applied Physics* **2005**, *97*, 123526.
- [225] Perkampus, H.-H., *UV-VIS Spectroscopy and Its Applications*; Springer Lab Manuals; Springer Berlin Heidelberg: Berlin, Heidelberg, 1992.
- [226] Smith, B. C., *Fundamentals of Fourier transform infrared spectroscopy*, 2nd ed.; CRC Press: Boca Raton, Fla, 2011.
- [227] Hawkes, P. W.; Spence, J. C. H., *Science of microscopy*, Corrected print; Springer: New York, NY, 2008.
- [228] Fultz, B.; Howe, J., *Transmission electron microscopy and diffractometry of materials*, 4. ed.; Graduate texts in physics; Springer: Berlin, 2013.
- [229] Kaupp, G., *Atomic force microscopy, scanning nearfield optical microscopy and nanoscratching: Application to rough and natural surfaces*; Nanoscience and technology; Springer-Verlag Berlin Heidelberg: Berlin, Heidelberg, 2006.
- [230] Ocelic, N.; Huber, A.; Hillenbrand, R. *Applied Physics Letters* **2006**, *89*, 101124.
- [231] Novotny, L.; Stranick, S. J. *Annual review of physical chemistry* **2006**, *57*, 303.

- [232] Ambrosio, A.; Devlin, R. C.; Capasso, F.; Wilson, W. L. *ACS Photonics* **2017**, *4*, 846.
- [233] Ambrosio, A.; Jauregui, L. A.; Dai, S.; Chaudhary, K.; Tamagnone, M.; Fogler, M. M.; Basov, D. N.; Capasso, F.; Kim, P.; Wilson, W. L. *ACS Nano* **2017**, *11*, 8741.
- [234] Ambrosio, A.; Tamagnone, M.; Chaudhary, K.; Jauregui, L. A.; Kim, P.; Wilson, W. L.; Capasso, F. *Light, Science & Applications* **2018**, *7*, 27.
- [235] Ziegler, J. F., *Ion Implantation Science and Technology: Science and Technology*; Elsevier Science: Oxford, 1984.
- [236] Rensberg, J., Ph.D. thesis, Friedrich Schiller University Jena, 2017.
- [237] *Introduction to focused ion beams: Instrumentation, theory, techniques and practice*; Giannuzzi, L. A., Ed.; Springer: New York, NY, 2005.
- [238] Yu, W., *Electromagnetic simulation techniques based on the FDTD method*; Wiley series in microwave and optical engineering; Wiley: Hoboken, NJ, 2009.
- [239] Ruffert, K., bachelor thesis, Friedrich Schiller University Jena, 2019.
- [240] Tanaka, K. *physica status solidi (b)* **2020**, 1900756.
- [241] Mio, A. M.; Privitera, S. M. S.; Bragaglia, V.; Arciprete, F.; Bongiorno, C.; Calarco, R.; Rimini, E. *Nanotechnology* **2017**, *28*, 065706.
- [242] Pries, J.; Wei, S.; Wuttig, M.; Lucas, P. *Advanced Materials* **2019**, *31*, e1900784.
- [243] Orava, J.; Greer, A. L.; Gholipour, B.; Hewak, D. W.; Smith, C. E. *Nature Materials* **2012**, *11*, 279.
- [244] Do, K.; Lee, D.; Sohn, H.; Cho, M.-H.; Ko, D.-H. *Journal of The Electrochemical Society* **2010**, *157*, H264.
- [245] Senkader, S.; Wright, C. D. *Journal of Applied Physics* **2004**, *95*, 504.
- [246] He, S.; Zhu, L.; Zhou, J.; Sun, Z. *Inorganic chemistry* **2017**, *56*, 11990.
- [247] Hammond, C., *The basics of crystallography and diffraction*, 2. ed.; Texts on crystallography, Vol. 5; Oxford Univ. Press: Oxford, 2001.
- [248] Popova, S.; Tolstykh, T.; Vorobev, V. *Opt. Spectrosc* **1972**, *33*, 444.
- [249] Malitson, I. H. *Journal of the optical society of america* **1965**, *55*, 1205.
- [250] Njoroge, W. K.; Wöltgens, H.-W.; Wuttig, M. *Journal of Vacuum Science & Technology A: Vacuum, Surfaces, and Films* **2002**, *20*, 230.
- [251] Privitera, S.; Mio, A. M.; Zhang, W.; Mazzarello, R.; Persch, C.; Wuttig, M.; Rimini, E. *Nanoscience and Nanotechnology Letters* **2017**, *9*, 1095.
- [252] Kempf, J.; Nonnenmacher, M.; Wagner, H. H. *Applied Physics A* **1993**, *56*, 385.

- [253] Kolobov, A. V.; Tominaga, J.; Fons, P.; Uruga, T. *Applied Physics Letters* **2003**, *82*, 382.
- [254] Hosseini, P.; Wright, C. D.; Bhaskaran, H. *Nature* **2014**, *511*, 206.
- [255] Du, K.-K.; Li, Q.; Lyu, Y.-B.; Ding, J.-C.; Lu, Y.; Cheng, Z.-Y.; Qiu, M. *Light, science & applications* **2017**, *6*, e16194.
- [256] Sarangan, A.; Duran, J.; Vasilyev, V.; Limberopoulos, N.; Vitebskiy, I.; Anisimov, I. *IEEE Photonics Journal* **2018**, *10*, 1.
- [257] Babar, S.; Weaver, J. H. *Applied Optics* **2015**, *54*, 477.
- [258] De Los Santos, V. L.; Lee, D.; Seo, J.; Leon, F. L.; Bustamante, D. A.; Suzuki, S.; Majima, Y.; Mitrelias, T.; Ionescu, A.; Barnes, C. H. *Surface Science* **2009**, *603*, 2978.
- [259] Goncharenko, A. V.; Lozovski, V. Z.; Venger, E. F. *Optics Communications* **2000**, *174*, 19.
- [260] Greenzweig, Y.; Drezner, Y.; Tan, S.; Livengood, R. H.; Raveh, A. *Microelectronic Engineering* **2016**, *155*, 19.
- [261] Ciocchini, N.; Palumbo, E.; Borghi, M.; Zuliani, P.; Annunziata, R.; Ielmini, D. *IEEE Transactions on Electron Devices* **2014**, *61*, 2136.
- [262] Zuliani, P.; Varesi, E.; Palumbo, E.; Borghi, M.; Tortorelli, I.; Erbetta, D.; Libera, G. D.; Pessina, N.; Gandolfo, A.; Prelini, C.; Ravazzi, L.; Annunziata, R. *IEEE Transactions on Electron Devices* **2013**, *60*, 4020.
- [263] Slater, J. C. *The Journal of Chemical Physics* **1964**, *41*, 3199.
- [264] Choi, K.-J.; Yoon, S.-M.; Lee, N.-Y.; Lee, S.-Y.; Park, Y.-S.; Yu, B.-G.; Ryu, S.-O. *Thin Solid Films* **2008**, *516*, 8810.
- [265] Jellison, G. E.; Modine, F. A. *Applied Physics Letters* **1996**, *69*, 371.
- [266] Tauc, J.; Grigorovici, R.; Vancu, A. *Phys. Status Solidi* **1966**.

A. Appendices

A.1. Supplemental information on sample preparation

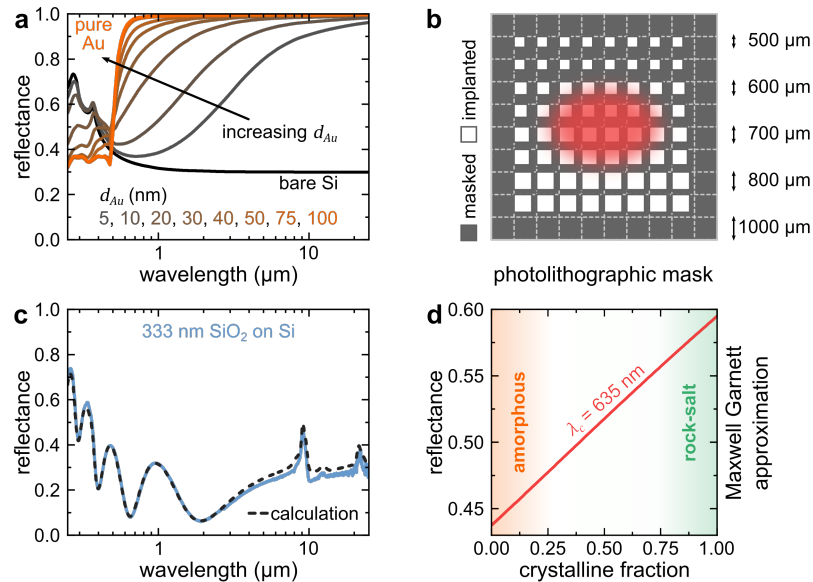


Figure A.1: (a) Calculated reflectance spectra of a thin Au film on a Si substrate. Upon increasing Au thickness (d_{Au}) the reflectance approaches the spectrum of a pure Au substrate. (b) Schematic depiction of the fabricated mask for photolithography. White openings represent the implanted regions. The symbolic laser spot (red) shows the approximate examined area for the temperature-resolved reflection measurements. (c) Measured reflectance spectrum of the thermally oxidized Si substrates (blue solid line). The effective thickness of the SiO₂ layer was determined (333 nm) by comparing the experiment with calculated spectra (best fit shown as dashed line). Refractive index values were taken from references [257] for Au, [223, 224] for Si, and [248, 249] for SiO₂. (d) Calculated reflectance of GST at $\lambda_c = 635$ nm as a function of crystalline fraction using the Maxwell Garnett approximation for crystalline (rock-salt) inclusions within the amorphous matrix.

A.2. Supplemental information on focused ion beam irradiation

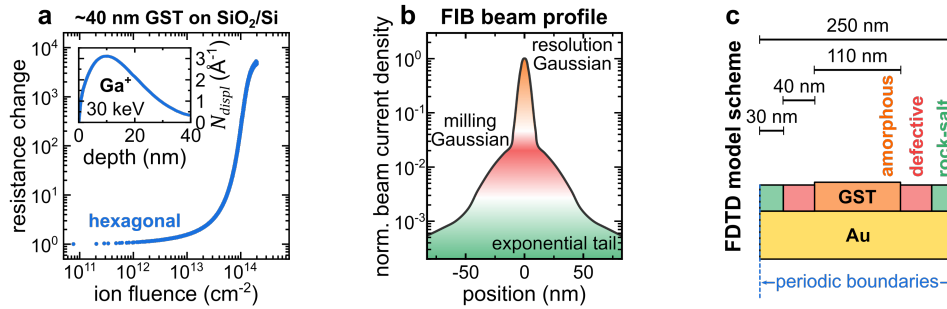


Figure A.2.: (a) Resistance change of a GST film on SiO₂/Si ($d \approx 40$ nm) at a constant flux of $\sim 2 \times 10^{11} \text{ cm}^{-2} \text{ s}^{-1}$, which was irradiated with an Ga⁺-ion energy of 30 keV at an incidence angle of 7°. The overall trend is comparable to the observations of chapter 5. The inset shows the corresponding number of total displacements per incident ion N_{displ} simulated with SRIM. (b) Typical, qualitative focused ion beam profile extracted from irradiation experiments by Greenzweig et al. (adapted from reference [260]). (c) Schematic drawing of the optimized finite-difference time-domain model in cross-section view comprising amorphous (orange), defective (red) and rock-salt (green) GST stripes on top of the Au substrate.

A.3. Dispersion model equations

A.3.1. Tauc-Lorentz dispersion formula

According to Jellison and Modine [265], the optical permittivity ε of amorphous semiconductors and insulators can be parameterized by multiplying the imaginary part ε_2 of the Lorentz oscillator model with the Tauc joint density of states:

$$\varepsilon_{2,TL} = \varepsilon_{2,T} \cdot \varepsilon_{2,L} . \quad (\text{A.1})$$

Interband transitions above the band edge can be described in the parabolic bands approximation by Tauc's dielectric function [266]:

$$\varepsilon_{2,T}(E > E_g) = A_T \cdot \left(\frac{E - E_g}{E} \right)^2 \quad (\text{A.2})$$

with the Tauc coefficient A_T , the photon energy E , and the optical band gap energy E_g . The imaginary part of the Lorentzian oscillator model is given by:

$$\varepsilon_{2,L}(E) = \frac{A_L \cdot E_0 \cdot C \cdot E}{(E^2 - E_0^2)^2 + C^2 \cdot E^2} \quad (\text{A.3})$$

with amplitude A_L and broadening C of the Lorentzian peak $\varepsilon_{2,L}(E_0)$ centered at E_0 . The product of equation A.2 and A.3 yields:

$$\varepsilon_{2,TL}(E) = \begin{cases} \frac{1}{E} \frac{A \cdot E_0 \cdot C \cdot (E - E_g)^2}{(E^2 - E_0^2)^2 + C^2 \cdot E^2} & \text{for } E > E_g \\ 0 & \text{for } E \leq E_g \end{cases} \quad (\text{A.4})$$

with $A = A_T \cdot A_L$. The real part of the dielectric function can be calculated using the Kramers-Kronig relations:

$$\varepsilon_1(E) = \varepsilon_1(\infty) + \frac{2}{\pi} \cdot P \cdot \int_{E_g}^{\infty} \frac{\xi \cdot \varepsilon_2(\xi)}{\xi^2 - E^2} d\xi \quad (\text{A.5})$$

where P denotes the Cauchy principal value. Solving this equation yields a complex expression for $\varepsilon_{1,TL}(E)$, which can be found in reference [265].

A.3.2. Drude model

Taking into account the contribution of free carriers for the optical properties of metals or doped semiconductors is achieved by the Drude dispersion model. Here, the permittivity can be expressed as:

$$\tilde{\varepsilon}_D(\omega) = \varepsilon_\infty - \frac{\omega_p^2}{\omega^2 - i\omega\Gamma} \quad (\text{A.6})$$

with the high frequency permittivity ε_∞ , plasma frequency ω_p , and Γ is the collision frequency.

B. List of publications

Publications directly related to this thesis

- (I) Hafermann, M.; Schöppe, P.; Rensberg, J.; and Ronning, C.
Metasurfaces Enabled by Locally Tailoring Disorder in Phase-Change Materials, *ACS Photonics* **2018**, 5(12), 5103–5109

- (II) Hafermann, M.; Zapf, M.; Ritzer, M.; Printschler, A.; Luo, Y.; Ambrosio, A.; Wilson, W. L.; and Ronning, C.
Grayscale Nanopatterning of Phase-Change Materials for Subwavelength-Scaled, Inherently Planar, Nonvolatile, and Reconfigurable Optical Devices, *ACS Applied Nano Materials* **2020**, 3(5), 4486–4493

Further publications

- (I) Hümpfner, T.; Hafermann, M.; Udhardt, C.; Otto, F.; Forker, R.; and Fritz, T.
Insight into the unit cell: Structure of picene thin films on Ag(100) revealed with complementary methods, *The Journal of Chemical Physics* **2016**, 145(17), 174706

- (II) Salman, J.; Hafermann, M.; Rensberg, J.; Wan, C.; Gundlach, B.; Ronning, C.; and Kats, M. A.
Flat Optical and Plasmonic Devices Using Area-Selective Ion-Beam Doping of Silicon, *Advanced Optical Materials* **2018**, 6(5), 1701027

- (III) Wambold, R.; Salman, J.; Hafermann, M.; Rensberg, J.; Wan, C.; Gundlach, B.; Ronning, C.; and Kats, M. A.
Monolithic Doped-Semiconductor Platform for Optical Devices in the Infrared, *2018 IEEE Research and Applications of Photonics In Defense Conference (RAPID)*, **2018**, 1-3

-
- (IV) Schöppe, P.; Schönherr, S.; Chugh, M.; Mirhosseini, H.; Jackson, P.; Wuerz, R.; Ritzer, M.; Johannes, A.; Martínez-Criado, G.; Wisniewski, W.; Schwarz, T.; Plass, C. T.; Hafermann, M.; Kühne, T. D.; Schnohr, C. S.; and Ronning, C.
Revealing the origin of the beneficial effect of cesium in highly efficient Cu(In,Ga)Se₂ solar cells, *Nano Energy* **2020**, *71*, 104622
- (V) Mei, H.; Koch, A.; Salman, J.; Wan, C.; Wambold, R.; Hafermann, M.; Rensberg, J.; Ronning, C.; and Kats, M. A.
Toward Frequency-Selective Surfaces via Doping of Zinc Oxide with a Focused Ion Beam, *CLEO: Science and Innovations*, **2020**, STu3P.2
- (VI) Zapf, M.; Ritzer, M.; Liborius, L.; Johannes, A.; Hafermann, M.; Schönherr, S.; Segura-Ruiz, J.; Martínez-Criado, G.; Prost, W.; and Ronning, C.
Hot electrons in a nanowire hard X-ray detector, *Nature Communications* **2020**, *11*(1), 4727
- (VII) Plass, C. T.; Ritzer, M.; Schöppe, P.; Schönherr, S.; Zapf, M.; Hafermann, M.; Johannes, A.; Martínez-Criado, G.; Segura-Ruiz, J.; Würz, R.; Jackson, P.; Schnohr, C. S. and Ronning, C.
In-Operando Nanoscale X-ray Analysis Revealing the Local Electrical Properties of Rubidium-Enriched Grain Boundaries in Cu(In,Ga)Se₂ Solar Cells, *ACS Applied Materials & interfaces* **2020**, *12*(51), 57117-57123

C. List of oral and poster presentations

- (I) Poster:** Mid-infrared optical and plasmonic devices enabled by area-selective ion beam doping of silicon
Martin Hafermann, Jad Salman, Jura Rensberg, Chenghao Wan, Raymond Wambold, Bradley S. Gundlach, Mikhail A. Kats, and Carsten Ronning
Workshop Ionenstrahlphysik, Göttingen, 2017
- (II) Talk:** Mid-infrared optical and plasmonic devices enabled by area-selective ion beam doping of silicon
Martin Hafermann, Jad Salman, Jura Rensberg, Chenghao Wan, Raymond Wambold, Bradley S. Gundlach, Mikhail A. Kats, and Carsten Ronning
DPG Spring Meeting, Dresden, 2017
- (III) Talk:** Sub-wavelength phase coexistence patterning of phase-change materials by means of ion irradiation
Martin Hafermann, Jura Rensberg, and Carsten Ronning
MRS Fall Meeting, Boston, 2017
- (IV) Talk:** Sub-wavelength phase coexistence patterning of phase-change materials by means of ion irradiation
Martin Hafermann, Jura Rensberg, and Carsten Ronning
DPG Spring Meeting, Berlin, 2018
- (V) Poster:** Metasurfaces enabled by locally tailoring disorder in phase-change materials
Martin Hafermann, Philipp Schöppe, Jura Rensberg, and Carsten Ronning
MRS Fall Meeting, Boston, 2018
- (VI) Talk:** Phase-change material based active optical metasurfaces enabled by ion irradiation techniques
Martin Hafermann, Maximilian Zapf, Maurizio Ritzer, Axel Printschler, Jura Rensberg, Philipp Schöppe, Luo Yue, Antonio Ambrosio, William L. Wilson, and Carsten Ronning
SPIE Photonics West, San Francisco, 2020

D. Ehrenwörtliche Erklärung

Ich erkläre hiermit ehrenwörtlich, dass ich die vorliegende Arbeit selbständig, ohne unzulässige Hilfe Dritter und ohne Benutzung anderer als der angegebenen Hilfsmittel und Literatur angefertigt habe. Die aus anderen Quellen direkt oder indirekt übernommenen Daten und Konzepte sind unter Angabe der Quelle gekennzeichnet.

Bei der Auswahl und Auswertung folgenden Materials haben mir die nachstehend aufgeführten Personen in der jeweils beschriebenen Weise entgeltlich/unentgeltlich geholfen:

- Die Konzeption und Umsetzung der Messapparaturen für die Temperaturabhängige Reflexionsmessung (TRR) sowie die Erweiterung um optische Messungen der *in-situ* elektrischen Messungen während Ionenbestrahlung wurde gemeinsam mit Dr. Jura Rensberg durchgeführt.
- GST-Dünnschichten wurden teilweise von Robin Schock, Jacon Grandmontagne, Axel Printscher und Konstantin Ruffert gewachsen.
- Mit Gold beschichtete Siliziumsubstrate wurden von Prof. Dr. Frank Schmidl gewachsen.
- Die EDX Messungen wurden in Zusammenarbeit mit Maurizio Ritzer, Dr. Sven Schönherr und Oliver Rüger durchgeführt.
- Sämtliche XRD Messungen wurden von Chenghao Wan an der University of Wisconsin-Madison durchgeführt.
- TRR Messungen in Kapitel 4 wurden in Zusammenarbeit mit Konstantin Ruffert durchgeführt.
- UV-VIS und FTIR-Messungen in Kapitel 4 wurden gemeinsam mit Axel Printscher durchgeführt.
- *In-situ* optische und elektrische Messungen in Kapitel 5 wurden in Zusammenarbeit mit Dr. Jura Rensberg, Veronica Lopez Marcos und Robin Schock durchgeführt.
- Ionenbestrahlungen wurden zumeist mit Hilfe von Patrick Hoffmann durchgeführt.
- TRR, UV-VIS und FTIR-Messungen in Kapitel 5 wurden teilweise von Robin Schock und Axel Printscher durchgeführt.
- FIB Bestrahlungen wurden mit Hilfe von Dr. Philipp Schöppe durchgeführt.
- Die Lamelle wurde von Dr. Philipp Schöppe präpariert und anschließend wurden mit seiner Hilfe SEM und TEM Bilder aufgenommen. Letzteres am Otto-Schott-

Institut Jena.

- FTIR Messungen wurden auch teilweise mit Hilfe von Daniel Füßel und Matthias Falkner am Institut für angewandte Physik (IAP) durchgeführt.
- AFM, PiFM und SNOM Messungen wurden von Yue Luo, Maximilian Zapf und Maurizio Ritzer an der Harvard University durchgeführt.
- TRR, UV-VIS und FTIR-Messungen in Kapitel 7 wurden von Robin Schock und Jacob Grandmontagne durchgeführt.
- Fotolithografie wurde gemeinsam mit Jacob Grandmontagne durchgeführt.
- Optische Mikroskopbilder wurden von Jacob Grandmontagne aufgenommen.
- Im Übrigen waren jeweils die Koautoren der angeführten Veröffentlichungen (siehe Anhang List of Publications) an der Interpretation der Ergebnisse beteiligt.

Weitere Personen waren an der inhaltlich-materiellen Erstellung der vorliegenden Arbeit nicht beteiligt. Insbesondere habe ich hierfür nicht die entgeltliche Hilfe von Vermittlungs- bzw. Beratungsdiensten (Promotionsberater oder andere Personen) in Anspruch genommen. Niemand hat von mir unmittelbar oder mittelbar geldwerte Leistungen für Arbeiten erhalten, die im Zusammenhang mit dem Inhalt der vorgelegten Dissertation stehen.

Die Arbeit wurde bisher weder im In- noch im Ausland in gleicher oder ähnlicher Form einer anderen Prüfungsbehörde vorgelegt.

Die geltende Promotionsordnung der Physikalisch-Astronomischen Fakultät ist mir bekannt.

Ich versichere ehrenwörtlich, dass ich nach bestem Wissen die reine Wahrheit gesagt und nichts verschwiegen habe.

Kleinromstedt, den 10.03.2021

Martin Hafermann